NANOGENERATORS

A Dissertation
Presented to
The Academic Faculty

by

Jinhui Song

In Partial Fulfillment
of the Requirements for the Degree
Doctor of Philosophy in the
School of Material Science and Engineering

Georgia Institute of Technology
August, 2008

NANOPIEZOTRONICS' BASE: NANOGENERATOR

Approved by:

Dr. Zhong Lin Wang, Advisor
School of Materials Science & Engineering
Georgia Institute of Technology

Dr. Robert L. Snyder
School of Materials Science & Engineering
Georgia Institute of Technology

Dr. Russell D. Dupuis
School of Electrical and Computer Engineering
Georgia Institute of Technology Georgia Institute of Technology

Dr. Christopher J. Summers
School of Materials Science & Engineering
Georgia Institute of Technology

Dr. Kenneth A. Gall
School of Materials Science & Engineering
Georgia Institute of Technology

Date Approved: May 16th, 2008

ACKNOWLEDGEMENTS

First of all, I would like to thank my advisor Prof. Z.L. Wang, who always supports me with anything he can do without any reservation. During those years I study under his advice, I learned from him not only the excellent way of research but also the nice characters of a respectful prestigious professor. Whenever I feel frustrated, he always encourages me, leads me to the right direction with his unique foresight. He and his family take care of me not only in my research and study in school, but also the personal life. Their tender care warms me to leave the lonely feelings away as a foreigner student in US and concentrate on study and research. So much I've got from Dr. Wang, no words could express the appreciation to him. Without his supports and guidance, I could not have gone this far.

I also would like to express my appreciation to the other committee members: Dr. Synder, Dr. Dupuis, Dr. Summers and Dr. Gall. They take their precious time to give me advice on my research and thesis.

My group members help me a lot during the years when I studied here. Dr. Ding and Ms. Yolande brought me into the world of powerful tools TEM, SEM in nanoscience. Dr. X.D. Wang acts as my mentor during my entire PhD study, I learned lot from him and also we have lot cooperative work too. Dr. P.X. Gao, Dr. Buchine Jenny Morber, Jun Zhou, Dr. Lao, Jin Liu, Wenjie Mai, Melanie Kirkham, Ben Weintraub, Yifan Gao, Sheng Xu, et al. supported me a lot and let me feel the good family like atmosphere. Here, I would like to thank them all.

I owned my parents so much, thought they could not come here to attend the commencement. I really appreciate everything I took from them: persistence, patience, wisdom, honest, kindness and intelligence. They care and love me more than themselves. I will always feel guilty to them for what they provided me I would never gave them back. My brother and sister take care of me since the day of my birth. They support me and care me without any reservation. Thank them all from the deepest hart.

Finally, I would like to thank my wife. She always stays with me, takes care of my life and gives me support and encouragement. She takes all the possibility to let me be concentrated on my research. She offers more care to me than herself. Without her, I could not be here.

TABLE OF CONTENTS

Page

ACKNOWLEDGEMENTS iii

LIST OF TABLES ix

LIST OF FIGURES x

SUMMARY xxi

CHAPTER

1 INTRODUCTION 1

2 SYNTHESIS OF WELL ALIGNED ZINC OXIDE NANOMATERIALS 5

2.1 Synthesis Facilities 5

2.1.1 Furnace 6

2.1.2 Temperature Gradients Calibration 7

2.1.3 Pressure System 9

2.2 Vapor-Solid-Solid Process 10

2.2.1 Vapor-Solid Process 11

2.2.2 Vapor-Liquid-Solid Process 13

2.2.3 Vapor-Solid-Solid Process 14

2.3 Growth Aligned ZnO Nanowire Arrays 15

2.3.1 Experiment for Synthesizing Aligned ZnO NW Arrays 15

2.3.2 TEM and SEM Characterization 16

2.3.3 “Phase Diagram” for Aligned ZnO NW Arrays 18

2.3.4 Growth ZnO NW Arrays on Nitride Substrates 26

2.3.4.1 Synthesizing ZnO NWs on Nitride Substrates 27

2.3.4.2 Sample Analysis 29

3 MECHANICAL PROPERTY OF ZNO NW ARRAYS 39
3.1 Measurement Method of the Measuring Methods 39
3.1.1 General Review 39
3.1.2 Method for Measuring Mechanical Property of Aligned ZnO 40
3.2 Application of the Measurement Based on AFM 50
3.2.1 Mechanical Property of RuO_2 and RuO_2/TiO_2 Core/Shell NWs 50
3.2.1.1 Introduction of RuO_2 and RuO_2/TiO_2 Core/Shell NWs 50
3.2.1.2 The Measurement 51
3.2.2 Measurement on Ni-doped Metallic $TaSi_2$ Nanowires 55
4 NANO PIEZOTRONICS' BASIS NANOGENERATOR 59
4.1 First Nanogenerator in the World 60
4.1.1 Nanogenerator Based on ZnO Nanowire Arrays 60
4.1.1.1 Samples 60
4.1.1.2 Conductive AFM Measurement of Nanogenerator 63
4.1.1.3 Equivalent Circuit of Nanogenerator 69
4.1.1.4 Bending Theory for Nanogenerator 70
4.1.1.5 Deflection of the Nanowire under External Force 74
4.1.1.6 The Elastic Deformation Energy of the Nanowire 75
4.1.1.7 Analysis and Discussion 76
4.1.1.8 The Unique Dual Property of ZnO Nanowire 82
4.1.1.9 Possibility of Powering Nanodevices Using Nanogenerator 88
4.1.2 Nanogenerator on Plastic Substrate 88
4.1.2.1 The Synthesis of ZnO Nanowires on Flexible Substrate 89
4.1.2.2 Power Generating from ZnO NWs on Flexible Substrate 93
4.2 Power Generating Process of Single ZnO Belt/Wire 102

4.2.1 Experiment Setup 103

4.2.2 Summary of the Experimental Observation 107

4.3 Introduction of New Field: Nano-Piezotronics 115

4.3.1 Piezoelectric Field-effect Transistor 115

5 DC NANOGENERATOR DRIVEN BY ULTRASONIC WAVE 120

5.1 First Prototype DC Nanogenerator Driven by Ultrasonic Wave 120

5.1.1 Fabrication of DC Nanogenerator 120

5.1.2 The Mechanism of DC Nanogenerator 122

5.1.3 The Performance of DC Nanogenerator 127

5.2 Integrated Nanogenerator in Biofluid 131

5.2.1 The Fabrication and Setup 132

5.2.2 The Performance of the Integrated Nanogenerator 132

5.2.3 The Improvement of the Integrated Nanogenerator 135

5.2.4 The Effect of Ultrasonic Wave Intensity 138

6 INVESTIGATING THE PRINCIPLE OF NANOGENERATOR IN DEPTH 141

6.1 Carrier Density and Schottky Barrier with Nanogenerator 141

6.1.1 The Experiment Design 142

6.1.2 Currier Density on the Output of Nanogenerator 143

6.1.3 Schottky Barrier on the Performance of Nanogenerator 147

6.1.4 UV Illumination on the Performance of Nanogenerator 150

6.2 P-Type Oligomer Functionalized ZnO NW Nanogenerator 152

6.2.1 The Experiment Setup 153

6.2.2 Phenomena of Power Generating from OPV Functionalized ZnO Wire/Belt 155

6.2.2.1 Experiment Setup and Preparation 155

6.2.2.2 Special Phenomena 157

6.2.3 Proposed Principle of Power Generating Process from OPV Functionalized ZnO Wire/Belt 158

7 SUGGESTED FUTURE WORK 163

7.1 Improve the Current or Voltage output of Nanogenerator 163

7.1.1 Design Universal Mask to Fabricate Next Generation Nanogenerator 163

7.1.2 Growth Parameters Control to Improve the Uniformity of ZnO Nanowires 165

7.1.3 Frequency Optimization of Input Ultrasonic Wave 166

8 CONCLUSION 167

REFERENCES 172

LIST OF TABLES

Page

Table 3.1: Measured elastic modulus of aligned ZnO nanowires 48

Table 3.2: The elastic modulus of RuO_2 and RuO_2/TiO_2 core/shell structure measured by AFM 53

Table 3.3: Length and elastic modulus of individual Ni-doped $TaSi_2$ nanowires measured with an AFM 57

LIST OF FIGURES

Page

Figure 2.1: Schematic figure of single zone tube furnace for synthesis of ZnO nanowires. 6

Figure 2.2: Temperature profile measured inside the alumina tube for different source temperatures. 8

Figure 2.3: Schematic of the pressure system. 9

Figure 2.4: (a-e) A proposed growth mechanism for ZnO nanobelts through a VS process. (f, g) The growth front and end of a ZnO nanobelt showing no trace of catalyst. 12

Figure 2.5: Aligned ZnO nanorods on GaN substrate. (a) side view SEM image, the inset is the top view SEM image of the sample; (b) TEM image of ZnO nanorods, the inset is an electron diffraction pattern taken from on ZnO rod. 17

Figure 2.6: "Phase diagram" that correlates oxygen partial pressure (in volume percent in the carry gas) and the growth chamber pressure (plotted in logarithm and P is in unit of mbar) for growing aligned ZnO nanorods. The synthesis Line (1) is the line with constant oxygen partial pressure; line (2) is the line with constant system pressure; line (3) is the line with linearly varying oxygen partial pressure and system pressure. 19

Figure 2.7: SEM images of ZnO nanorods grown under the conditions of 4 green points along line (1) in figure 2.7 under constant oxygen partial pressure (2%) but variable chamber pressure: (a) 50 mbar; (b) 30 mbar; (c) 6 mbar; (d) 1.5 mbar. 21

Figure 2.8: SEM images of ZnO nanorods grown under the conditions of 4 green points along line (2) in figure 2.7 under constant chamber pressure (30 mbar) but variable oxygen partial pressure: (a) 1.3% ; (b) 2%; (c) 2.4%; (d) 3%. 23

Figure 2.9: SEM images of ZnO nanorods grown under the conditions of 4 green points along line (3) in figure 2.7 by linearly adjusting the chamber pressure and oxygen partial pressure. (a) 1.6% oxygen partial pressure, 50 mbar chamber pressure; (b) 2% oxygen partial pressure, 30 mbar chamber pressure; (c) 2.5% oxygen partial pressure, 7 mbar chamber pressure; (d) 3% oxygen partial pressure, 1.5 mbar chamber pressure. 25

Figure 2.10: SEM images of aligned ZnO nanorods grown on a GaN substrate . (a) Low-magnification 30º side-view image; (b) High-magnification 30º side-view image; (c) High-magnification top-view image. 29

Figure 2.11: XRD spectra of aligned ZnO nanorods growing on GaN (a), $Al_{0.5}Ga_{0.5}N$ (b), and AlN (c) substrates. 31

Figure 2.12: SEM images of ZnO nanorods growing on GaN (a) and AlN (b) substrates at the edge of catalyst layer; (c - f) EDS spectra of the corresponding circled region in (a) and (b). 33

Figure 2.13: Low-magnification TEM image of ZnO nanorods grown on GaN (a) and AlN (b) substrates; (c) High-magnification TEM image of a single ZnO nanorod; inset: the corresponding electron diffraction pattern of the ZnO nanorod showing in (c). 35

Figure 2.14: Photoluminescence spectra (300K) of aligned ZnO nanorods grown on GaN (a), $Al_{0.5}Ga_{0.5}N$ (b), and AlN (c) substrates.. 37

Figure 3.1: (a, b) SEM images of ZnO nanowire arrays grown on sapphire surfaces. (c) TEM image of the nanowires with gold catalyst at their tips. Inset is an electron diffraction pattern recorded from a nanowire. (d) Statistical distribution in nanowire diameter measured from TEM images. 41

Figure 3.2: Procedures for measuring the elastic modulus of a nanowire in the AFM contacting mode. 42

Figure 3.3: (a) Topological image and (b) lateral force image of the aligned ZnO nanowire arrays received in AFM contacting mode. The elastic modulus of each and every nanowire in the scanning range can be derived from these images. 44

Figure 3.4: (a, b) Line profiles along the dashed lines in Fig. 3.3(a, b) showing the curves of scanner-retracting-distance verses the nanowire-lateral-displacement and the lateral-force verses the lateral-displacement, respectively. (c, d) Enlarged portions of the areas enclosed by rectangles in (a, b), respectively. 46

Figure 3.5: Tip-nanowire geometry for calculating the length/height of the nanowire. 47

Figure 3.6: a) SEM image of RuO2 NWs synthesized by reactive sputtering at 450 °C for 3 h. The inset shows a magnified SEM image of RuO_2 NWs. b) XRD spectrum of the RuO_2 NWs. The marked spectrum shows the simulated result. c) SEM image of the RuO_2/TiO_2 core/shell structure. The inset shows the corresponding magnified SEM image. d) XRD spectrum of the RuO_2/TiO_2 core/shell structure. The marked spectra represent the simulated results. 50

Figure 3.7: a–d) Schematic illustration of AFM tip scanning across a NW. e,f) The topography and lateral-force images of the RuO_2 NWs, respectively. g,h) The topography and lateral-force images of RuO_2/TiO_2 core/shell structure, respectively. 52

Figure 3.8: (a)–(d) The motion of a cantilever scan over the nanowires in an AFM in contact mode. (e) The topography image and (f) the lateral force image taken simultaneously from the AFM in contact mode. (g) Line profile of bending displacement as a function of scanning distance and (h) line profile of the lateral force as a function of the scanning distance recorded from the dashed line along the figures (e) and (f). *h, d* and *fm* represent the largest bending height, scanning distance for the Si tip across the nanowires, and a constant lateral force when the scanner touches the nanowire. 55

Figure 4.1: Experimental design for converting nano-scale mechanical energy into electric energy by a vertical piezoelectric ZnO nanowire. (**A**) SEM images of aligned ZnO nanowires grown on -Al_2O_3 substrate. (**B**) Transmission electron microscopy (TEM) images of ZnO NWs, showing the typical structure of the NW without a gold particle or with a small gold particle at the tip. Each NW is a single crystal and has uniform shape. The inset is an electron diffraction pattern from a NW. Most of the NWs have no gold tip. An NW with a gold tip is inserted. (**C**) Experimental set up and procedures for generating electricity by deforming a piezoelectric NW using a conductive AFM tip. 61

Figure 4.2: TEM images of ZnO nanowires showing no gold caps or with small gold caps at the growth fronts. Note the hespherical shape of the gold particles at the tips. 62

Figure 4.3: Electro-mechanical coupled discharging process of aligned piezoelectric ZnO NWs observed in contact mode. (**A**) Topography image and (**B**) corresponding output voltage image of the NW arrays. (**C**) A series of line profiles of the voltage output signal when the AFM tip scanned across a vertical NW at a time interval of 1 min. The data shows the registration of the electric signal with the location of the NW and the reproducibility of the event over an extended period of time. In (A-C), the scanning speed of the tip was 12.081 μm/s, and the time spent to acquire and output one scan point was 2 ms. (**D**) Line profiles from the topography (red) and output voltage (blue) images across a NW. The peak of the voltage output corresponds approximately to the maximum deflection of the NW, indicating the discharge occurs when the tip is in contact with the compressed side of the nanowire. When the tip touches the NW, piezoelectric charges start to accumulate, but no discharging. The discharge occurs when the deflection reaches close to the maximum y_m. Note the lateral deflection y includes the shape and contact geometry of the tip, which have to be subtracted to derive the true deflection of the NW. (**E**) Line profile of the voltage output signal when the AFM tip scanned across a vertical NW at 12.394 m/s, and the time spent to acquire and output one scan point was 0.05 ms achieved at the maximum scan frequency of the AFM. The inset is an equivalent circuit of the measurement to be used for simulating the discharging process. (**F**) The resonance vibration of a NW after being released by the AFM tip, showing that the stored elastic energy is transferred mainly into vibration energy after creating the piezoelectric discharge event. 64

Figure 4.4: Three different perspectives of outputting the data shown in Fig. 4.3B to clearly image the sharp piezoelectric voltage peaks. 67

Figure 4.5: Piezoelectic output voltage received at a higher scan frequency at a small scan region, showing the shape of the discharge peaks. The output voltage peak is as high as 20 mV. 68

Figure 4.6: Equivalent circuit of the nanogenerator. 69

Figure 4.7: (A) A segment of a nanowire for calculating the bending induced piezoelectric potential across the two side surfaces. (B) The definition of coordination system under an external displacement force F. 71

Figure 4.8: Coordinates for analysis of bending nanowire. 74

Figure 4.9: Conductive AFM scanning images of metal film. (A) topography image (B) corresponding electrical image. 78

Figure 4.10: Experiment on carbon nanotube (A) SEM image of the side view aligned carbon nanotube. (B) SEM image of the top view of aligned carbon nanotube. (C) Corresponding electrical image from the conductive AFM scanning. 79

Figure 4.11: Experiment on aligned WO_3 nanowires sample (A) SEM image of WO_3 nanowires (B) corresponding electrical signals output from conductive AFM scanning. 80

Figure 4.12: Physical principle of the observed power generation process of a piezoelectric ZnO NW, showing a unique coupling of piezoelectric and semiconducting properties in this metal-semiconductor Schottky barrier governed transport process. (**A**) Schematic definition of a NW and the coordination system. (**B**) Longitudinal strain ε_z distribution in the NW after being deflected by an AFM tip from the side. (**C**) The corresponding longitudinal piezoelectric induced electric field E_z distribution in the NW. (**D**) Potential distribution in the NW as a result of piezoelectric effect. The process in (E) is built up the potential; the process in (F) is to discharge the potential. (**G, H**) Contact of the metal tip with a ZnO nanowire having a small gold particle at the top. The piezoelectric potential is built up in the displacing process (G), and later the charges are released through the compressed side of the NW (H). (**J**) Contact of the metal tip with a ZnO nanowire with a large gold particle at the top. 83

Figure 4.13: Electro-mechanical coupled discharging process of aligned piezoelectric ZnO NWs observed in tapping mode. (**A**) The experimental set up. (**B**) Topography image and (**C**) corresponding output voltage image of the NWs. The tapping force was 5 nN, tapping frequency 68 KHz and tapping speed 6 μm/s. The voltage output contains no information but noise, proving the physical mechanism demonstrated in Fig. 4.12. 87

Figure 4.14: A series of SEM and TEM images of the typical ZnO NW arrays grown on a plastic substrate. a) and b) are respectively a low-magnification top view of the densely aligned NW arrays and a corresponding magnified SEM image. The inset is an optical image of the sample with NWs on polymer surface. c) A side view SEM image displaying orientation aligned ZnO NWs normal to the plastic substrate. d) A typical TEM image of an individual ZnO NW, inset is a corresponding selected area electron diffraction pattern. 90

Figure 4.15: a) and b) are respectively a low-magnification and an enlarged SEM images for the sparsely grown ZnO NW arrays on the plastic substrate. c) Experimental schematic for the conductive AFM measurement on the NWs array. Note the polarity of the defined output voltage on the external load. d) typical voltage output profile for the AFM tip scanning over a single NW on the plastic substrate. e) and f) are 3D plotted AFM topography image and voltage output profile received by scanning the AFM tip over a 40 μm x 40 μm area of aligned ZnO NWs on the plastic substrate. 92

Figure 4.16: The simultaneously recorded line scanning topography image (blue dotted line) and corresponding voltage output profile (red line) from several aligned ZnO NWs. The inset at the upper part is a two-dimensional height profile (top) and the simultaneously recorded voltage output image (bottom) by scanning the tip across an area of 6.5 μm x 3.2 μm. Schematic tip to NW local contacts are displayed at the left-bottom corner for the corresponding locations. 96

Figure 4.17: a) and b) are respectively a top view SEM image of the as-grown densely packed and vertically aligned ZnO microwires array (inset: a side view of aligned microwires array) on the plastic substrate and the corresponding AFM voltage output profile (20 μm x 20 μm). The inset SEM image in b) shows a portion of the microwires pushed-down by the AFM tip. c) and d) are respectively a top view SEM image showing the PMMA coating reinforced ZnO wires aligned on the plastic substrate (inset: an enlarged view of PMMA encapsulated microwires) and the corresponding AFM voltage output profile under AFM measurement (inset: topography image of the 20 μm x 20 μm area). 98

Figure 4.18: a) and b) are respectively a typical SEM image of sparsely grown aligned ZnO nanocones (inset: an enlarged view of a single nanocone) and the corresponding AFM voltage output profile (20 μm x 20 μm) under AFM measurement. c) and d) are respectively a typical top view SEM image of the randomly oriented ZnO NWs on a plastic substrate (inset: an enlarged view showing the randomly tilted NWs on plastic substrate) and the corresponding AFM voltage output profile (20 μm x 20 μm). 101

Figure 4.19: In-situ observation of the process for converting mechanical energy into electric energy by a piezoelectric ZnO wire. (**A**) SEM images of a ZnO wire with one end affixed by silver paste onto a silicon substrate and the other end is free. The wire has a hexagonal cross-section. (**B, C and D**) Three characteristic snapshots and the corresponding output voltage images when the tip scanned across the wire. The schematic illustration of the experimental condition is shown at the left-hand side, with the scanning direction of the tip indicated by an arrowhead. In (**B**), the AFM tip scanned over the top of the wire on the silicon substrate, and the voltage output is just in the noise level. In (**C**), the AFM tip touched the top end of the wire and the output voltage image showed a sharp negative peak. In (**D**), right after the AFM tip passed the top end of the wire and scanned towards its lower part, but without across the wire, no output voltage was detected. 104

Figure 4.20: In-situ observation of the process for converting mechanical energy into electric energy by a piezoelectric ZnO belt. (**A**) SEM images of a ZnO belt with one end affixed by silver paste onto a silicon substrate and the other end is free. The belt has a rectangular cross-section. (**B, C** and **D**) Three characteristic snapshots and the corresponding topography (red curve) and output voltage (blue curve) images when the tip scanned across the middle section of the belt. In (**B**), the AFM tip pushed the belt towards the right-hand side but did not go above and across its width, as judged from the topography image, no output voltage was detected. In (**C**), the AFM tip pushed the belt towards the right-hand side and went above and across its width, as judged from the peak in the topography image, the output voltage image showed a sharp negative peak. In (**D**), for an alternative belt, the AFM tip pushes the belt towards the left but did not go above and across its width, as judged from the topography image, no output voltage was detected beyond noise level although the deflection was large. 106

Figure 4.21: Working mechanism for the power generation process of a piezoelectric ZnO wire/belt as a result of coupled piezoelectric and semiconducting properties in conjunction with the Schottky barrier at the AFM tip-semiconductor interface. (**A**) Schematic definition of a belt. (**B**) Longitudinal strain $_z$ distribution in the belt after being deflected by an AFM tip from the side. (**C**) The corresponding longitudinal piezoelectric induced electric field E_z distribution in the belt with. (**D**) Potential distribution in the belt as a result of piezoelectric effect, with the stretched and compressed side surfaces being positive and negative potentials, respectively. (**E, F**) Metal and semiconductor contacts between the AFM tip and the semiconductor ZnO belt at two reversed local contact potentials (positive and negative), showing reverse and forward biased Schottky rectifying behavior, respectively. The process in (E) is to build up and preserve the charges/potential; the process in (F) is to discharge the potential through a flow of electrons from the circuit. The negative output voltage on the load is a result of current flow from the AFM tip through the ZnO belt to the ground. 109

Figure 4.22: Experiments to verify that the contact between silver paste with ZnO wire/belt is Ohmic. (**A**) I-V characteristic of a ZnO wire with both ends in contact with silver paste. (**B**) I-V characteristic of a ZnO wire with one end in contact with silver paste and the other end with tungsten tip. 111

Figure 4.23: Three occasionally observed phenomena in the AFM manipulation of a ZnO wire/wire, showing some unique characteristics for the power generator that may be missed in most of cases due to the slow response of the AFM tip in scanning speed and data output rates. (**A**) Schematic of the resonance vibration of a wire after being released by the AFM tip, showing that the stored elastic energy is transferred mainly into vibration energy after creating the piezoelectric discharge event. (**B**) A largely bent wire and its corresponding SEM image, but with no output voltage signal. (**C**) A bent wire, its corresponding SEM image and a positive output voltage peak at the very beginning of the AFM deformation. 114

Figure 4.24: (a-e) SEM images showing five different examples of bends introduced into a ZnO NW. Scale bar = 10 μm. (f) Corresponding I-V characteristics of the ZnONW for the five different bending cases. Schematics showing the mechanisms responsible to the conductance change: (g) the carrier trapping effect; and (h) thecreation of a charge depletion zone. (i) Plot showing the relationship between the ZnO NW conductance and the deflection force derived from the experimentaldata, demonstrating a nanoscale force or pressure sensor using a single NW. Inset: schematic of the deflected NW. 117

Figure 5.1: Nanogenerators driven by ultrasonic wave. (**A**) Schematic diagram showing the design and structure of the nanogenertor. Aligned ZnO NWs grown on a solid/polymer substrate are covered by a zig-zag electrode. The substrate and the electrode are directly connected to an external load. (**B**) Aligned ZnO NWs grown on a GaN substrate. The gold catalyst particles used for the growth had been mostly vaporized, thus, the final NWs are purely ZnO with flat top ends. (**C**) The zig-zag trenched electrode fabricated by standard etching technique. (**D**) A cross-section SEM image of the nanogenerator composed of aligned NWs and the zig-zag electrode. The inset shows a typical NW that is forced by the electrode to bend, resulting in output of electricity once touches the left-hand adjacent tooth. 121

Figure 5.2: The mechanism of the nanogenerator driven by ultrasonice wave. (**A**) Schematic illustration of the zig-zag electrode and the four types of representing configurations of the NWs. (**B**) The piezoelectric potential created across the NW I and II under the push/deflection of the electrode as driven by the ultrasonic wave, but without flow of current due to the reversely biased Schottky diode at the electrode-NW interface. The NW III is in resonance under the stimulation of the ultrasonic wave. (**C**) Once the NWs touche the surface of the adjacent teeth, the Schottky diode at the electrode-NW interface is forward biased, piezoelectric discharge occurs, resulting in the observation of current flow in the external circuit. (**D**) The effective circuit of the nanogenerator and the set up for measuring the output current I, output voltage V and the resistance R (see text). (**E, F, G**) Measured output current I, output voltage V and the resistance R using the connections shown in (D), respectively, when the ultrasonic wave was turned on and off periodically. A pixel averaging was applied to reduce the noise. 123

Figure 5.3: Continues DC output of the nanogenerator. (**A**) Reproducible and highly repeatable current output of the nanogenerator when the ultrasonic wave was turned on and off. (**B**) Continuous current output of the nanogenerator for an extended period of time. The data are displayed after correcting the background introduced by electronic drift. 128

Figure 5.4: Output of the nanogenerator using different materials and different design configurations. (**A**) Nanogenerator based on arrays of carbon nanotubes with a zig-zag top electrode, showing no output current regardless the ultrasonic wave was on or off. (**B**) Nanogenerator based on arrays of ZnO NWs but with flat top electrode, showing no output current while stimulated by ultrasonic wave. (**C**) Nanogenerator based on arrays of ZnO NWs with a zig-zag top electrode, showing detectable output current when the ultrasonic wave was turned on.129

Figure 5.5: (a) Schematic of a NG that operates in biofluid and the two types of connections used to characterize the performance of the NG. The pink and blue curves represent signals from forward connected current/voltage (*I*/*V*) meter and reversely connected *I*/*V* meter, respectively. (b, c) The short circuit current and open circuit voltage measured by the two types of connections when the ultrasonic wave was turned on and off. 133

Figure 5.6: **Figure 5.6** Short circuit current measured from an integrated NGs system. (a, b) Current signal measured from two individual NGs, I and II. (c, d) Current signal measured from parallel and antiparallel connected NG I and NG II, respectively; the connection configurations are schematically shown in the insets. (e) Current signal measured from NG III with a better performance. (f) Current signal measured from parallel connected NG I, II, and III; inset shows the connection configuration. 135

Figure 5.7: Open circuit voltage measured from an integrated NGs system. (a-c) Voltage signal measured from one, two, and three serial connected NGs. The connection configurations are schematically shown in the insets. 137

Figure 5.8: **Figure 5.8** Enhanced output power by seeking the strong local intensity of the ultrasonic waves. (a) Schematic of the NG's position and moving directions inside biofluid. (b) Short circuit current signal measured during the movement of NG along the *z* direction (from water surface to the bottom and then back to surface). (c) Short circuit current signal measured during the movement of NG along the *x* and *y* directions while the *z* position was kept 3.3 cm below the water surface. 138

Figure 6.1: (a) Experimental set up for measuring the UV response of an assembled nanogenerator (NG) in liquid. The nanogenertor (NG) is placed up side down to ensure the UV illumination from the substrate side. (b) UV transmittance spectra through AlN/sapphire substrate and water to ensure the penetration of the UV into the core of the nanogenerator (NG). 143

Figure 6.2: Tuning the transport property of ZnO and an assembled nanogenerator (NG) by UV excitation. (a) Response of the current transported through a thin ZnO film with NWs on top when subjecting to UV illumination, showing a long delay in the recovering process. The externally applied voltage $V_0 = 2$ V. The inset is the measurement set up. (b) Current transported through an assembled NG under an externally applied voltage $V_0 = 2$ V when the UV light was tuned on and off. The dark and red curves represent the response curve at full UV intensity I_{UV} and $I_{UV}/4$, respectively. The inset is the measurement set up. 144

Figure 6.3: The output of a nanogenerator (NG) as excited by ultrasonic wave when the UV light was turned on and off. The UV light can reduce the output current 30-50%, indicating increasing (increase) of carrier density is not beneficial for improving the output power. 146

Figure 6.4: I-V characteristic of an assembled nanogenerator (NG) for identifying its performance for producing current. (a) For an NG that actively producinig (producing) current, as shown in the inset, its I-V curve when the ultrasonic wave was off clearly shows a Schottky diode behavior. UV light not only increased the carrier density (or conductivity) but also might reduce the barrier height. (b) For a "defective" NG that did not produce current, the I-V curve clearly shows a clearly Ohmic behavior. The UV light clearly increased the conductivity. 147

Figure 6.5: (a) AFM based measurement set up for correlating the relationship between the metal-ZnO contact and the NG output. (b) Output potential generated by ZnO NW array when scanned by a Pt coated Si tip. (c) No output potential is generated by ZnO NW array when scanned by an Al-In coated Si tip. (d) Experimental set up for characterizing the I-V transport property of metal-ZnO NW contact. (e) I-V curve of a Pt-ZnO NW contact, showing Schottky diode effect. (f) I-V curve of an alloyed Al/In-ZnO NW contact, showing Ohmic behavior. 149

Figure 6.6: Two-electrode based device fabricated using a ZnO nanowire for measuring its transport property when subjecting to UV illumination. An SEM image of the device is inset. The asymmetric contact at the two ends results in a Schottky diode. The UV not only increased the carrier density but also reduced the barrier height at the interface. 150

Figure 6.7: In situ observation of the process of outputting piezoelectric potential by scanning an one-end-free ZnO wire/belt using an AFM tip. The ZnO is clean without oligomer coating. Top inset is a snapshot optical image of the AFM tip that is deflecting the wire/belt. Bottom inset is a schematic experimental setup. The curves are the aligned plot of the output voltage (blue curve) over the external load and the topography profile (pink curve). 153

Figure 6.8: In situ observation of the process of outputting piezoelectric potential of a one-end-free ZnO wire/belt that is coated with a thin layer of OPV2 . (a, b) Aligned plot of the output voltage (blue curve) over the external load and the topography profile (pink curve) measured from two different wires/belts. Top inset is a TEM image showing the thickness of the oligomer coating. Schematic cross-section of the wire/belt is illustrated. 156

Figure 6.9: I-V Characteristics of the contacts between Pt electrode and ZnO nanowires without coating (pink); Pt electrode and OPV2 (black); Pt electrode and OPV2 functionalized ZnO nanowires (blue). Inset is a schematic diagram of the experiment set up. A flat Pt electrode was placed on the top of the aligned ZnO nanowire with or without coating a layer of p-type oligomer. 158

Figure 6.10: Proposed model of the piezoelectric potential generated from a OPV2 coated ZnO wire/belt when deflected by an AFM tip. (a, b) Metal and semiconductor contacts between the AFM tip and the semiconductor ZnO belt coated with OPV2 at positive and negative local contact potential (see text). (c) Schematic diagram showing the barrier height at the OPV2-ZnO p-n junction. 161

Figure 7.1: Schematic design for the high output nanogenerator. (a) E-Beam lithography mask with open stripes. (b) Depositing gold pattern on GaN substrate by using the mask in (a). (c) Silicon substrate with photolithography pattern by using the mask in (a). (d) Growing ZnO nanowires by the substrate in (b). (e) Chemical etching the patterned silicon substrate to for zigzag electrode. (f)Diagram for assembling nanogenerator by the patterned growth ZnO nanwires sample with the matching silicon zigzag electrode coated with Pt. 164

SUMMARY

Nanotechnology and nanoscience are experiencing rapid development in the last decade. Intensive research has been carried out on nanostructures synthesis and nanodevices fabrication. Due to its small size, a nanodevice usually requires an extremely small power to operate. However, to make the novel nanodevice work, an external power source is normally needed, which can either be a battery or a power source, thus, the size of the battery is usually much larger than that of the device and its life time is limited. It is highly desired to have a nanoscale size power source that harvests its energy from the environment so that it works independently and wirelessly to provide power to the nanodevices. This dissertation provides a solid solution to this dilemma based on nanotechnology. Starting from the synthesis of well aligned ZnO nanowire arrays on different substrates, an innovative method is presented first to measure the mechanical property of the as-synthesized ZnO nanowire arrays by using AFM without destroying and manipulating the sample. This technique is then extended to converte mechanical energy into electricity by scanning the nanowire arrays using a AFM tip in contact mode. Due to the unique semiconducting and piezoelectric dual properties of ZnO, mechanical energy is converted into electricity and is effectively output. This is the invention of the piezoelectric nanogenerator. Then, by replacing AFM tips using a zigzag top electrode, the first prototype direct-cirrent nanogenerator driven by ultrasonic wave has been fabricated. Further investigations have also been carried out about the effect of ZnO carrier density on the output power, and the power generating property of oligomer functionalized ZnO nanowires. This desertation established the fundamental mechanism

for the nanogenerator, and it provides a new path towards self-powered nanosystems, which has key applications in in-vivo biosensing, MEMS, environmental mornitoring, defence technology and even personal electronics.

CHAPTER 1

INTRODUCTION

Nanoscience and nanotechnology are technologies characterized by length for second time in the long history of industrial engineering. The first technology characterized by length is microelectronics. The archetypical microelectronics technology is photolithography to make tiny transistors to form integrated circuits (IC). Nowdays, the smallest transistor can achieve 50 nm in length, which is almost the limitation of optical wavelength. By further minimizing the scale and lowering the cost of fabrication, microelectronics has "given birth" to nanoscience and nanotechnology.

Nanoscience and nanotechnology can be defined as research into the principle or utilization of materials and fabrication of devices or systems through control of materials on the nanometer scale, i.e. at the level of atoms or assembles of atoms, molecules, supermolecules structures and at least one characteristic dimension is within nanoscale (1-100 nm).

Starting from the last decade, nanoscience and nanotechnology have highly affected multidisciplinary fields such as applied physics, material science, chemistry, device physics, interface science, robotics, chemical engineering, mechanical engineering, electrical engineering and biological engineering et al..

As materials shrink dimensions to nanoscale, numerous novel prosperities and phenomena appear which are dramatically different from those in the bulk state. When materials dimensions are reduced to nanometer scale, quantum confinement phenomena dominate the properities. For example, the melting temperature of a gold nanoparticle decreases dramatically when its diameter is below 20 nm; the color of the emitting light from semiconductor nanoparticles varies with their sizes. The surface to volume ratio increases intensively as the material size reaches nanoscale. Surface energy dominates

most of the mechanical, chemical and physical properties, which could make the nanomaterial more durable, more ductile and exhibit novel properties which the bulk material does not have.

For bulk materials, classic physics theory describes and predicts the morphology, property and character. For a single atom, quantum theory could describe its character. When the bulk material shrinks to nanoscale, quantum refinement dominates a material's property. But nanometer scale materials may contain several tens of thousands of atoms. It is almost impossible and nonsense to calculate every atom of those thousands of atoms to find the overall property. Thus, new theories which could describe materials at the nanoscale need to be investigated. Nanoscience mainly focuses on the principle and basic property research of nanomaterials, while nanotechnology attempts to synthesize different nanostructures and utilize those nanomaterals to fabricate nanodevices.

During the past decades, nano related research has achieved intensive progress, which brings us plenty of high-tech benefits. Diverse nanostructures have been fabricated. Numerous properties have been measured on those nanomaterials. The properties of nanomaterials show differ from their bulk counterparts. Some novel devices based on those nanomaterials have been fabricated and tested. Nanoscience and nanotechnology though, are still in their infancy. Among the nanomaterials, the carbon nanotube is the famous one, which has ultra high strength and has been used in many high tech products for human daily life. Also some nanotechnology has been commercialized, using the advantages of colloidal nanoparticles in bulk form. Suntan lotion, protective coating, stain resistant cloth, drug delivery and ultra light glass fiber with carbon nanotubes to greatly improve strength are typical samples.

Researchers have synthesized diverse nanostructures on different materials, such as nanowires, nanobelts, nanorings, nanosprings, nanobows, nanospheres et al.. Based on the nanostructures plenty of nanodevices have been fabricated. Research in synthesizing nanostructures based on different materials and fabricating nanodevices based on these

nanostructures is rapidly expanding and becoming the forefront of nanoscience and nanotechnology. Fabricating gas sensors based on a single nanowire have more sensitivity and lighter weight, smaller volume and lowerer power consumption. Some nanosensors can even detect single cancer cell. Even the nanoscale logical circuit has been fabricated recently.

Although fabricating nanodevices attracts intensive research interest and many novel nanodevices have been successfully made which have smaller size, more sensitivity and lower power consuming properties, those novel devices still need power supply to function. Usually a battery is the candidate to provide power supply to those nanodevices. However, there are two fatal drawbacks. One is that the traditional battery size is ultra big compared with the size of the nanodevice. Although the nanodevice is small, and can be used in a tiny area, the battery which enables the nanodevice to work properly is extraordinary big. The advance of the small size of the nanodevice is counteracted. In other word, only together with nanoscale power source the nanodevice could form nanosystem as an independent working unit. The other drawback of the traditional battery is that the battery needs to be replaced or recharged from time to time. Ideally, the nanosystem should work wirelessly and independently. It is highly desired for implanted biomedical devices to be self-powered without a battery. Therefore, it is essential to explore innovative nanotechnologies for converting mechanical energy (such as body movement, muscle stretching, vehicle idling), vibrational energy (such as acoustic/ultrasonic wave), and hydraulic energy (such as wind, body fluid and blood flow) into electrical energy that would power nanodevices to build nanosystems without using a battery.

Unfortunately, little work has been done on the nano-power source. Although some novel nanodevices have been fabricated for biomedical/bio-implantable use, without a similar size range power source, none of the nanodevices have real application. It is essential to find the proper power source in the nanoscale to provide power to the

nanodevices so that the nanosystem can have real applications. Nanoscale power source is becoming the bottle neck for developing and applying nanoscience and nanotechnology.

This dissertation will focus on the solution of nanoscale power source: a nanogenerator based on ZnO nanostructures, which is the basis of the new field "Nano-Piezotronics". It is first time to investigate and solve the power source dilemma in nanoscience and nanotechnology. The research which will be described here would pave the way to the practical application of nanotechnology.

The next chapter (chapter 2) of this dissertation will discuss the synthesis of ZnO nanowire arrays. In order to improve the stability and understand the as-synthesized ZnO nanowire arrays, chapter 3 will focus on the elastic modulus measurement. Furthermore, chapter 4 will introduce the firstever nanogenerator in the world. By using a conductive AFM working in contact mode, mechanical energy has been converted to electric energy by a ZnO nanowire due to its unique semiconducting and piezoelectric dual properities. Based on this mechanism, a direct current nanogenerator driven by ultrasonic waves has been fabricated. Chapter 5 will illustrate the prototype nanogenerator driven by ultrasonic waves in detail. To demonstrate the ability of the nanogenerator working in fluid, chapter 6 will discuss the effect of carrier density and Schottky barrier to the output of the nanogenerator and the power generating character of p-type polymer coated ZnO nanowires. Chapter 7 will give the future work, and chapter 8 is the conclusion.

CHAPTER 2

SYNTHESIS OF WELL ALIGNENED ZINC OXIDE NANOMATERIALS

Quasi-one-dimensional (1D) ZnO nanostructures such as nanobelt[1], nanowire[2], nanorods[3] and nanosprings/nanorings[4] have attracted a lot of research interest due to their shape induced unique electrical and optical properties for applications in sensors[5], optoelectronics[6], field emissions[7] and logical circuit devices[8]. Growth of ZnO nano structures has been one of the most active fields in nanotechnology.[9] Fabrication of vertically aligned ZnO 1D structures is considered to be an effective approach for nano-devices assembly and applications on light emitting[10] and field emission[11]. Synthesis of 1 dimensional nanostructures is fundamental to fabricate nanodevices. In this chapter, the synthesis of well aligned ZnO nanowires on GaN/Al_2O_3 substrates will be well discussed. Aligned growth of ZnO nanowires can be achieved by various methods, such as vapor-solid-solid process[12], metal-organic chemical vapor deposition (MOCVD)[13] or sol-gel process[14]. As the simplest and most efficient method, VSS process has been employed by many researchers for growing aligned ZnO nanorods on various substrates, such as silicon[15], sapphire[10, 16], GaN[17, 18] and AlGaN/AlN[19]. Consequently, this method has been very successful and versatile in fabricating nanobelts and nanowires with various characteristics. The thermal evaporation technique (VSS) is a very simple process in which solid or powder source material is vaporized at elevated temperatures and then the resultant vapor phase(s) is condensed under certain conditions (temperature, pressure, atmosphere, substrate, etc.) to form the desired nanostructures.

2.1 Synthesis Facilities

The facilities used to synthesize well aligned ZnO nanowires include a furnace and pressure system. The furnace system provides the fundamental temperature control of the reaction chamber for nanostructure deposition; while the pressure system was responsible for the evaporation and deposition pressure condition inside the reaction

chamber. Both systems and the basic control principles will be described in detail in the followings.

2.1.1 Furnace

The furnace system for the thermal evaporation method to synthesis ZnO nanowires is like the schematic figure 2.1 below.

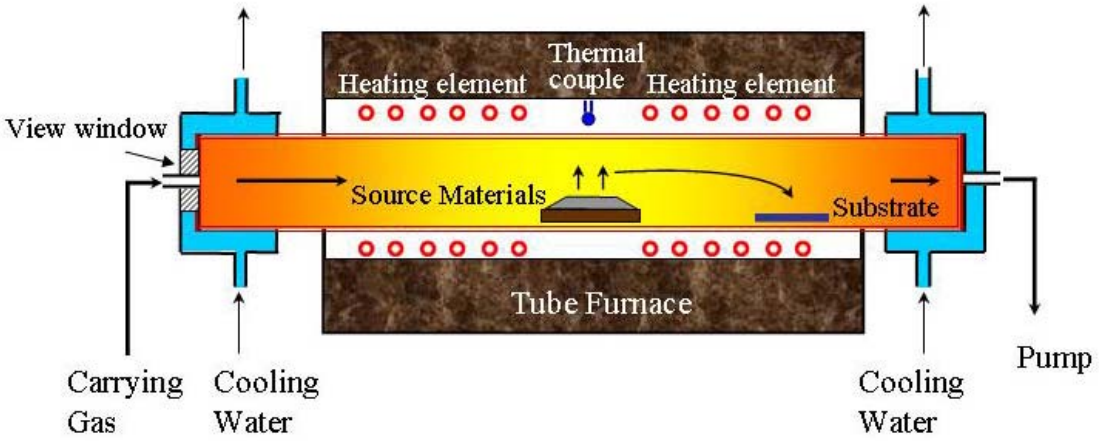

Figure 2.1 Schematic figure of single zone tube furnace for synthesis of ZnO nanowires

The core part of the system is the single zone tube furnace whose model number is Thermolyne 793000. Exposed heating element coils embedded into ceramic fiber insulation provided the capability of rapidly ramping the temperature up to 1200 ˚C in 20 minutes. A digital C1 programmable controller with one stored program of eight segments controls the heating of the furnace. Each segment of the program consists of three parts: a ramp rate (ranging from 1 ˚C/min to 60 ˚C/min), a temperature set point (ranging from 100˚C to 1200˚C), and a dwell time (ranging from 0.1 min to 999.9 min). An alumina tube with a length of 30”, 1.75” outer diameter and 1.50” inner diameter is

placed inside the tube furnace. Because the furnace chamber is only 24" in length, the alumina tube protruded six inches on either side of the furnace. Both ends of the tube are covered by stainless steel end caps and sealed with O-rings. Cooling water with constant temperture is circulated inside the cover caps to form a reasonable temperature gradient in the tube. One end cap is fitted with a gas inlet connection for introducing the inert carrier gas into the system as carrying gas and a quartz window is also embedded on this end cap to monitor the evaporation process inside the tube or as a transparent window for introducing laser beam to heat the source target. Another end cap is connected to the pressure system to exhaust the waste gases into a hood.

In the system, the alumina tube acts as the reaction chamber for evaporation and deposition. Generally, source powders loaded in an alumina boat are located in the middle of the furnace, the highest temperature region. The desired nanostructures are deposited on substrates placed a certain distance away from the source in the down-stream direction of the carrier gas.

2.1.2 Temperature gradients calibration

The temperature control is one of the most important parameters for synthesis. The temperature for the furnace system related with this dissertation is measured by a thermal couple placed at the center of the furnace chamber, but outside and on the top of the alumina tube. As a single zone furnace, the temperature readout is the only feedback available to control the temperature inside the furnace. Therefore, it is essential to know the temperature gradient along the horizontal direction for the local deposition temperature is coupled for the distance from the substrate to tube center where the highest temperature is. As such, the temperature gradients for several different furnace temperatures are measured. An S-type thermocouple element (Platinum 10% Rhodium)

sheathed in an alumina sleeve, is inserted into the furnace under a 300mbar vacuum. A series of data points are taken at various positions within the alumina tube which is centered in the furnace, so that the temperature gradient across the entire furnace could be extrapolated. Although all of the data for the measured temperature gradients are taken using a 300 mbar chamber pressure, previous unpublished studies demonstrated no change in the temperature gradient with varied chamber pressure, which is to be expected. Figure 2.2 shows the data for five distinct source temperatures and their corresponding temperature gradients.

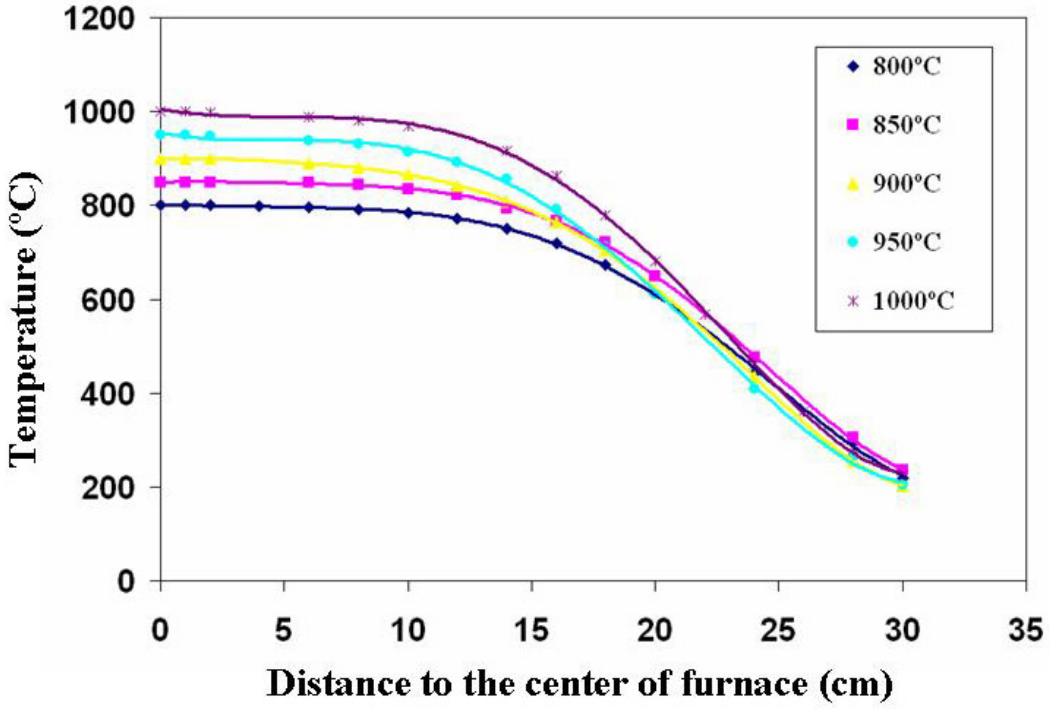

Figure 2.2: Temperature profile measured inside the alumina tube (from the center to the outside of the furnace) for different source temperatures.

A best-fit curve is calculated for each. These curves were then used to extrapolate the local substrate temperature with the corresponding source temperatures for synthesis.

2.1.3 Pressure system

The pressure system is made of three distinct parts. Following the direction of the gas flow, they are carrier gas introduction, pressure monitor and control and pump, as shown in Figure 2.3.

The carrier gas module is comprised by gas cylinders and mass flow controllers. The gases used in the system include N_2, Ar, and O_2, and each is individually connected to an Aalborg mass flow controller to regulate the gas flow rate through the chamber. The

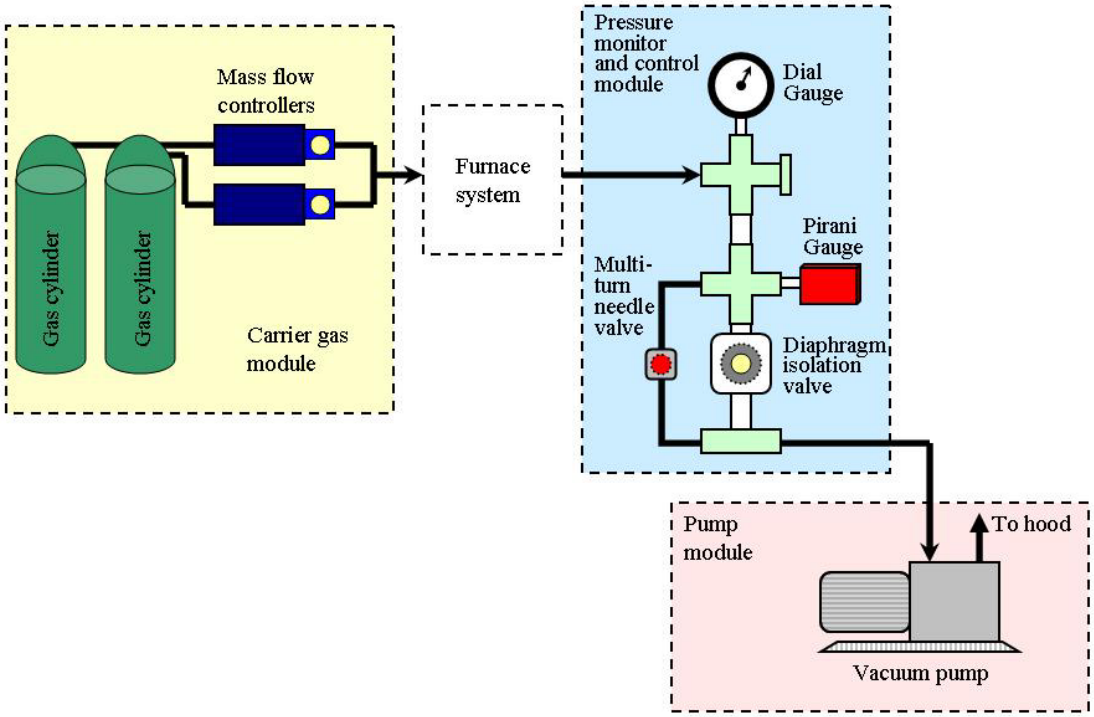

Figure 2.3: Schematic of the pressure system.

maximum flow rates of N_2, Ar and O_2 were 200, 100 and 10 standard cubic centimeter per minute (sccm) respectively, and are controlled to within 2% of their maximum flow rate. All of the outlets of the mass flow controllers are joined via 1/4" plastic tubing, and are connected to the gas inlet port of the end cap.

The pressure monitor and control module is connected to the outlet of the furnace system. For the sensitivity reason, the pressure is monitored by tow gauges: high vacuum gauge; low vacuum gauge. The high vacuum conditions are measured by a BOC Edwards analog Pirani vacuum gauge series 500 which has a working range from 100 to 10^{-3} mbar. The low vacuum level is detected by a BOC Edwards analog dial vacuum gauge series CG16K over the pressure range from 10 to 1000 mbar. In addition to monitoring the chamber pressure, two valves are incorporated in order to control the chamber pressure with coarse and fine adjustments. The coarse valve is a BOC Edwards diaphragm isolation valve. The primary purpose of this valve is to fully open the system to the mechanical pump and purge the chamber. A fine adjustable Cole-Palmer multi-turn needle valve is then used during synthesis to make small pressure adjustments and to achieve and maintain a stable reaction chamber pressure. The additional advantage of using double valves is that the needle valve makes vacuum gradually without sucking the power source to the pump system.

A BOC Edwards RV8 Hydrocarbon rotary vacuum pump is used to maintain the vacuum of the system. The mechanical pump has a pumping rate of 8.0 m^3/h and an ultimate vacuum of $2x10^{-3}$ mbar. Despite the fact that excess oxygen content can have an adverse effect on deposition, this system is found to be sufficient. The mechanical pump is connected to the vacuum controlling module by a 3-ft, 2-inch-wide flexible stainless steel tube and the outlet is directly connected to the hood exhausting system.

2.2 Vapor –Solid-Solid Process

Crystallization from vapor, liquid or solid phases is the essence of forming 1D nanostructures. The most adaptable growth of 1D nanostructure is still believed to be from the vapor phase because the transportation and concentration control of the building blocks are relatively easy. Three primary growth mechanisms of the nucleation and

growth from vapor source are widely accepted amongst the one-dimensional nanostructure synthesis community: the vapor-solid (VS) process, vapor-liquid-solid (VLS) process and vapor-solid-solid (VSS). The following three sections will focus the introduction of these synthesis mechanisims.

2.2.1 Vapor-Solid Process

Although the exact mechanism for 1D growth directly from the vapor phase is still not fully understood, vapor-solid process has been explored by many researchers to synthesize 1D nanostructures from a variety of materials. As early as 1950s, it was reported that acicular structured oxides of metals such as Cu, Cr, Fe, Pb, Ti, W, and Zn could be produced on the external surfaces of the corresponding metals when they were heated in air at certain temperatures[20].

The VS process is believed to be a kinetics driven anisotropic crystallization process. From experimentally and theoretically studies on the kinetics of nanowire growth[21,22], The 2D nucleation probability (P_N) on the surface of a nanowire is expressed as:

$$P_N = B\exp(-\frac{\pi\sigma^2}{k^2T^2\ln\alpha}) \quad (2.1)$$

where B is a constant; σ is the surface energy of the solid nanowire; k is the Boltzmann constant; T is absolute temperature; α is the supersaturation ratio determined by $\alpha=p/p_0$ (p is the actual vapor pressure and p_0 is the equilibrium vapor pressure corresponding to T). According to Equation 2.1, we can clearly see the lower the surface energy, the larger the 2D nucleation probability. On the other hand, an atom adsorbed on a low-energy surface has a low binding energy and it has a low probability of absorption. Competition and coordination of these two effects are responsible for the formation of the low-index crystal planes enclosing the 1D nanostructures. The temperature and the supersaturation

ratio are two parameters controlled by experimental conditions. Higher temperature and larger supersaturation ratios facilitate 2D nucleation, resulting in the formation of thin films. In VS growth process, temperature and supersaturation ratio are the two dominant factors controlling the morphology of deposited products.

Therefore, the VS growth can be considered as starting from "self-catalytic" initiation. When there is no catalyst used in the synthesis, the formation of 1D nanostructures is normally dominated by the VS process, such as the growth of oxide nanobelts structures. A possible mechanism has been proposed in VS growth of ZnO nanobelts[23], as illustrated in Figure 2.4.

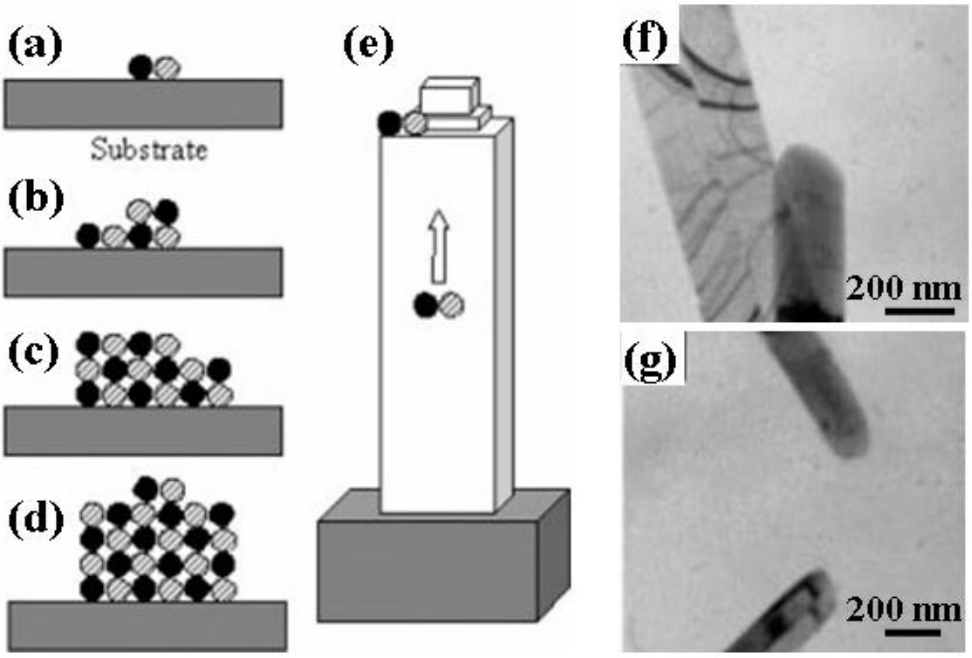

Figure 2.4: (a-e) A proposed growth mechanism for ZnO nanobelts through a VS process. (f, g) The growth front and end of a ZnO nanobelt showing no trace of catalyst.

After vaporization at high temperature, the ZnO molecules condensed onto the substrate placed on the lower temperature region as shown in Figure 2.4a and the cation-anion will be arranged in such a lowest energy way that a proper cation-anion coordination is

preserved to balance the local charge and structural symmetry forming a small nucleus as in figure 2.4b. Newly arriving cation-anions will continue to deposit on the formed nucleus while the local vapor supersaturation is remained. Due to the high mobility of the molecules at the deposition temperature (~800ºC), the molecules will accumulate onto the rough growth front or edges, resulting in an expanded surface area as in figure 2.4c. The rough structure of the tip leads to a rapid accumulation of incoming molecules, as a result the fast formation of a nanobelt (figure 2.4d) and after some time a long nanobelt is formed (Figure 2.4e). Figure 2.4f and g show ends of ZnO nanobelts, in which the growth fronts are a rounded, indicating their atomic-scale roughness with the presence of steps, ledges, and kinks, where the molecules are most likely to stay resulting in an anisotropic 1D growth.

2.2.2 Vapor –Liquid-Solid Process

Since the nucleation and growth are only controlled by the temperature and supersaturation ratio, it is hard to achieve precise control over the growth. Improved control can be realized by introducing a metal catalyst to guide the precipitation such that now growth is typically through a VLS process. Compared to VS process, the mechanism of VLS process is much better understood.

The VLS process was originally discovered by Wagner et al to produce silicon whiskers in 1964[24], and later adapted to one-dimensional nanostructure growth by Lieber, Yang, and many other research groups[25,26].

For VLS growth, it is very important to select the right metal catalyst. As a major requirement, there should exist a good solvent capable of forming a liquid alloy with the source material, and ideally they should be able to form eutectic compounds. In addition,

the catalyst should be chemically stable with respect to the source material and oxygen as there is always the inclusion of trace amounts of O_2 in the reaction systems. Consequently, gold, as a noble catalyst, is the first choice for catalyzing a VLS growth of various materials[27,28].

There are several benefits in applying the VLS process for 1D nanostructure growth. The first is dimensionality control. It has been demonstrated that the diameter of the catalyst directly affects the cross-section of the resulting 1D nanostructures[27,28]. In addition to size control, the VLS affords the capability of site-specific growth. The catalysts act as preferential nucleation sites, allowing for patterned or arrays of nanostructures to be synthesized. Moreover, VLS provides the ability to synthesize aligned nanostructures, once a single crystal substrate is carefully chosen based on their lattice parameters. One of the challenges faced by the VLS process is the limitation in forming 1D nanostructures with complex components, because the simpler phases always tend to be precipitated from the alloy when the alloy is formed by multiple elements. For example, it seems impossible to fabricate three- or four-element piezoelectric or superconducting 1D nanostructures, such as PZT, through a VLS process.

2.2.3 Vapor –Solid-Solid Process

The mechanism of growing ZnO nanowire arrays by thermal deposition process is used to be believed to be VLS process. The recent in-depth study on the growth process of well aligned ZnO nanowire arrays by M Kirkham et al. reveals the growth mechanism is Vapor Solid Solid process rather than Vapor Liquid Solid process[29].

By XRD technique, it is confirmed that the nanopartical Au catalyst has not formed alloy with Zn. The lattice parameter remains the same for the catalyst Au nanoparticle

exporsed to ZnO vapor or not, which indicates there is no impuities in the Au catalyst particle. The growth temperature is around 500 ˚C from reports on growing ZnO nanowires, which is almost 200˚C below Au rich Au-Zn eutectic temperature. All the evidences show the catalyst nanoparticle remains solid during the synthesis for there is no eutectic depression of the melting point. The growth proceeds by surface diffusion rather than bulk diffusion.

The preferred growth mechanism for growing aligned ZnO nanowire arrays will be addressed below. ZnO vapor is absorbed on the surface of the solid gold nanoparticles. The incoming ZnO vapor causes the percentage of the ZnO component in the droplet to increase and ultimately supersaturates. ZnO is precipitated out at the solid-liquid interface, and growth continues until the source vapor is cut off.

2.3 Growth Aligned ZnO Nanowire Arrays

The synthesis method in this dissertation for growing well aligned ZnO is typical VSS process. Details will be discussed below.

2.3.1 Experiment for Synthesizing Aligned ZnO NW Arrays

Undoped *c*-plane oriented GaN film with a thickness of 2 μm that were grown on *a* plane sapphire wafer was used as substrates. A thin layer of gold (7-8 nm) was coated on the top of GaN via plasma sputtering, which acted as catalysts to guide the growth of ZnO nanorods. The source materials were the mixture of equal mount (by weight) of ZnO power and graphite power, which was ground and put into an alumina boat. Then the boat was loaded in the center of an alumina tube (150 cm long, 4 cm inner diameter), where the substrate was placed 10 cm away from the source material at the downstream side. The tube was placed in a horizontal tube furnace (Model F79345 from

Barnstead/Thermolyne Co.) with cooling water running through the outside of the tube at the ends. After pumping the system down to 2×10^{-2} mbar, a premixed gas (Ar and O_2) was introduced into the system with a flow rate of 50 sccm to bring the pressure back to 30 mbar. The furnace was then heated to 950˚C at a heating rate of 50˚C /min and the temperature was held at the peak temperature during the growth for 30 min. Finally, the system was slowly cooled down to room temperature under flow gas.

2.3.2 TEM and SEM Characterization

The as-synthesized ZnO nanorods were first examed by scanning electron microscopy (SEM). Figure 2.5a shows a typical image of ZnO nanorods grown on GaN substrate with a good alignment, in which almost all of the ZnO rods have the same lengths and same diameters and are oriented perpendicular to the substrate. This sample was grown under the condition of 2 % O_2 (by volume) and 30 mbar chamber pressure. The well-aligned structure uniformly covered all of the area of the GaN substrate. The inset in figure 2.5a shows a top view of the aligned ZnO nanorods, where only the very bright gold catalyst tips can be observed. It also confirms that almost every single nanorod is perpendicular to the substrate and there are no side branches.

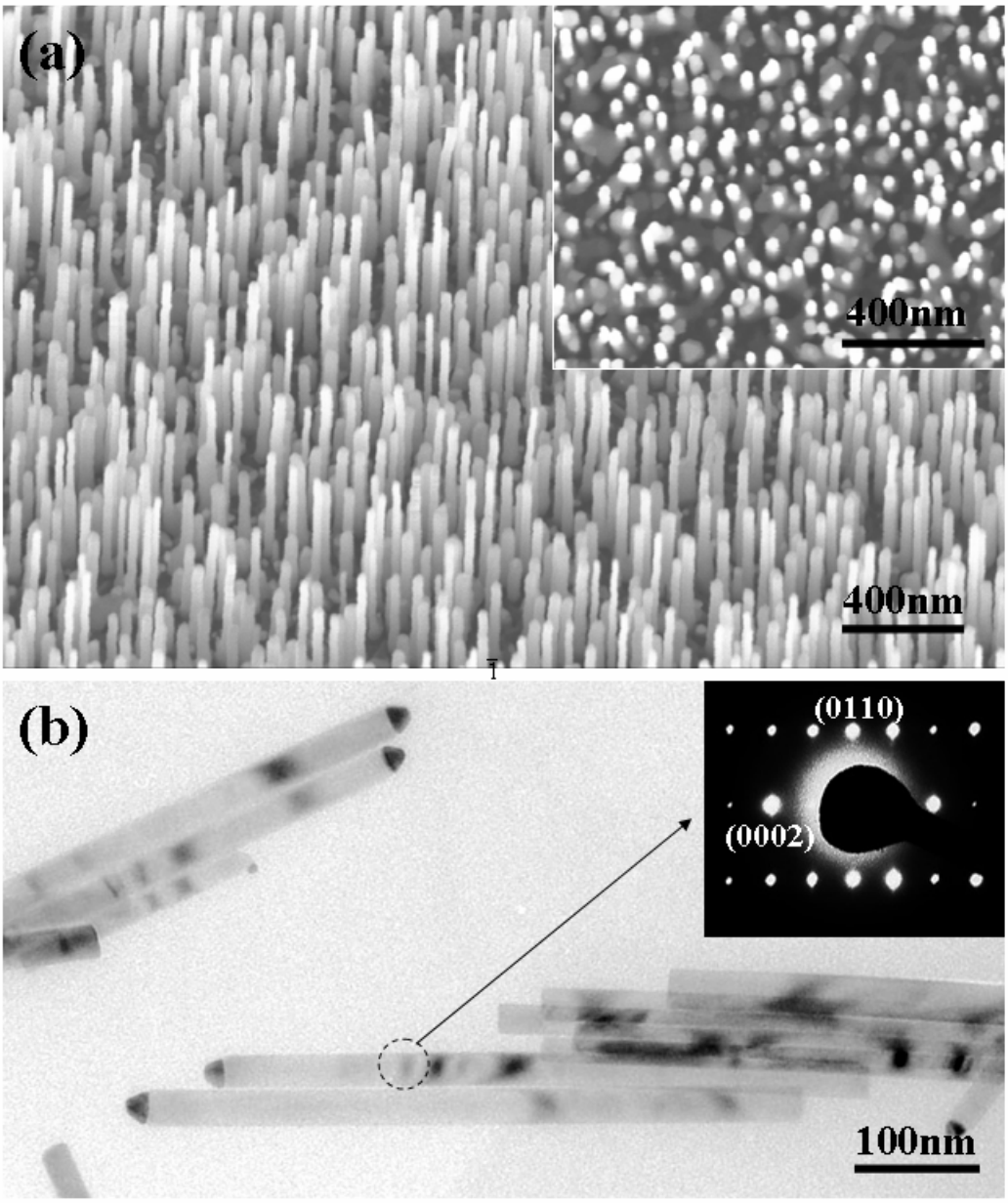

Figure 2.5: Aligned ZnO nanorods on GaN substrate. (a) Side view SEM image, the inset is the top view SEM image of the sample; (b) TEM image of ZnO nanorods, the inset is an electron diffraction pattern taken from one ZnO rod.

The crystallography of ZnO rods is characterized by Hitachi HF2000 transmission electron microscopy (TEM). Figure 2.5b shows a typical TEM image of the ZnO

nanowires/nanorods. Each nanorod is a single crystal and exhibits a uniform thickness. From the ZnO nanorod a diffraction pattern was recorded as shown in the inset of Figure 2.5b, which reveals the growth direction is along [0001] and the six sides facets are $\{11\bar{2}0\}$.

2.3.3 "Phase Diagram" for Aligned ZnO NW Arrays

In the synthesis experiments, the oxygen partial pressure and the system total pressure played key roles in the growth of ZnO nanorods. With different oxygen volume percentage and different chamber pressure, the quality and growth behavior of the ZnO nanowires are strongly affected. We have carried out over *100* growth experiments under different growth conditions, which were designed to quantitatively define the best combination of the O_2 partial pressure and the chamber pressure for growth of aligned ZnO nanowires. For consistency, all of the samples were collected at the 880 temperature zone, which is 10 cm away from the source materials. It is possible to observe deposition on other temperature zone while the experimental conditions are changed. However, it's sufficient to illustrate the effects of oxygen partial pressure and chamber pressure just within one temperature zone. The O_2 partial pressure varied from 1 to 4 vol.% and the system pressure varied from 1.5 to 300 mbar. Since the growth system was first pumped down to 2×10^{-2} mbar, the system pressure was brought back to the growth pressure of 1.5 to 300 mbar, the oxygen coming from the residue air only contributed 0.28% to 0.0014% towards the entire oxygen content, which were much less than the percentage of O_2 in the flow gas. Therefore, the partial pressure of O_2 was considered to be the percentage of the O_2 introduced in the flow gas.

The experimental results are summarized in figure 2.6, which is a "phase diagram" for the O_2 partial pressure and system pressure, under which the optimum conditions for growing aligned ZnO nanowires are presented. This phase diagram was determined for the furnace system described in the experimental section.

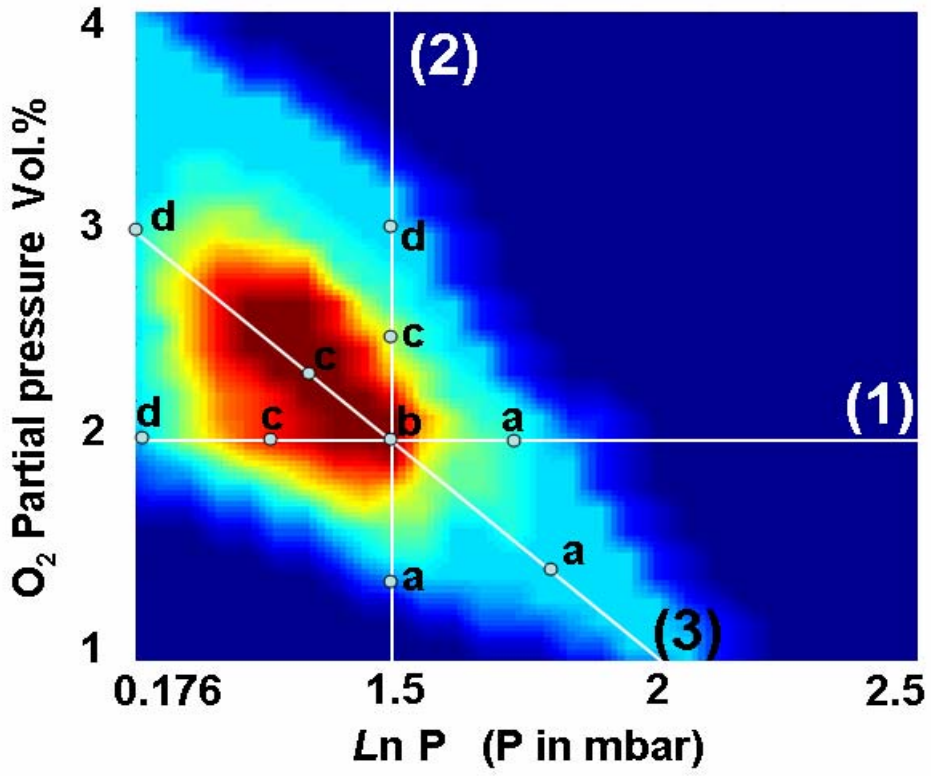

Figure 2.6 "Phase diagram" that correlates oxygen partial pressure (in volume percent in the carry gas) and the growth chamber pressure (plotted in logarithm and P is in unit of mbar) for growing aligned ZnO nanorods. This phase diagram was generated by over 100 points with different experimental conditions, where this point matrix was broadened and smoothed by MatLab to form a continuous 2D diagram. The synthesis Line (1) is the line with constant oxygen partial pressure; line (2) is the line with constant system pressure; line (3) is the line with linearly varying oxygen partial pressure and system pressure.

As shown in figure 2.6, the horizontal axis is the logarithm of the total chamber pressure; the vertical axis is the oxygen partial pressure, and the quality of the grown ZnO nanowires are represented by different colors. The quality of the nanowires is characterized by their uniformity, density, length and alignment. In the phase diagram, dark red represents the best growth condition, where a perfect alignment of ZnO nanorods

with a high density and uniform length and thickness were achieved. The grown is good in the red area, while the density is lower and the nanorods are shorter. In the green and light blue area, the grown is poor, where only a little amount of short nanorods was found. No growth was found in the dark blue region. This phase diagram provides the road map for growing high quality aligned ZnO nanowires.

In order to clearly demonstrate the effects of total chamber pressure and O_2 partial pressure to the final results, three sequences are highlighted in the phase diagram: fixed O_2 partial pressure but with variable chamber pressure (line 1); fixed system pressure but with variable O_2 partial pressure (line 2); and linear increased O_2 partial pressure with decreasing system pressure (line 3). Four representative points on each line are picked up to present the quality of the grown nanowires under the defined growth conditions.

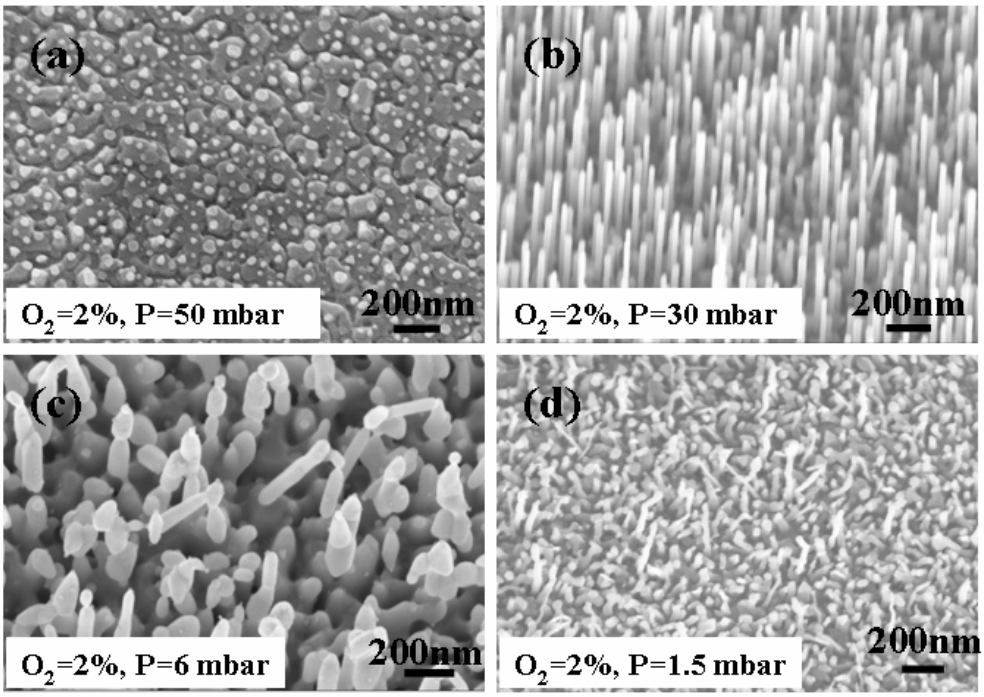

Figure 2.7 SEM images of ZnO nanorods grown under the conditions of 4 green points along line (1) in figure 2.6 under constant oxygen partial pressure (2%) but variable chamber pressure: (a) 50 mbar; (b) 30 mbar; (c) 6 mbar; (d) 1.5 mbar.

Figure 2.7 presents SEM images of four samples received under the conditions of 2% fixed O_2 partial pressure (1 sccm oxygen, 49 sccm argon) but 4 different chamber pressures: 50 mbar, 30 mbar, 6 mbar, and 1.5 mbar as shown in Figure 2.7a, b, c, and d, respectively. In figure 2.7a, which represents the results with the highest system pressure among the four experiments, no nanowire was formed but only gold catalyst particles were found, which was confirmed by EDS. With the decreasing of system pressure to 30 mbar, a perfect alignment of ZnO nanowires were achieved, as shown in Figure 2.7b. When the system pressure dropped to 10 mbar, ZnO nanorods became shorter and randomly orientated, as shown in Figure 2.7c. By further dropping the system pressure to 1.5 mbar, only a few thin nanorods were deposited on a continuous ZnO film as in Figure

2.7d. This regular change in the ZnO morphology is contributed to the increased Zn vapor concentration while the system pressure decreased.

In the carbon-thermal evaporation process, the Zn vapor source is dominated by reaction:

$$ZnO(s) + C(s) \Leftrightarrow Zn(v) + CO(v) \qquad (2.2)$$

This reaction is favorable in high temperature. Once the vapors are transported to the cooler region where the substrate is located, the Zn vapor is deposited on the surface of the catalyst and reoxidized, resulting in the growth of nanowire. Since the amount of Zn vapor is determined by the local temperature, thus, the rate at which the Zn vapor is produced can be assumed to be a constant under different chamber pressures. Consequently, when the total system pressure drops, the partial pressure of Zn vapor increases. When the system pressure is too high, Zn vapor may not reach supersaturation, thus, no deposition occurs on the surface of the catalyst particles, resulting in no growth at all (Fig. 2.7a). When the system pressure is too low, Zn vapor may be over supersaturated, the vapor deposits not only on the surface of the Au catalyst but also the surface of the GaN substrate, resulting in formation of nanowires as well as a thin film on the substrate surface (Fig. 2.7d). A high quality aligned ZnO nanorods can only be achieved when a reasonable supersaturation level of Zn vapor is reached at a moderate system pressure, which is around 30 mbar in our growth condition.

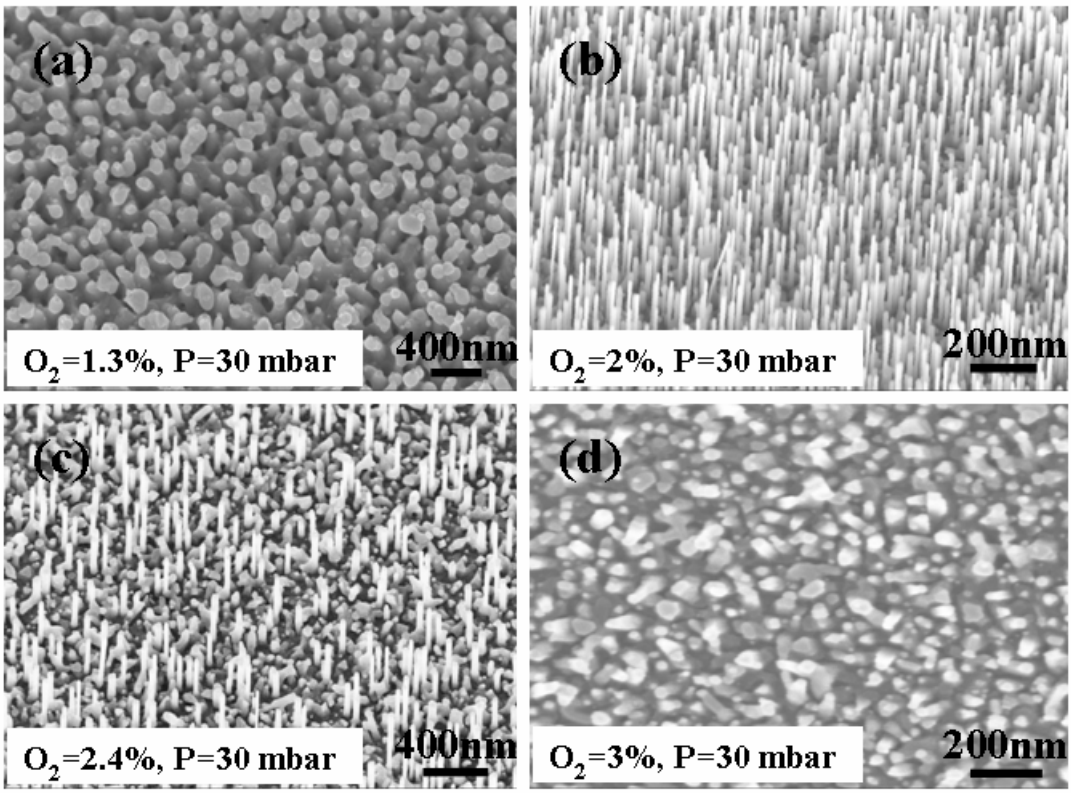

Figure 2.8 SEM images of ZnO nanorods grown under the conditions of 4 green points along line (2) in figure 2.6 under constant chamber pressure (30 mbar) but variable oxygen partial pressure: (a) 1.3% ; (b) 2%; (c) 2.4%; (d) 3%

The effect of O_2 partial pressure is illustrated in Figure 2.9, in which SEM images of a, b, c and d represent the typical results of ZnO deposition at O_2 partial pressure of 1.3%, 2%, 2.5% and 3%, respectively, with a fixed chamber pressure of 30 mbar. At a very low O_2 partial pressure (1.3%), only small ZnO dots were nucleated, as shown in Figure 2.8a. By increasing the O_2 partial pressure to 2%, good alignment of ZnO nanowires was achieved (Figure 2.8b). When the O_2 partial pressure increased to 2.5%, as shown in Figure 2.8c, the density of ZnO nanorods dropped dramatically, as well as their

lengths. The growth of ZnO nanorods almost vanished once the O_2 partial pressure was set at 3% (Figure 2.8d).

There are three reactions that O_2 are involved in carbon-thermal evaporation process:

$$2C + O_2 = 2CO \qquad (2.3)$$

$$2CO + O_2 = 2CO_2 \qquad (2.4)$$

$$2Zn + O_2 = 2ZnO \qquad (2.5)$$

Zn vapor is still provided by equation (2.2). From Ellingham diagram, reaction (2.2) occurs only when the temperature is higher than 970˚C, while in our furnace, the furnace was just heated to 950˚C, thus, the question what make the local temperature high enough for reaction (2.2) to be possible? In the beginning when there was no other gas in the system, the main reaction involving O_2 is reaction (2.3), which generated heat as well as CO. The heat could be absorbed locally and possibly facilitate reaction (2.2) to produce Zn vapor. On the other hand, local concentration of CO could also increase, which could hinder the Zn vapor generation. Under the influence of these two effects, reaction (2.2) can not be fully accelerated and as a result, when the O_2 partial pressure was very low, sufficient Zn vapor can not be released to reach a reasonable supersaturation point for producing ZnO nanorods, as the situation shown in Figure 2.8a.

Once the partial pressure of O_2 was increased, additional O_2 can react with CO to form CO_2 (equation 2.4), which lowered the concentration of CO and generated heat as well. Both of these two effects facilitated reaction (2.2). Therefore, supersaturation of Zn vapor can be reached, leading to growth of high quality aligned ZnO nanorods, as shown in Figure 2.8b. However, when the partial pressure of O_2 was further increased, additional O_2 could react with Zn vapor generate from the source materials immediately to formed ZnO film/grain. We have examined this situation by introducing a lot more O_2 into the system, and found a layer of large ZnO nanorods/grain was formed on the surface of the source powders.[30] Consequently, the Zn vapor decreased again near the substrate and

little growth was found (Fig. 2.8d). In general, only moderate O_2 partial pressure (~ 2 vol.%) results in good aligned ZnO nanorods.

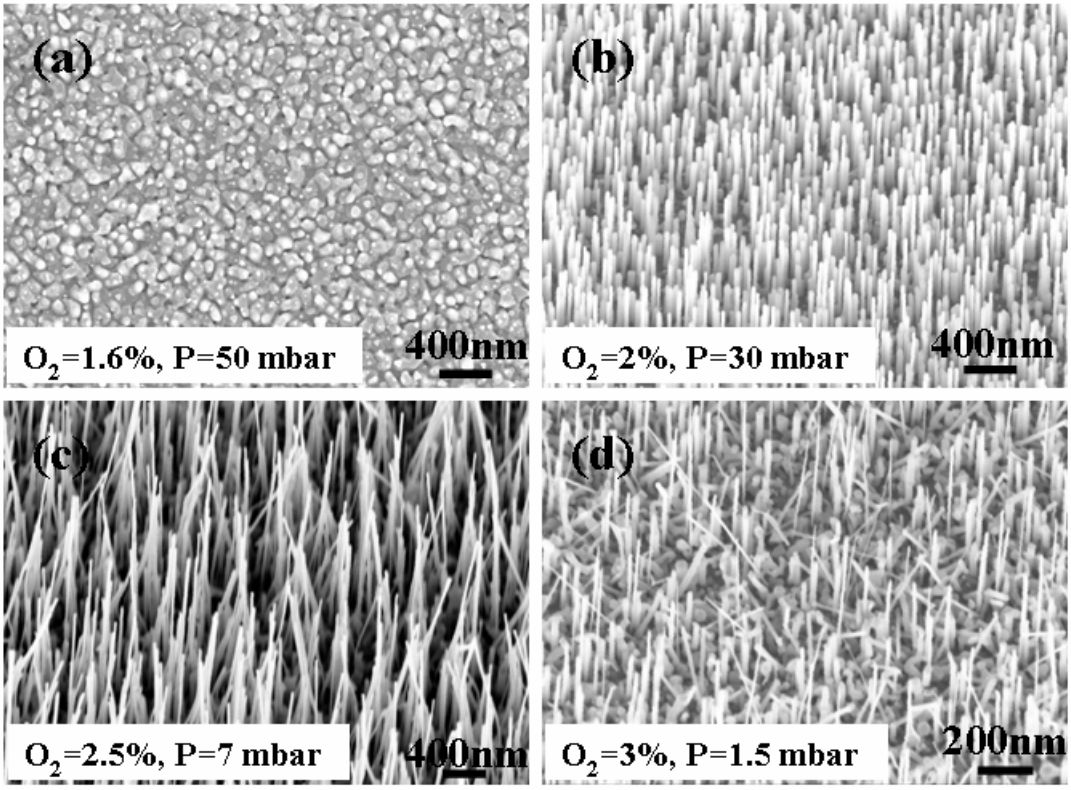

Figure 2.9 SEM images of ZnO nanorods grown under the conditions of 4 green points along line (3) in figure 2.6 by linearly adjusting the chamber pressure and oxygen partial pressure. (a) 1.6% oxygen partial pressure, 50 mbar chamber pressure; (b) 2% oxygen partial pressure, 30 mbar chamber pressure; (c) 2.5% oxygen partial pressure, 7 mbar chamber pressure; (d) 3% oxygen partial pressure, 1.5 mbar chamber pressure.

Four typical results of ZnO deposition carried out under linearly increased O_2 partial pressure with decreased chamber pressure are illustrated in Figure 2.9. The

experimental conditions selected are: (a) 1.6% O_2 at 50 mbar system pressure; (b) 2% O_2 at 30 mbar system pressure; (c) 2.5% O_2 at 7 mbar system pressure; (d) 3% O_2 at 1.5 mbar system pressure. Except point a, where both O_2 partial pressure and system pressure were intended to give a low Zn vapor concentration, all of the other three points in the phase diagram exhibited a reasonable growth of ZnO nanorods. This is because the decreasing of Zn vapor caused by increased O_2 could be compensated by reducing the chamber pressure, thus the reasonable supersaturation level of Zn vapor can be maintain in a relatively large range.

The "phase diagram" discussed here correlates the partial pressure of oxygen with chamber pressure for growing aligned ZnO nanorods on GaN semiconducting substrate via VSS process. Distinct from the conventional understanding about VSS growth process, both of the partial pressure of O_2 and total system pressure exhibited distinct effects on the final morphologies of deposited ZnO nanostructures. In our furnace system, the optimal condition for growing aligned ZnO nanorods was found to be 2% O_2 at 30 mbar system pressure at local growth temperature of 880˚C. The phase diagram presented here can provide a road map for fabricating aligned ZnO nanowires for large-scale and controlled nanowire synthesis.

2.3.4 Growth ZnO NW Arrays on Nitride Substrates

For the growth of aligned ZnO nanowires/nanorods, *a*-plane oriented Al_2O_3 (sapphire) single crystals have been used as substrates with the assistance of gold particles as catalysts, in which the growth is initiated and guided by the Au particle and the epitaxial orientation relationship between ZnO and Al_2O_3 leads to the alignment.[31,32] Two intrinsic problems are, however, associated with this technique, possibly limiting its application to devices. Al_2O_3 is a non-conductive material, making it difficult to utilize the aligned ZnO nanorods for electronic and optoelectronic devices. Also due to the

surface crystal structure, a lateral growth of side branches close to the substrate surface is almost inevitable during the early stages of growth. For technological applications, it is highly desirable to grow ZnO nanorods on a conductive or semiconductive substrate in order to fabricate heterostructure devices and to make electronic measurements. GaN, an important optoelectronic material with the same crystal structure as ZnO, has been used as a substrate for growing aligned ZnO nanorods by the metalorganic chemical vapor deposition (MOCVD) process due to their very close lattice match.[33,34] However, since no catalyst was used in this process, there was no control over the site distribution and density of the nanostructures.

In this section, perfectly aligned ZnO nanorods grown on semiconducting GaN, $Al_{0.5}Ga_{0.5}N$ and AlN thin-film substrates by a vapor-liquid-solid (VSS) phase process using gold as a catalyst will be discussed. The as-grown nanorods show no lateral growth but are vertically aligned on the substrate surface. Our results prove that ZnO nanorods can be epitaxially grown on $Al_xGa_{1-x}N$ thin film layers with any Al alloy composition ratio. Since the bandgap of $Al_xGa_{1-x}N$, which can also be *n*-[35] and *p*-type[36] doped, is tunable from 3.44 eV to 6.20 eV by changing the Al composition from 0 to 1, a bandgap tunable hetero-junction array of ZnO nanorods on a thin film substrate can be achieved, thus making them an ideal candidate structure for light-emitting diode arrays.

2.3.4.1 Synthesizing ZnO NWs on Nitride Substrates

MOCVD technique was employed for growing GaN, AlN and AlGaN epilayers[37, 38], which served as the substrate for the subsequent growth of ZnO nanorods. Undoped *c*-plane-oriented GaN and AlN thin films were grown on *a*-plane sapphire substrates to thicknesses of 2 μm and 500 nm, respectively. $Al_{0.5}Ga_{0.5}N$ epitaxial layers with a thickness ~205 nm were grown on a 500 nm-thick AlN buffer layer grown on *c*-plane

orientated sapphire substrate. A 7~8 nm-thick ~5 x 5 mm^2 gold catalyst layer was then deposited by plasma sputtering onto the epitaxial nitride substrates. The ZnO nanorods were grown through a vapor-liquid-solid process using a mixture of equal amounts (by weight) of ZnO and graphite powders that were loaded in an alumina boat located at the center of an alumina tube. To facilitate the reaction 2% (1sccm) oxygen was mixed with argon carrier gas at a flow rate of 49 sccm and the substrates were placed down stream in a temperature zone at ~850˚C. A horizontal tube furnace was used to heat the source materials to 950˚C at a rate of 50˚C/min and the temperature was held at the peak temperature for 30 minutes under a pressure of 30 mbar. Then the system was slowly cooled to room temperature under an argon flow.

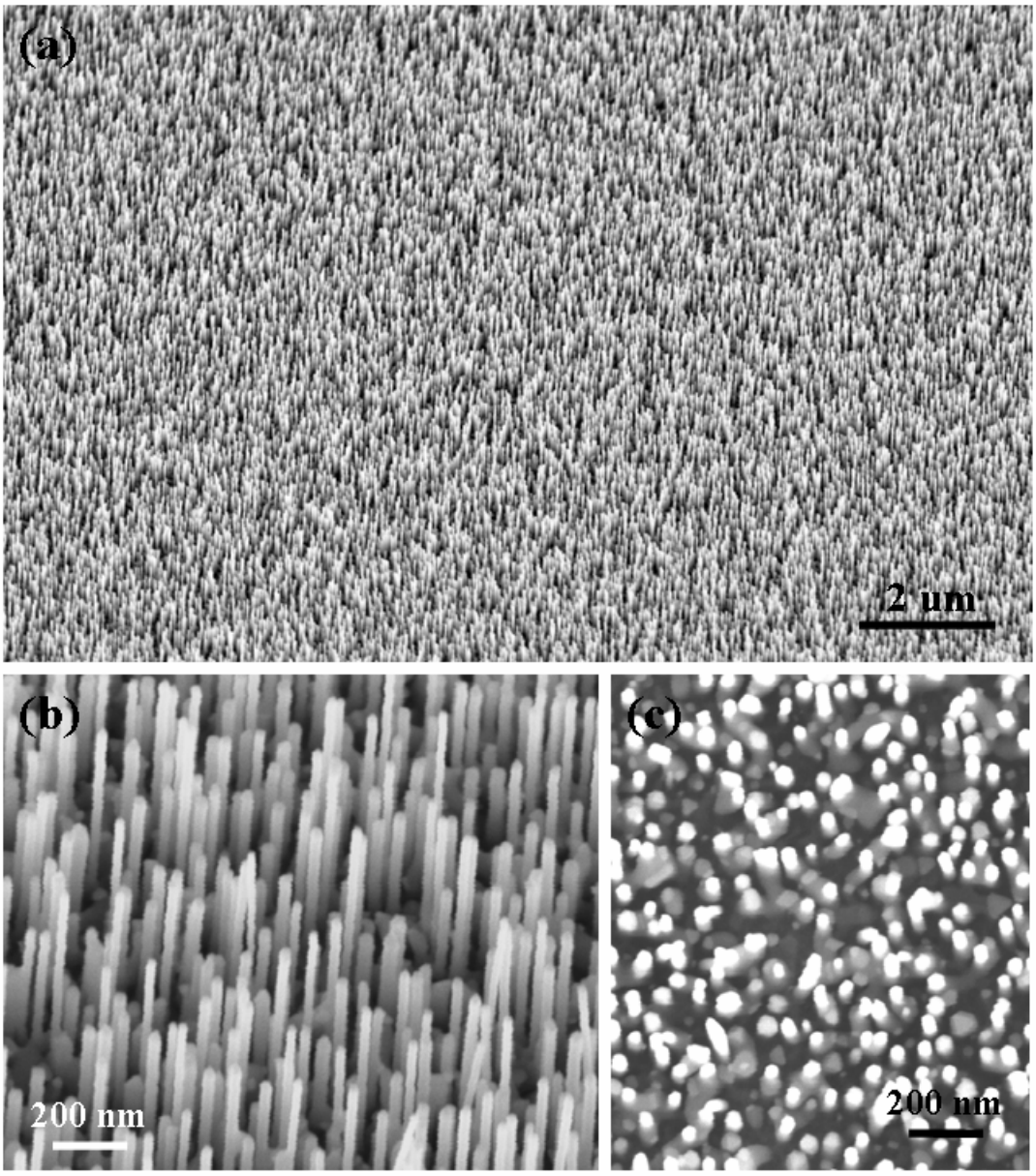

Figure 2.10 SEM images of aligned ZnO nanorods grown on a GaN substrate . (a) Low-magnification 30º side-view image; (b) High-magnification 30º side-view image; (c) High-magnification top-view image.

2.3.4. Sample Analysis

The as-synthesized aligned ZnO nanorods were first examined under a LEO 1530 field emission gun (FEG) scanning electron microscope (SEM) operated at 10 kV. A typical low-magnification SEM image of ZnO nanorods grown on GaN is shown in Figure 2.10a. All of the ZnO nanorods are straight and perpendicular to the substrate with a high uniformity across the entire substrate, indicating that this technique can be scaled up for large-area production. As shown from a higher magnification SEM image in Figure 2.10b, the ZnO nanorods exhibit uniform diameter. Figure 2.10c shows a top view of the aligned ZnO nanorods, where only the very bright gold catalyst tips can be observed. It also confirms that almost every single nanorod is perpendicular to the substrate and that there are no side branches, which is generally unavoidable when sapphire is used as substrate.

Highly aligned ZnO nanorods were also grown on $Al_{0.5}Ga_{0.5}N$ and AlN substrates under the same growth conditions, even though the lattice mismatch for these materials are larger than for GaN. Figure 2.11a~c gives the X-ray diffraction (XRD) spectra of the aligned ZnO nanorods samples grown on GaN, $Al_{0.5}Ga_{0.5}N$, and AlN substrates, respectively. In all three spectra, only diffraction from (0002) and (0004) atomic planes of ZnO are observed at 34.63^{o} and 72.76^{o}, respectively, indicating the high degree of nanorods alignment and their epitaxial relationship with the substrate. From the lattice constants of wurtzite GaN: a = 3.190 Å and c = 5.189 Å and wurtzite ZnO: a = 3.249Å and c = 5.207 Å, the lattice mismatch between the (0001) planes is 1.9%. Thus, in the XRD spectrum (Figure 2.11a), the peak from the GaN (0002) plane overlaps that of ZnO, while a double shoulder is observed on the (0004) peak. The epitaxial relationship between the ZnO nanorods and the GaN substrate layer is $(0001)_{ZnO} \parallel (0001)_{GaN}$, $[01\bar{1}0]_{ZnO} \parallel [01\bar{1}0]_{GaN}$. For the AlGaN system, although the lattice constant decreases from 3.190 (GaN) to 3.15 ($Al_{0.5}Ga_{0.5}N$) and to 3.110 (AlN) Å; and their lattice mismatch correspondingly increases from 1.8%, 3.0% to 4.3%; the epitaxial relationship is preserved as supported by the XRD spectra shown in Figure 2.11d and c. This figure also show that the diffraction peaks of

$Al_{0.5}Ga_{0.5}N$ and AlN are gradually separated from the ZnO peaks due to the increased lattice mismatch, whereas the ZnO (0002) and (0004) peaks remain sharp and clear.

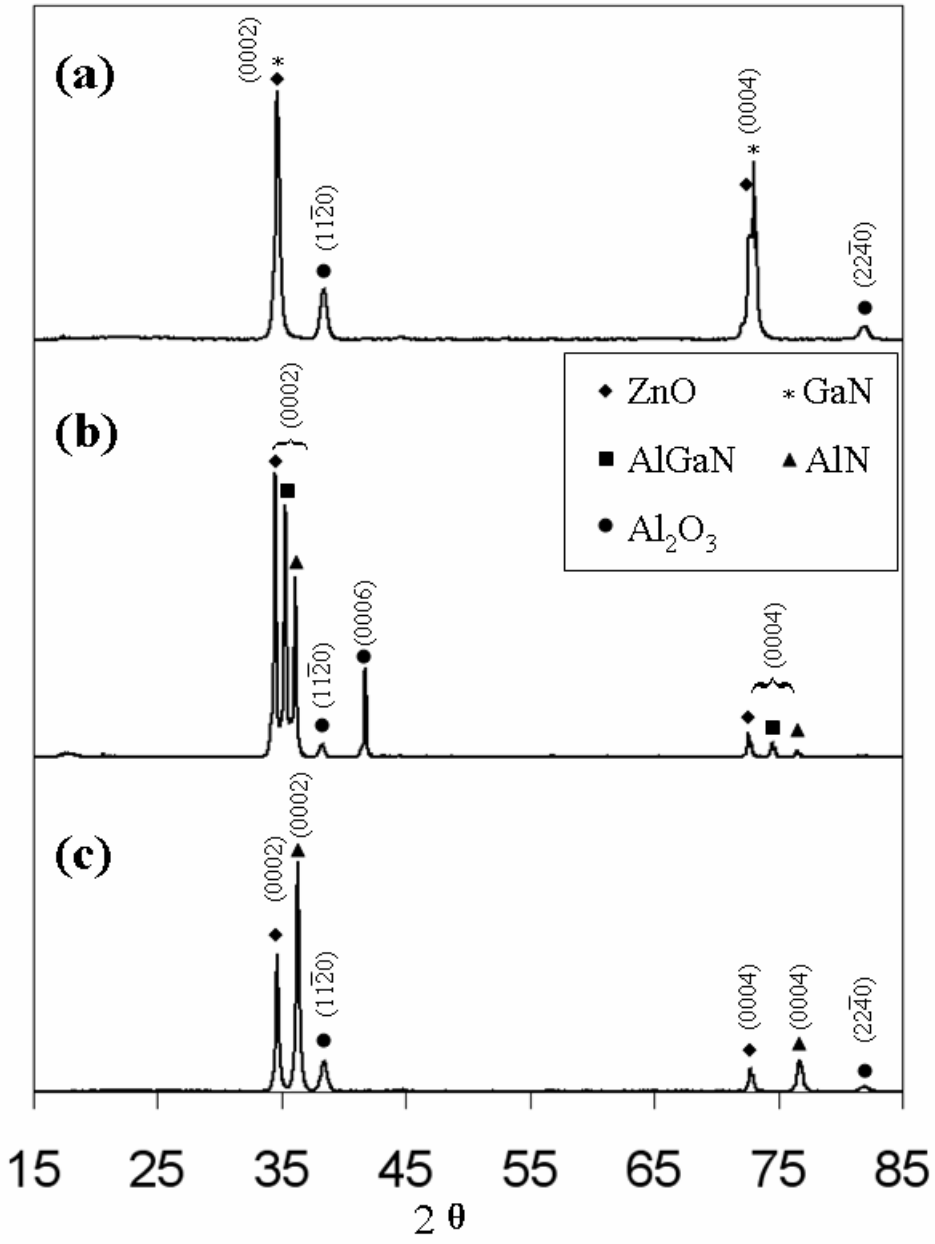

Figure 2.11 XRD spectra of aligned ZnO nanorods growing on GaN (a), $Al_{0.5}Ga_{0.5}N$ (b), and AlN (c) substrates.

Because both ZnO and the substrates have the same wurtzite structure, the deposited ZnO nanorods are confined to their six equivalent <01 $\bar{1}$ 0> directions and only grow along the [0001] direction, exactly following the substrate's crystal orientation. As a result, the possibility for ZnO nanorods to undergo lateral growth is rare, even around the catalyst nucleation sites where conditions are favorable for lateral growth, as shown in Figure 2.12a and b. Therefore, c-plane oriented $Al_xGa_{1-x}N$ substrates are ideal for the growth of aligned ZnO nanorods. On the other hand, the epitaxial relationship between ZnO and *a*-plane sapphire substrate is $(0001)_{ZnO} \parallel (11\bar{2}0)_{Al_2O_3}$, $[01\bar{1}0]_{ZnO} \parallel [0001]_{Al_2O_3}$. Although the lattice mismatch between $4[01\bar{1}0]_{ZnO}$ ($4 \times 3.249 = 12.996$Å) and $[0001]_{Al_2O_3}$ (12.99 Å) is almost zero, there is only one direction that is defined by this epitaxial relationship because the $(11\bar{2}0)$ plane of Al_2O_3 is a rectangular lattice but the (0001) plane of ZnO is a hexagonal lattice. As a result, the lateral growth of ZnO side branches was always observed for *a*-plane sapphire substrates.

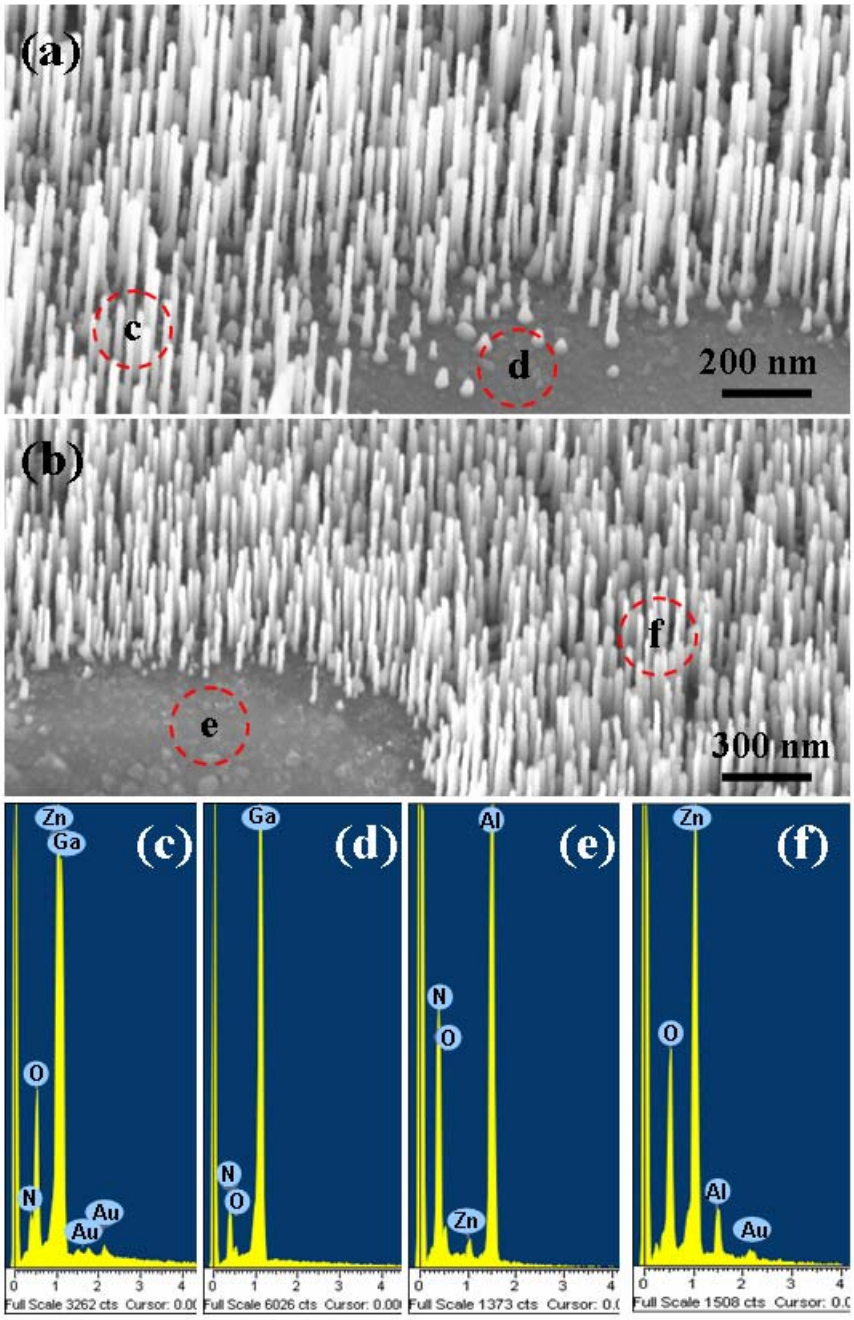

Figure 2.12 SEM images of ZnO nanorods growing on GaN (a) and AlN (b) substrates at the edge of catalyst layer; (c - f) EDS spectra of the corresponding circled region in (a) and (b).

The properties of catalytic particle initiated growth were further investigated using energy-dispersive X-ray spectroscopy (EDS) during the SEM measurements. Figure 2.12a

and b are SEM images of ZnO nanorods grown around the gold catalyst on GaN and AlN substrates, respectively, in which the catalyst boundary is clearly marked by the growth of aligned ZnO nanorods. EDS measurements were performed on the nanorod regions and the exposed substrate. Within the nanorod regions (Figure 2.12c and f), strong signals from zinc and oxygen were detected with a small gold signal originating from the Au film which acted as the catalyst and a portion of which remained at the tip of ZnO nanorods. Also small signals of Ga, Al and N were observed from the GaN and AlN substrates. However, on the exposed substrate (Figure 2.12d and e), only strong signals from the substrate materials were detected. Therefore, unlike the non-catalyst technique, such as MOCVD, which lacks of control over the growth position, the VSS process can precisely position the aligned ZnO nanorods by patterning the gold catalyst, while the uncovered substrate area remains chemically and structurally unchanged. Moreover, an almost perfect vertical alignment of ZnO nanorods without lateral growth can be achieved using the VSS technique demonstrated here.

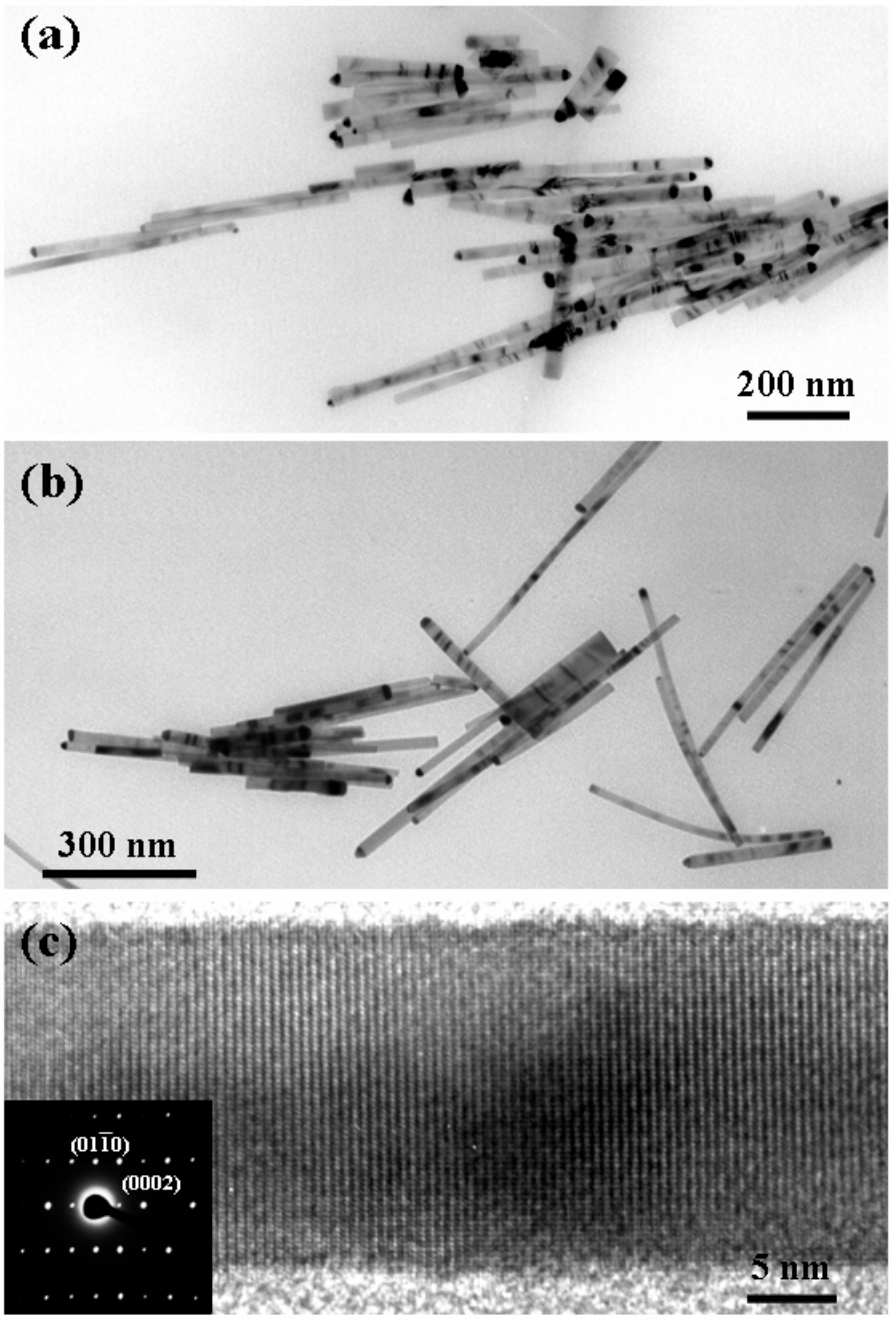

Figure 2.13 Low-magnification TEM image of ZnO nanorods grown on GaN (a) and AlN (b) substrates; (c) High-magnification TEM image of a single ZnO nanorod; inset: the corresponding electron diffraction pattern of the ZnO nanorod showing in (c).

Transmission electron microscopy (TEM) was also performed for size and crystal structure analysis using a Hitachi HF2000 TEM operated at 200 KV. The lower magnification TEM images obtained for ZnO nanorods grown on GaN and AlN substrates are shown in Figure 2.13a and b, respectively. From ~200 nanorods recorded on TEM images, the average length of ZnO nanorods grown on GaN was measured to be 434 nm, while the ZnO nanorods grown on AlN substrate were a little longer, ~500 nm. However, their length distributions are very close ±118 and ±120 nm for ZnO nanorods grown on GaN and AlN substrates, respectively. The average diameter was 28 ± 6 nm for ZnO nanorods grown on GaN is, and 22 ± 2 nm for those deposited on AlN. The smaller size of the ZnO nanorods on AlN is possibly due to the larger lattice mismatch between ZnO with AlN. The ZnO nanorods are single crystal (Figure 2.13c), the growth direction is [0001] and the six side facets are $\{11\bar{2}0\}$.

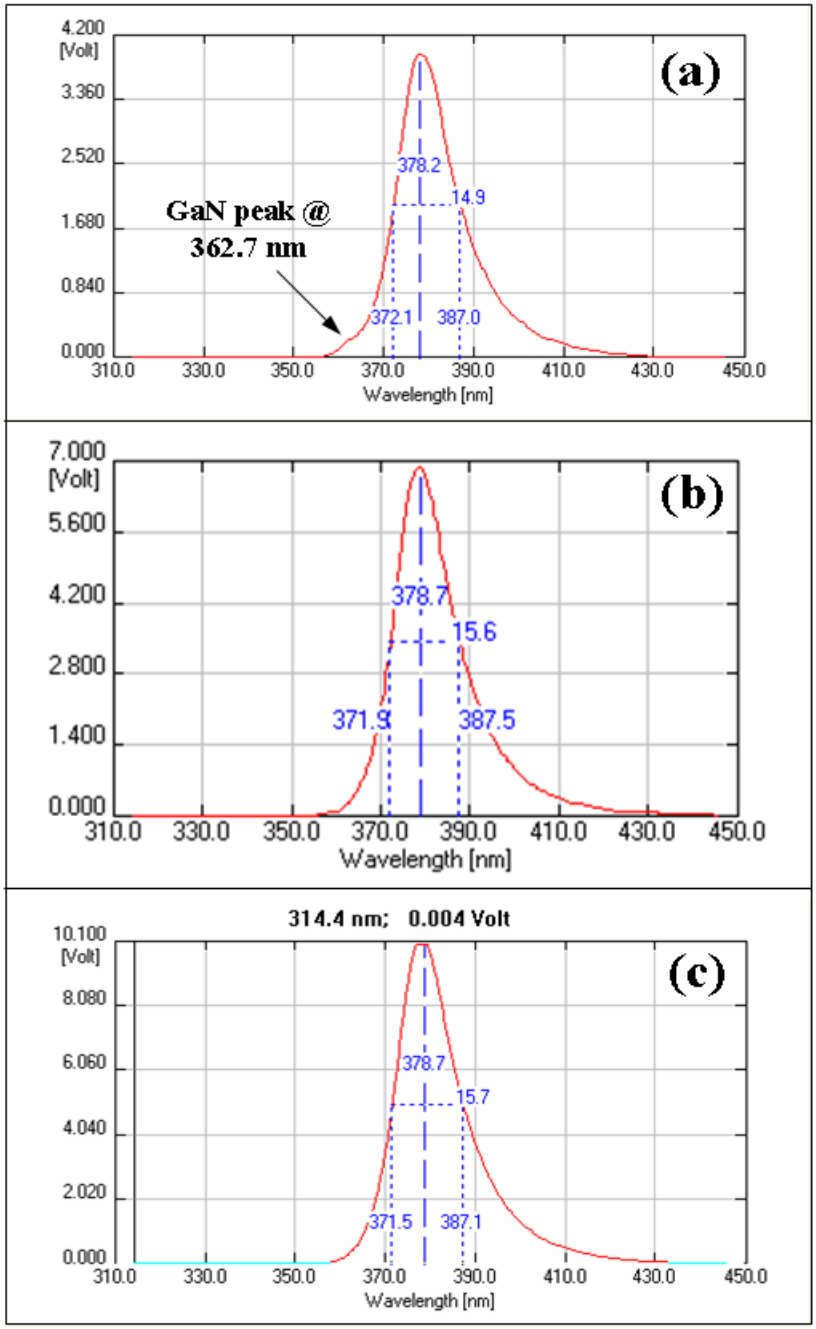

Figure 2.14 Photoluminescence spectra (300K) of aligned ZnO nanorods grown on GaN (a), $Al_{0.5}Ga_{0.5}N$ (b), and AlN (c) substrates.

Room-temperature photoluminescence properties were measured for ZnO nanorods arrays grown under the same conditions on GaN, AlGaN and AlN substrates

(Figure 2.14a~c) using a 266 nm Nd:YAG Q-switched laser with an average power of 1.9 mW as the excitation light source. A Si photodetector is used to measure the PL. All of the samples exhibited a strong luminescence peak at ~378 nm corresponding to the near bandgap emission of ZnO, an identical peak shape with a peak width at half intensity of ~15 nm. For the PL spectrum of ZnO nanorods on GaN, a small peak at 362.7 nm was also detected, which corresponds to the bandgap of GaN (3.44 eV). Due to the increased bandgap when Al was introduced into the GaN lattice, the PL peaks from the substrate are blue shifted and thus no additional substrate-related peaks were observed from ZnO nanorods grown on AlGaN and AlN substrates.

Although the PL peaks have an identical shape, their peak intensity varies significantly. The highest PL signal intensity, which was more than 10 volts, was measured from ZnO nanorods grown on AlN (Figure 2.14c) and the lowest from ZnO nanorods grown on GaN, only ~ 4 volts as shown in Figure 2.14a. The PL peak intensity from ZnO nanorods grown on AlGaN, exhibited an intermediate peak intensity of ~7 volts (Figure 2.14b). Since the density of nanorods grown on GaN, AlGaN and AlN substrates are calculated from the SEM images to be 146, 70 and 157 per μm^2, respectively, the relative PL intensities are not linearly related to the nanorod density. Due to the wide bandgap of AlN (6.20 eV), the luminescence from ZnO can not be absorbed by AlN, but the proximity of the bandgap of GaN to ZnO can cause absorption of the emission from the nanorods grown on GaN.

CHAPTER 3

MECHANICAL PROPERITY OF ZNO NW ARRAYS

Understanding and measuring the mechanical property of as-synthesized aligned ZnO nanorods not only improve the understanding of basic properties of nanomaterials but also are essential to make durable and reliable nanodevices based on them.

3.1 Measurement Method

In this section, the discussion is focusing on the methods to measure aligned NW arrays. For the typical small dimension of NWs, it is hard to measure the mechanical property. Researchers have invented a few methods to solve the essential problems in application of NWs for nanodevices fabrication.

3.1.1 General Review

Characterizing the mechanical properties of nanowiress/nanotubes/nanorods (NWs/NTs/NDs) is of great importance for their applications in electronics, optoelectronics, sensors and actuators. There are several techniques that have been developed for measuring the elastic properties of individual NTs. The technique demonstrated by Lieber et al.[39] was to quantifying the deflection of a carbon NT that was affixed at one end and the other end was free to be deflected by an AFM tip. The NT was laid in parallel to a solid substrate, and the elastic modulus of a carbon NT was received from the force-deflection curve. The technique by Wang et al. [40, 41] relied on the electromechanically resonance of a NT/NW by in-situ transmission electron microscopy (TEM). The resonance was stimulated by applying an AC voltage across two electrodes, one of which was a carbon NT that was glued to a metal tip affixed on a specimen holder.

The resonance frequency together with the geometrical parameters of the NT provided by TEM yielded the elastic modulus. The technique of Yu et al. [42] used two AFM tips to stretch a carbon NT that was glued at both ends to the two tips, respectively; the stretching force-displacement curve gave the tensile strength and elastic modulus. A technique developed by Salvetat et al. [43, 44] used an AFM tip to bend a NT or a bundle of single-walled NTs lying across a hole in a solid substrate. Quantifying the thermal vibration amplitude of a NT in TEM also yielded its elastic modulus.[45] For all of these techniques, the NT have to be removed from the substrate used in the growth and are manipulated for the measurements.

Growth of aligned NTs/NWs is of great importance for many technological applications. Elastic properties of aligned carbon NTs have been measured by an "indentation" method [46], in which a large-size tip was pushed downward against the aligned NTs so that many NTs are in contact with the tip and its side surface. By recording the force-displacement curve, the average number of NTs that were in contact with the tip and the contacting area of the NTs with the tip, an average elastic modulus of the NTs was received. This method requires that the density of the nanotubes is high and all of the nanotubes have the same size and length, and the measured result is a statistical average of all the NTs

3.1.2 Method for Measuring Mechanical Property of Aligned ZnO

In this part, I demonstrate an alternative AFM based technique for measuring the elastic properties of each and every aligned ZnO NWs in the range of the tip scan. By simultaneously recording the topological image and lateral force image in the AFM contacting mode, the elastic modulus of individual NWs in the scanning range can be

derived. This technique allows a measurement of the mechanical properties of individual NWs of different lengths in an aligned array without destructing or manipulating the sample.

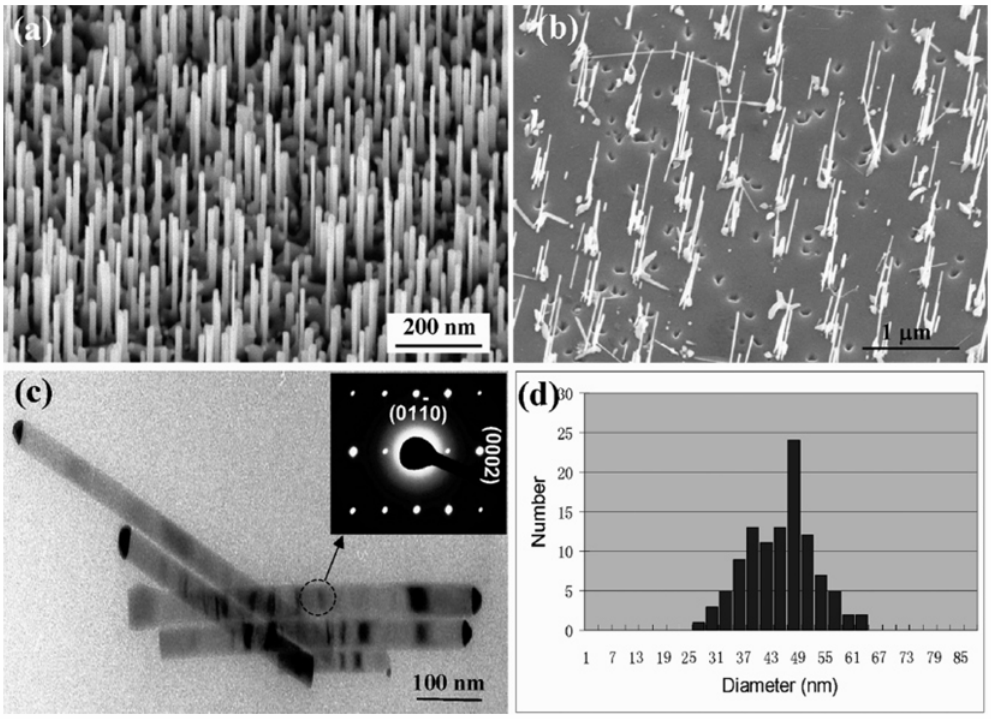

Figure 3.1 (a, b) SEM images of ZnO nanowire arrays grown on sapphire surfaces. (c) TEM image of the nanowires with gold catalyst at their tips. Inset is an electron diffraction pattern recorded from a nanowire. (d) Statistical distribution in nanowire diameter measured from TEM images.

The aligned ZnO NW arrays were grown using gold as catalyst by a vapor-solid-solid method (VSS) process, as reported previously.[47] By choosing an appropriate substrate, the epitaxial growth of ZnO on the single crystal substrate, such as α–Al_2O_3, GaN, AlN or $Al_{0.5}Ga_{0.5}N$ [48], yields aligned ZnO nanowires. Figure 3.1a shows a scanning electron

microscopy (SEM) image of the as-grown ZnO nanowires on an α–Al_2O_3 substrate, showing well aligned distribution but a large variation in height/length. If the density of the NWs is too high and/or the NW is too long, the AFM tip is probably too big to reach the surface of the substrate without simultaneously touching two nanowires. For the purpose of our measurements, we have grown a NW array that has relatively less density or shorter length (Fig. 3.1b), so that the AFM tip can exclusively reach one NW and the growth substrate without touching another nanowire, thus, our calculation can be carried out with considering only one nanowire. Each NW is a single crystal and grows along [0001] and is enclosed by six $\{01\bar{1}0\}$ sides facets (Fig. 3.1c). The NWs exhibit a uniform shape and their size is measured from the TEM image to have an average diameter of 45 nm (Fig. 3.1d).

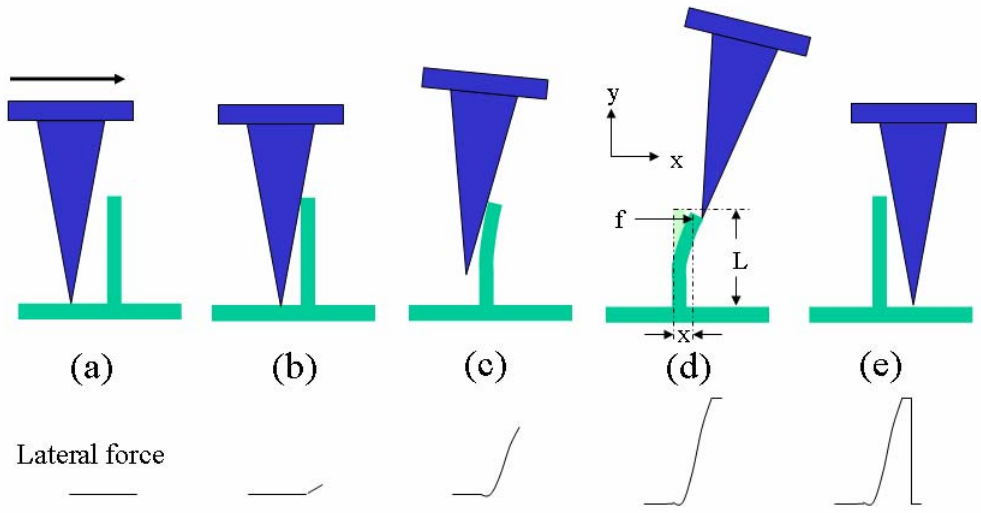

Figure 3.2 Procedures for measuring the elastic modulus of a nanowire in the AFM contacting mode.

The principle for the AFM measurement is illustrated in Figure 3.2. In the AFM contacting mode, a constant vertical force is kept between the tip and sample surface, and

the tip just scans over the top of the ZnO NW and its height is adjusted according to the surface morphology and local contacting force. Before the tip meets a NW, a small lateral force is observed due to the slow movement of the tip (Figure 3.2a). When it comes in contact with a NW, the lateral force increases almost linearly as the NW is elastically bent from its equilibrium position (Figure 3.2b, 3.2c). At the largest bending position as illustrated in Figure 3.2d, the tip crosses the top of the NW, then the NW is released; the lateral force drops suddenly and reaches the ordinary level (Figure 3.2e). We also assume that the NW has a very small vibration amplitude after being released by the tip, so that the subsequent movement of the tip is unaffected. With consideration the size of the NW and the measurement at room temperature, the thermal vibration of the NW at its free end can be ignored.

During this scanning process, the AFM works in the following way: when the tip contacts the NW, the scanner retracts at the same time in order to remain a constant contacting force, the cantilever is twisted and a rapid change in lateral signal is detected by the photo-detector. At the largest bending position, the scanner retracts to the highest position and the lateral signal reaches the maximal value. As the tip keeping moving at a low scanning speed, the bent NW is released by the tip, then the scanner extends quickly to touch the substrate to remain the constant set point; and the twisted cantilever immediately recovers to its equilibrium position. From the twist of the cantilever, the lateral force is measured.

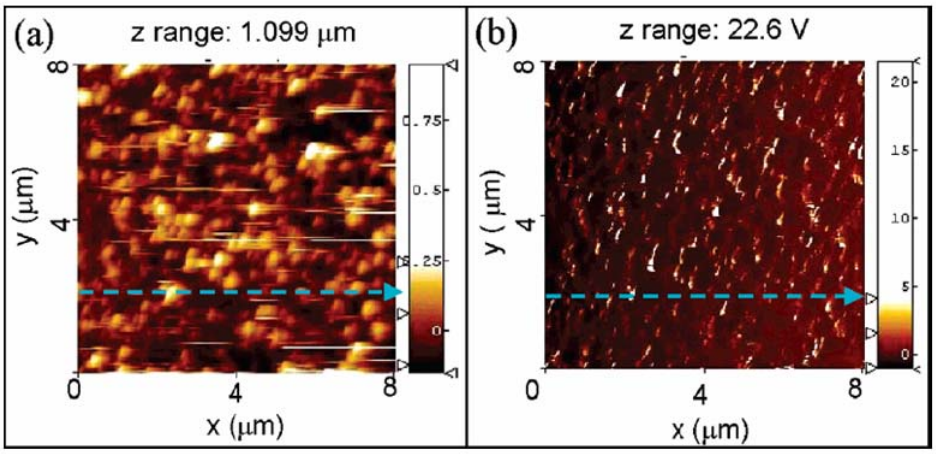

Figure 3.3 (a) Topological image and (b) lateral force image of the aligned ZnO nanowire arrays received in AFM contacting mode. The elastic modulus of each and every nanowire in the scanning range can be derived from these images.

Experimentally, the as-synthesized sample was loaded upwards on a specimen holder, and the tip of the AFM was scanned across the aligned NW arrays. Both the topography image (feed back signal from the scanner) and the lateral force image were recorded simultaneously. The images were recorded using a Si_3N_4 tip with 20^o cone angle. The scanning area varies from 25 to 100 μm^2. In contacting mode, the AFM tip keeps in touch with the sample surface at a constant force (set point). In this mode, as the tip scans over the vertically aligned NWs, the NWs are bent consecutively if their density is reasonably low. The bending force is captured in the lateral force image (Figure 3.3b), and the bending distance is directly recorded in the topography image (Figure 3.3a). The elastic modulus will be derived from the relationship between maximal lateral force and maximal bending distance.

The elastic property is derived based on following calculation. As the AFM tip swipes over the NW with its side and top surfaces in contacting with the NW, a lateral force is applied on the top of the NW. At the largest bending position (Figure 3.2d), the

applied lateral force reaches the maximum, so does the bending distance. The lateral force can be directly read out from the lateral friction force image; and the corresponding bending distance is read from the topography image. From the geometrical relationship illustrated in Figure 3.2d, when a vertical NW experiences a lateral force f parallel to the scanning direction, the displacement of the NW under the small deflection approximation can be expressed as [49]:

$$EI\frac{d^4x}{dy^4} = (f_0 + f)\delta(y - L) \qquad (3.1)$$

where f_0 is the projected component of the friction force between the tip and the NW in parallel to the tip scanning direction; E and I are the elastic modulus and momentum of inertia of the NW; x is the lateral displacement perpendicular to the NW; y is the height from the fixed end (root) of the NW to the point where the lateral force is applied, which is approximately the tip of the NW ($y = L$), and the contact is assumed to be a point; L is the length of the NW. f_0 is much smaller than the bending force f especially when the scanning speed is low, it thus can be dropped out in Eq. (3.1). The applied lateral force f is expressed as:

$$f = 3EI\frac{x}{L^3} \qquad (3.2)$$

From the Hook's law, the spring constant is $K = f / x$, thus, the elastic modulus can be expressed as a function of the spring constant K, the length of the NW and the momentum of inertia: $E = KL^3/3I$. The ZnO nanowire growing along [0001] usually has a hexagonal cross-section with side length of a (a is the radius of the NW), for which the momentum of inertia is $I = \frac{5\sqrt{3}}{16}\cdot a^4$. From the SEM and TEM images, the aligned ZnO NWs have a uniform diameter of 40 nm (Figure 3.1d) and heights varying from 200 to 800 nm (Figure 3.1b). The elastic modulus is given by:

$$E = \frac{16L^3K}{15\sqrt{3}\cdot a^4} \tag{3.3}$$

From the topography image (Figure 3a), the bright spots with tails are from the NWs, and the tails are due to the deflection of the NWs along the scanning direction of the tip. At the same points in the corresponding lateral force image (Figure 3.3b), there are also spots. To ensure that the center of the conical tip touches the center of the NW as assumed in theoretical calculation, both curves were read from the center of the NW as indicated in the images by dashed lines.

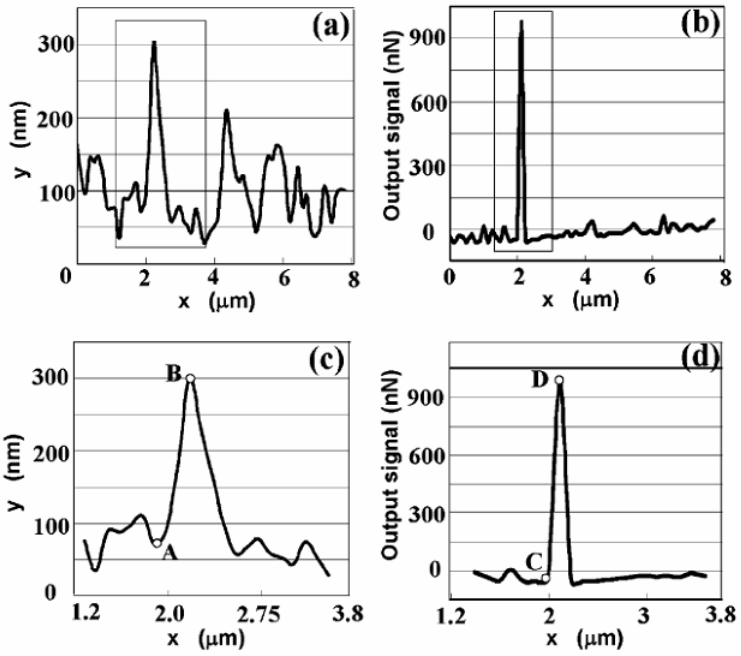

Figure 3.4 (a, b) Line profiles along the dashed lines in Fig. 3.3(a, b) showing the curves of scanner-retracting-distance verses the nanowire-lateral-displacement and the lateral-force verses the lateral-displacement, respectively. (c, d) Enlarged portions of the areas enclosed by rectangles in (a, b), respectively. The set point of the AFM was 0.15 V, while the photo detector output was ~ 6 V at the maximum lateral force.

Taking a line scan across the middle point of a spot in the topological image, a curve for the scanner retracting distance verses the NW lateral displacement is obtained, as shown in Figure 3.4a. A suddenly change in the profile occurs when the tip scans over the NW; the relatively flat part is when the tip scans on the substrate where has no NWs. Taking a scanning profile at the corresponding line in the lateral force image (as indicated in Figure 3.3b), the maximal lateral force for bending the NW is measured. A suddenly change in the curve occurs when the tip meets the NW and the friction force increases rapidly. Figures 3.4c, 3.4d are the enlarged portions of the curves enclosed by rectangles in Figures 3.4a and 3.4b, respectively. As in Figure 3.4c, the scanner retracting distance and the corresponding lateral displacement are the differences in y and x coordinates, respectively, between points A and B. In the corresponding lateral force curve in Figure 3.4d, the difference in heights between points C and D is the maximum bending force of the NW.

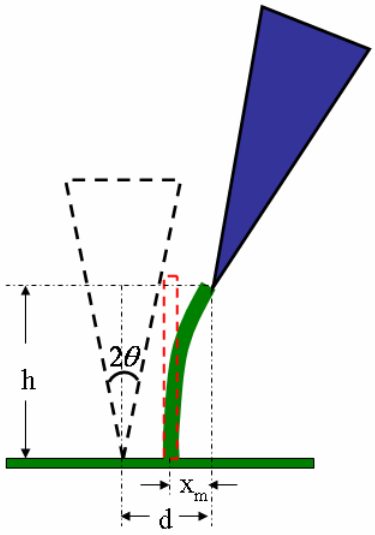

Figure 3.5 Tip-nanowire geometry for calculating the length/height of the nanowire.

The length of the nanowire can be derived from the AFM image, as demonstrated in Figure 3.5. When the tip meets a NW, the scanner/cantilever retracts and at the same time the tip is deflected. From the point starting at which the scanner begins to retract to the largest retracting position, the vertical and lateral displacements are represented by *h* and *d*, respectively, which are measured from the topological image (Figure 3.4a). So the length of a NW is given by $L \approx \sqrt{h^2 + x_m^{\ 2}}$, and the bending displacement of the NW is given by $x_m = d - h\tan\theta$, where 2θ is the apex angle of the AFM tip ($2\theta = 20^o$). From the same position in the lateral force image, we can get the lateral force f_m that caused the maximal NW bending. Combining the measured x_m and f_m from the two line profiles, the spring constant $K = f_m / x_m$ is obtained.

Table 3.1: Measured elastic modulus of aligned ZnO nanowires

Nanowire	Length (μm)	Elastic modulus (GPa)
1	0. 277	20
2	0. 281	22
3	0. 452	20
4	0. 211	36
5	0. 301	42
6	0. 640	36
7	0. 683	47
8	0. 209	35
9	0. 168	15
10	0. 209	35
11	0. 194	22
12	0. 285	28
13	0. 631	21
14	0. 328	31
15	0. 641	20

The elastic modulus of several well alignment ZnO NWs is presented in Table I. The lengths of the nanowires vary from 167.9 to 683.4 nm, the corresponding elastic

modulus varies from 15 to 47 GPa. It appears that the longer nanowire gives a higher modulus. This is likely due to the larger degree of bending of the nanowire, so that the approximations made in the calculation are deviated slightly from practical cases. The averaged elastic modulus of ZnO NW is 29 GPa. This is consistent with the results measured by in-situ TEM.[50]

From Eq. (3), the estimated error in E measurement is:

$$\Delta E/E = 3|\Delta L/L| + 4|\Delta a/a| + |\Delta f/f| + |\Delta x/x| \quad (4).$$

For typical values of ΔL = 10 nm, L =*300 nm,* Δa = 0.5 nm, a = 22.5 nm, $\Delta f/f$ = 3% and $\Delta x/x$ = 3%, Eq. (4) yields $\Delta E/E$ =26%, which gives E = 29 ± 8 GPa. The spread of data in Table I cannot be totally attributed to experimental error because the elastic modulus may depend on the size and length of the NWs. It must be pointed out that the variation in diameter as presented in Fig. 1d is one of the major errors in this type of measurement because the size of the nanowire cannot be accurately measured by AFM without destructing the sample.

This method is a general method for measuring the elastic modulus of individual nanowires aligned on a solid substrate using AFM. The technique has two advantages. One, it is feasible to measure the elastic modulus of an as-grown nanowire without destructing or manipulating the sample. Secondly, the measurements are carried out individually, systematically and almost simultaneously for all of the nanowires aligned in the scanning range of the AFM tip, whose lengths can be different. The topological image and the lateral force image simultaneously capture the geometrical profile and mechanical properties of all the nanowires in the area. An analysis of the images gives the elastic modulus of individual nanowires. The disadvantage of the technique is its inaccuracy in evaluating the size of individual nanowires without destructing the sample. For the ZnO nanowires grown on sapphire surfaces with an average diameter of 45 nm, the elastic modulus is measured to be 29 ± 8 GPa. This technique can be applied to one-dimensional nanostructures of any materials as long as they are aligned on a solid substrate and their density is relatively low

and/or heights are relatively short. In the following sections, the measurement by this method for mechanical property of some aligned one-dimensional nanostructures will be performed.

3.2 Application of The Measurement Based on AFM

3.2.1 Mechanical Property of RuO_2 and RuO_2/TiO_2 Core/Shell Nanowires

3.2.1.1 Introduction of the RuO_2 and RuO_2/TiO_2 Core/Shell Nanowires

Figure 1a shows a scanning electron microscopy (SEM) image of RuO_2 NWs synthesized by the reactive sputtering approach at a synthesis temperature of 450 °C for 3 h, and indicates a high density of uniform RuO_2 NWs more than several micrometers long. In addition, most of the RuO_2 NWs have a square cross section, as shown in the inset of Figure 3.6a.

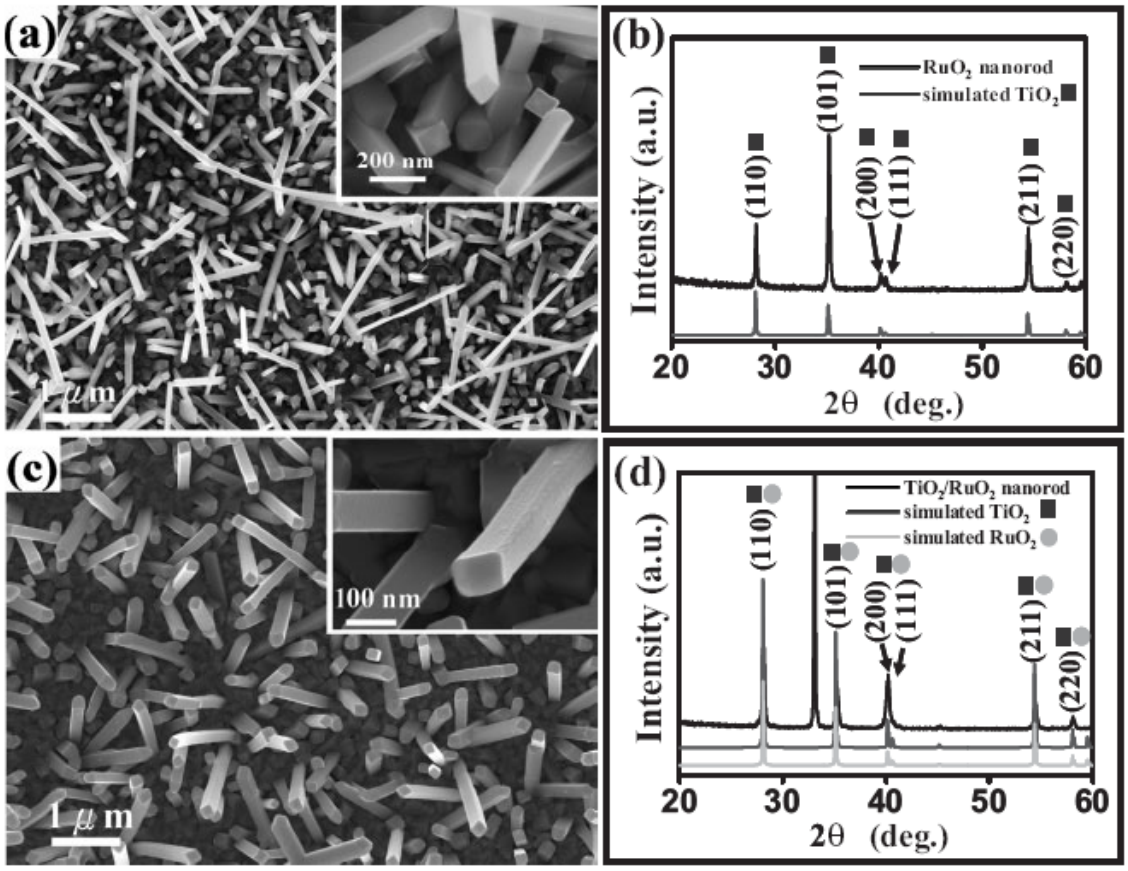

Figure 3.6 a) SEM image of RuO2 NWs synthesized by reactive sputtering at 450 °C for 3 h. The inset shows a magnified SEM image of RuO_2 NWs. b) XRD spectrum of the RuO_2 NWs. The marked spectrum shows the simulated result. c) SEM image of the RuO_2/TiO_2 core/shell structure. The inset shows the corresponding magnified SEM image. d) XRD spectrum of the RuO_2/TiO_2 core/shell structure. The marked spectra represent the simulated results.

The corresponding X-ray diffraction (XRD) spectrum, shown in Figure 3.6b, confirms that the phase of the NWs is rutile-structured RuO_2 with lattice-constant values of a = 0.45 nm and c = 0.31 nm. After deposition of a thin TiO_2 layer via reactive sputtering deposition, the morphology of these NWs remains unchanged, but the sizes increase, as shown in Figure 3.6c. The corresponding XRD spectrum of the NWs is shown in Figure 3.6d. It is hard to distinguish if the individual peaks originate from either RuO_2 or TiO_2 owing to the fact that the lattice mismatch between RuO_2 and TiO_2 is less than 5%.

3.2.1.2 The Measurement of the RuO_2 and RuO_2/TiO_2 Core/Shell Nanowires

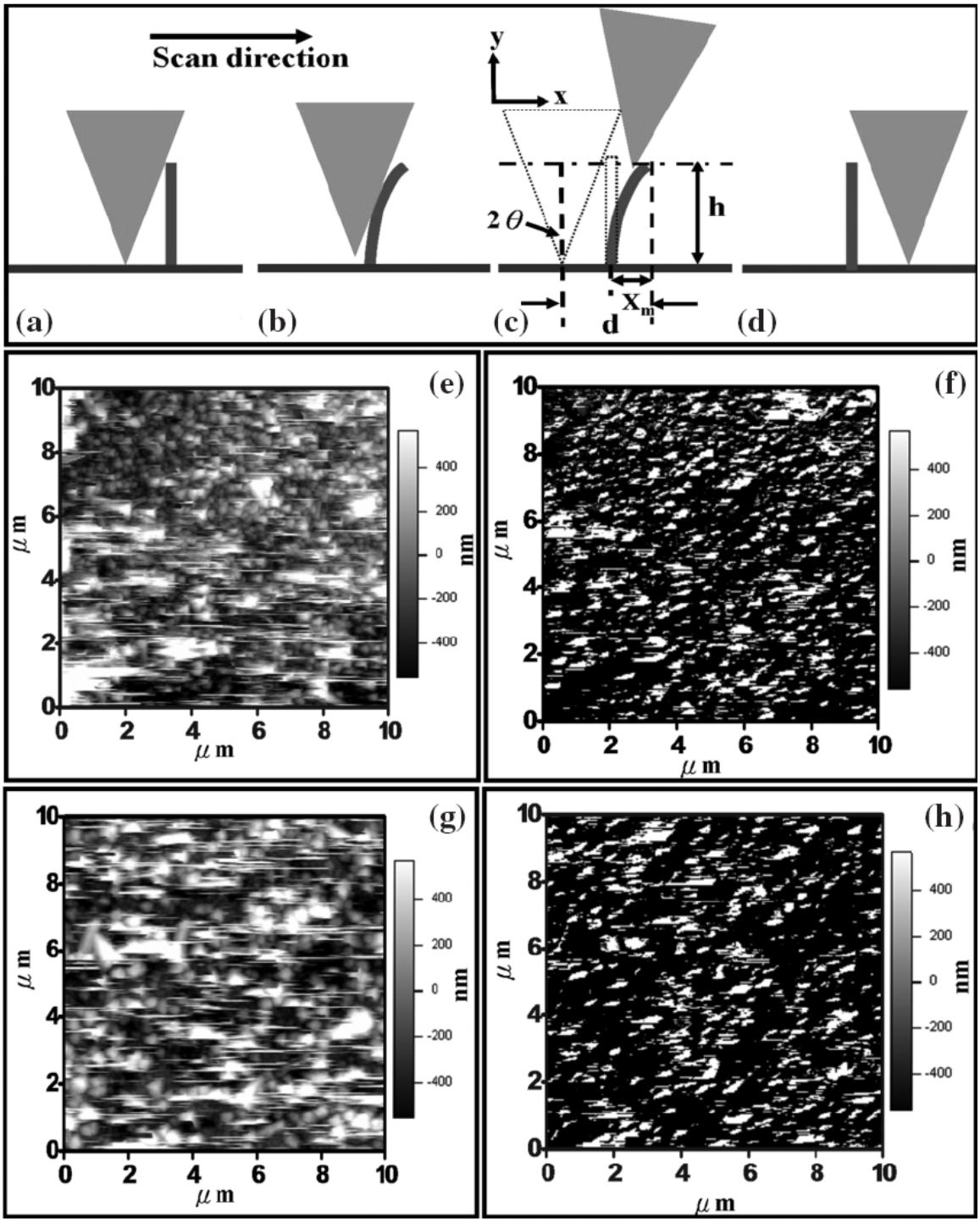

Figure 3.7 a–d) Schematic illustration of AFM tip scanning across a NW. e,f) The topography and lateral-force images of the RuO_2 NWs, respectively. g,h) The topography and lateral-force images of RuO_2/TiO_2 core/shell structure, respectively.

By using an atomic force microscopy (AFM) instrument in contact mode, the elastic

modulus of the NWs was measured without destroying the sample by using a technique developed by Song et al. In the present study, a tetrahedral Si-tip was used as cantilever with a calibrated normal spring of 1.76 Nm^{-1} (AC240TS, Asylum Research), and the lateral spring constant (*K*L) can be calculated by *K*L=*W*2*K*n/*T*2, where *W*, *T*, and *K*n represent the width and thickness of the cantilever, and the normal force spring constant, respectively. The set point (constant normal force) and scanning speed are maintained at 100 nN and 7 $\mu msec^{-1}$. The overall behavior of the NWs in contact-mode scanning is schematically illustrated in Figure 3.7a–d. Both the topography image (the signal from the feedback of scanner) and the lateral-force image were recorded simultaneously, and are shown in Figure 3.7e and f for RuO_2 NWs and in Figure 3.7g and h for the RuO_2/TiO_2 core/shell structure. The scanning area was set as 10 × 10 μm. The bright tails found in the lateral-force images (Fig. 3.7f and g) are a result of the deflection of the nanowires along the scanning direction, as pushed by the tip. As a result, the length of the NWs and the elastic modulus for each individual RuO2NWcan be estimated as ca. 1.669–3.205 μm and ca. 113–390 GPa, respectively, by taking the average length and radius of the NWs presented in Table 3.2. The average elastic modulus is about 250 GPa, which is consistent with the bulk value of 249–313 GPa[51]. The RuO_2 NWs have a higher elastic modulus than other NWs, for example, SiC (610–660 GPa),[15] ZnO (29–230 GPa)[52,53], GaN (227- 305 GPa)[54], and Si (93–250 GPa)[55],

Table 3.2. The elastic modulus of RuO_2 and the RuO_2/TiO_2 core/shell structure measured by AFM.

RuO_2 NWs	Length(μm)	Elastic Modulus(GPa)	RuO_2-TiO_2 coaxial NWs	Length(μm)	Elastic Modulus(GPa)
1	2.068	169	1	1.936	177
2	20513	390	2	2.088	250

3	2.593	143	3	1.721	221
4	2.268	330	4	1.895	90
5	2.319	304	5	2.086	446
6	2.305	249	6	2.055	91
7	3.271	233	7	1.661	123
8	1.697	113	8	1.374	91
9	3.205	161	9	1.398	130
10	1.987	416	10	1.825	424
11	2.077	209	11	2.306	196
12	1.669	261	12	1.878	90

For the RuO_2/TiO_2 core/shell structure, the elastic modulus is in the range 90–424 GPa, as presented in Table 3.2. The average elastic modulus is found to be about 194 GPa. However, in comparison with the average elastic modulus of the RuO2 NWs, the elastic modulus of the RuO_2/TiO_2 core/shell structure is found to have decreased by ca. 22 %. The decrease of the elastic modulus can be accounted for by the composite of RuO_2 and TiO_2. Based on flexural rigidity as theory for transverse deflection, *EI* can be defined as the effective flexural rigidity of the core/shell structure, for which *E* represents the effective elastic modulus of that core/shell structure. Hence, an effective elastic modulus can be given, without considering shear deformation, as[16] $EI = E_c I_c + E_s I_s$ (1) where E_c and E_s represent the elastic moduli of the core and the shell, respectively, and the variables $I_c = a^4/12$ and $I_s = (b^4 - a^4)/12$ are the cross-sectional moments of inertia for the core and the shell, respectively. The values *a* and *b* represent the diameters of the RuO_2 core and the total RuO_2/TiO_2 core/shell structure, respectively, using a cylindrical geometrical approximation. By taking the average bulk elastic modulus for both the RuO2 core (E_c = 281 GPa) and the TiO_2 shell (E_s = 200.5 GPa), along with average values for *a* and *b* of ca. 105 nm and ca. 165 nm, respectively, the effective modulus of the core/shell

structure with a TiO_2-shell thickness of ca. 25 nm is found to be ca. 208 GPa, in reasonable agreement with the measured result.

3.2.2 Measurement on Ni-doped Metallic $TaSi_2$ Nanowires

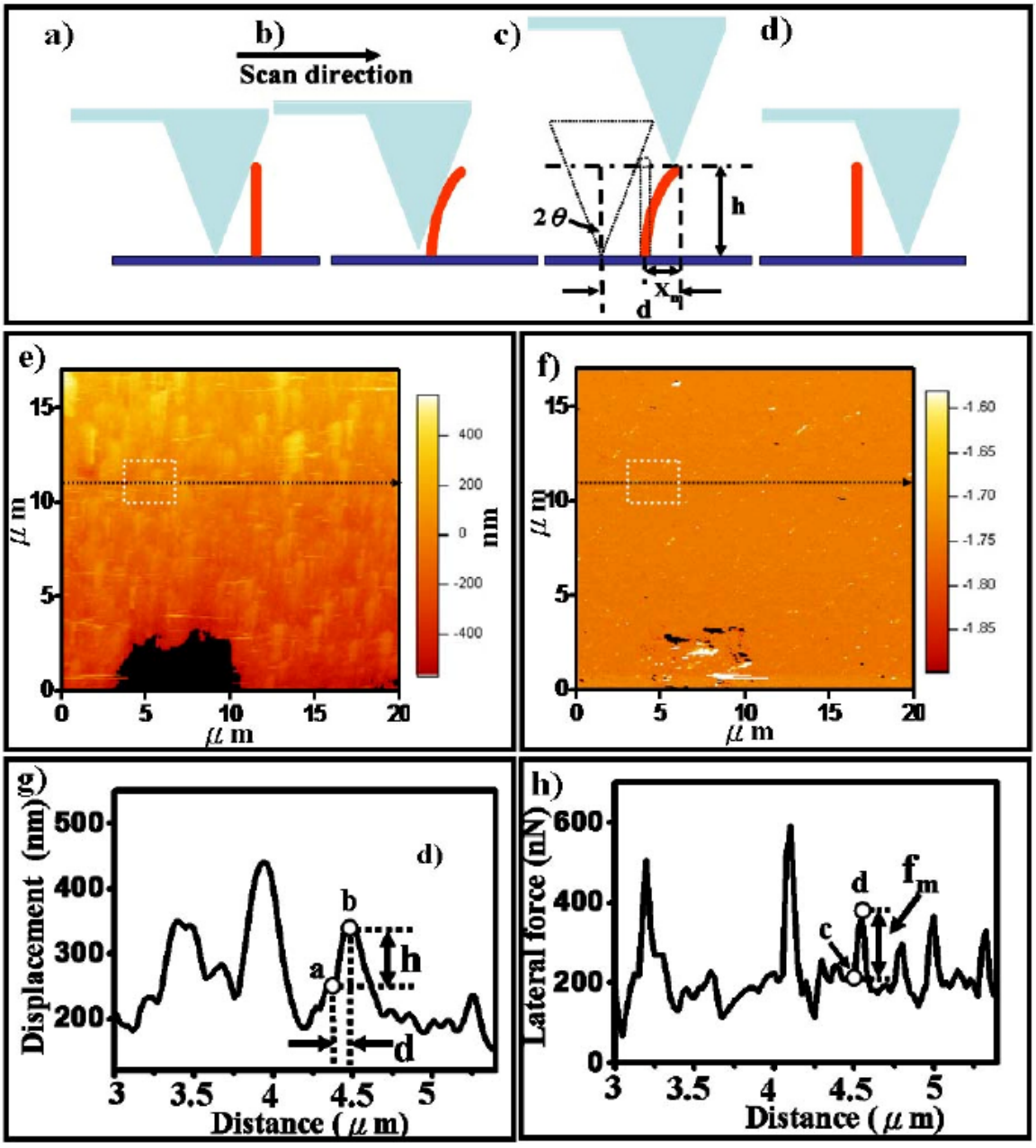

Figure 3.8 (a)–(d) The motion of a cantilever scan over the nanowires in an AFM in contact mode. (e) The topography image and (f) the lateral force image taken

simultaneously from the AFM in contact mode. (g) Line profile of bending displacement as a function of scanning distance and (h) line profile of the lateral force as a function of the scanning distance recorded from the dashed line along the figures (e) and (f). *h, d* and *fm* represent the largest bending height, scanning distance for the Si tip across the nanowires, and a constant lateral force when the scanner touches the nanowire.

The same measurement method was applied on aligned Ni-doped metallic $TaSi_2$ nanowires. A rectangular Si cantilever with a tetrahedral Si tip was used in present study, which had a calibrated normal spring constant of 1.8 Nm−1 (AC240TS, Asylum Research). In addition, the lateral spring constant can be calculated from $KL = W2Kn/T2$, where W and T represent the width and thickness of the cantilever and Kn means the normal force spring constant. The set point (constant normal force) and scanning speed are maintained at 100 nN and 7 μm s−1, respectively. The overall behaviours of scanning over the nanowires in contactmode are schematically illustrated in figures 3.8 (a)–(d).

The Si tip was in contact with the surface of the sample at a constant force (figure 3.8(a)). The motion of the scanning tip over the nanowires can be well controlled by surface morphology and lateral force. A small lateral force recorded by a photodetector was detected when the Si tip meets the nanowire (figure 3.8(b)). This lateral force was drastically increased as the Si tip consecutively scanned toward the nanowire so that the nanowire is elastically bent from its equilibrium position. At the largest bending position, the Si tip reaches the highest height and maximum lateral force (figure 3.8(c)). After the Si tip scan across the largest bending position, the nanowire was released, resulting in a sudden drop in the lateral force (figure 3.8(d)). Therefore, both the topography image (signal from the feedback of scanner) and lateral force image can be record simultaneously, as shown in figures 3.8(e) and (f) where the scanning area was set at 20 μm × 20 μm. Note that the bright tail in figure 3.8(e) results from the deflection along the scanning direction. The identical position in the lateral force image corresponding to the

topography also shows a bright spot. In order to make sure that the centre of the tetrahedron can accuratelymeet the centre of the nanowires for theoretical calculation, the dashed line cross both same positions are made so that the displacement and lateral force as a function of the scanning distances can be found. Examples are shown in figures 3.8(g) and (h), which are derived from the dashed rectangle area of figures 3.8(e) and (f), respectively. From the displacement as a function of the scanning distance, as shown in figure 3.8(g), the *d* value in the *x* axis between points a and b means that the Si tip starts to touch the nanowires at the largest bending equilibrium position (figure 3.8(c)). The drop found behind the point b represents the Si tip crossing the nanowires. *h* represents the maximum bending height from the substrate. Subsequently, the elastic modulus for individual Ni-doped TaSi2 nanowires can be estimated by taking the length of the nanowire, the average radius of the nanowire, and the lateral force spring constant, as given in table 3.3.

Table 3.3. Length and elastic modulus of individual Ni-doped $TaSi_2$ nanowires measured with an AFM.

Nanowire	Length (μm)	Elastic modulus (GPa)
1	0.2336	343
2	0.2347	344
3	0.1355	172
4	0.3137	485
5	0.3352	390
6	0.2745	399
7	0.1456	258
8	0.3096	304
9	0.2443	207
10	0.1983	147
11	0.2974	396
12	0.1391	170
13	0.1449	312

The length of the nanowires and the corresponding elastic modulus ranged from 0.1355 to 0.3353 μm and 170 to 485 GPa, respectively. The average elastic modulus is approximately 302 GPa, which is consistent with the value of 323 GPa for thin films (polycrystalline form)[56]. Note that the elastic modulus in the present study is increased as

the length is increased. Similar phenomena are found for ZnO, and Ag[57] nanowires as well as carbon nanotubes (CNTs) while some nanowires such as Cr [58] and Si [59] exhibit the opposite tendency. In addition, SiC [60] and Au [61] nanowires have no dependence on diameter. The details are still unknown and need to be investigated in the future.

Comparing the elastic modulus with those of other nanowires by the electromechanical resonance method and atomic force microscopy method, such as carbon nanotube (1.28–0.6 TPa) [60], SiC (610–660 GPa) [60], ZnO (29–230 GPa) [52,53], GaN (227–305 GPa) [62], and Si nanowires (93–250 GPa) [63,64], the metallic Ni-doped TaSi2 NWs have good mechanical properties,

CHAPTER 4

NANO PIEZOTRONICS' BASIS NANOGENERATOR

Developing novel technologies for wireless nanodevices and nanosystems are of critical importance for in-situ, real-time and implantable biosensing, biomedical monitoring and biodetection. An implanted wireless biosensor requires a power source, which may be provided directly or indirectly by charging of a battery. It is highly desired for wireless devices and even required for implanted biomedical devices to be self-powered without using battery. Therefore, it is essential to explore innovative nanotechnologies for converting mechanical energy (such as body movement, muscle stretching), vibration energy (such as acoustic/ultrasonic wave), and hydraulic energy (such as body fluid and blood flow) into electric energy that will be used to power nanodevices without using battery. It also has a huge impact to miniaturizing the size of the integrated nanosystems by reducing the size of the power generator and improving its efficiency and power density

Nanowires (NWs) and nanobelts (NBs) of inorganic materials are the forefront in today's nanotechnology research. Among the known one-dimensional nanomaterials, zinc oxide (ZnO) has three key advantages. First, it exhibits both semiconducting and piezoelectric properties, providing a unique material for building electro-mechanical coupled sensors and transducers. Secondly, ZnO is relatively bio-safe and biocompatible, and it can be used for biomedical applications with little toxicity. Finally, ZnO exhibits the most diverse and abundant configurations of nanostructures know up to today, such as nanowires[65], nanobelts[66], nanosprings[67], nanorings[68], nanobows[69], nanohelices[70] and more. Although there are numerous work have been done for demonstrating novel nanodevices and applications based on nanowires and nanobelts, but little work has done to address the power needs for these nanosystems, especially self-powering, wireless operation and miniaturization of the entire integrated system. In this paper, we

demonstrate for the first time a novel approach of converting mechanical energy into electric power using aligned ZnO nanowires. The operation mechanism of the power generator relies on the coupling of piezoelectric and semiconducting properties of ZnO as well as the formation of Schottky barrier between the metal and ZnO contacts. The nano-generator shown here could be the foundation for self-powering nanodevices for optoelectronics[71], biosensors[72], resonators[73] and more. It also offers the possibility of miniaturizing the size of the entire integrated nanosystem.

4.1 First Nanogenerator in the World

4.1.1 Nanogenerator Based on ZnO Nanowire Arrays

The first Nanogenerator in the world is based on aligned ZnO nanowires grown on c-plane oriented α-Al_2O_3 substrate using gold particles as catalyst by the vapor-liquid-solid (VSS) process[74].

4.1.1.1 Samples f

The sample used in this experiment is aligned ZnO nanowires grown on c-plane oriented Al_2O_3 substrate using gold particles as catalyst by the vapor-liquid-solid (VSS) process. Due to an epitaxial relationship of ZnO and Al_2O_3, a thin layer of continuous ZnO film is formed at the substrate surface, which served as a large electrode connecting the NWs with a metal electrode for transport measurement.

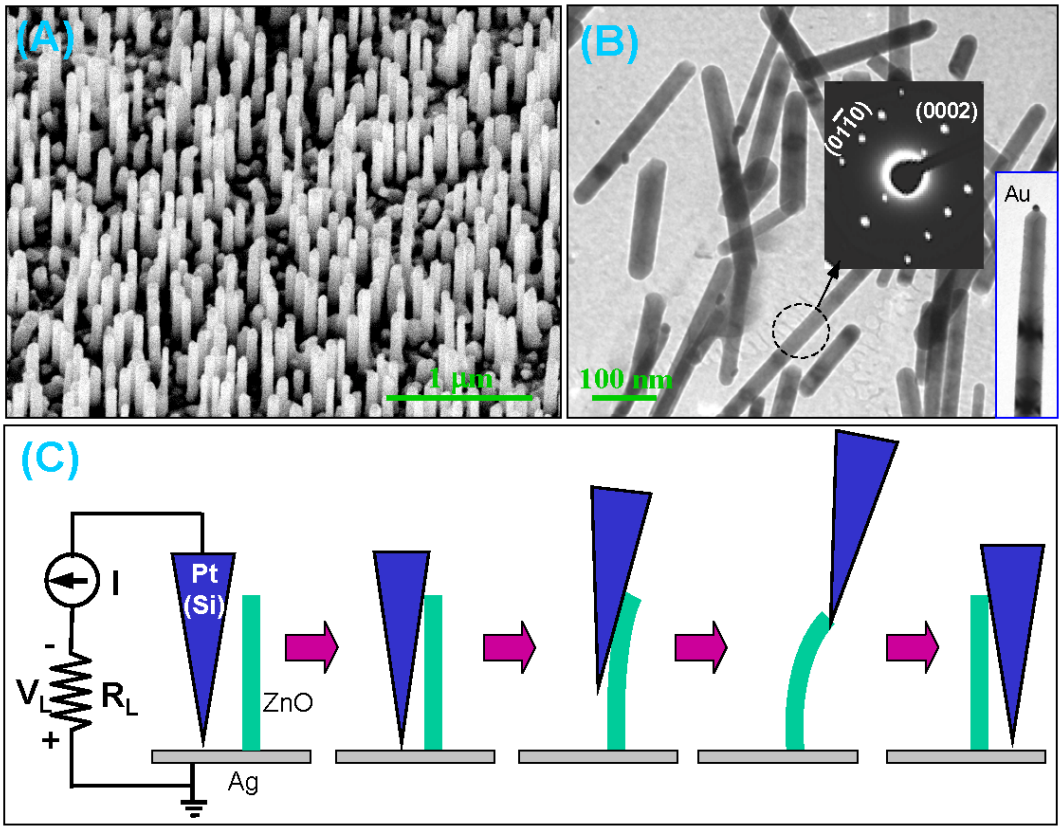

Figure 4.1 Experimental design for converting nano-scale mechanical energy into electric energy by a vertical piezoelectric ZnO nanowire. (**A**) SEM images of aligned ZnO nanowires grown on -Al_2O_3 substrate. (**B**) Transmission electron microscopy (TEM) images of ZnO NWs, showing the typical structure of the NW without a gold particle or with a small gold particle at the tip. Each NW is a single crystal and has uniform shape. The inset is an electron diffraction pattern from a NW. Most of the NWs have no gold tip. An NW with a gold tip is inserted. (**C**) Experimental set up and procedures for generating electricity by deforming a piezoelectric NW using a conductive AFM tip. The root of the NW is grounded, and an external load of R_L = 500 M is applied, which is much larger than the inner resistance R_I of the NW. The AFM scans across the NW arrays in contact mode.

Figure 4.1A shows a scanning electron microscopy (SEM) image of the aligned ZnO nanowires. The nanowires grows along [0001] and has side surfaces of $\{01\bar{1}0\}$ (Fig. 4.1B). Most of the gold particles at the tips of the NWs either have been evaporated during the growth or fallen off during AFM tip scanning [See Fig. 4.2]. For most of the NWs, the growth front is either without gold particle or has a small hemispherical gold particle that covers only a fraction of the top (see the inset image in Fig. 4.1B). For the purpose of our measurements, we have grown NW arrays that have relatively less density and shorter length (0.2 – 0.5 m), so that the AFM tip can exclusively reach one NW without touching another.

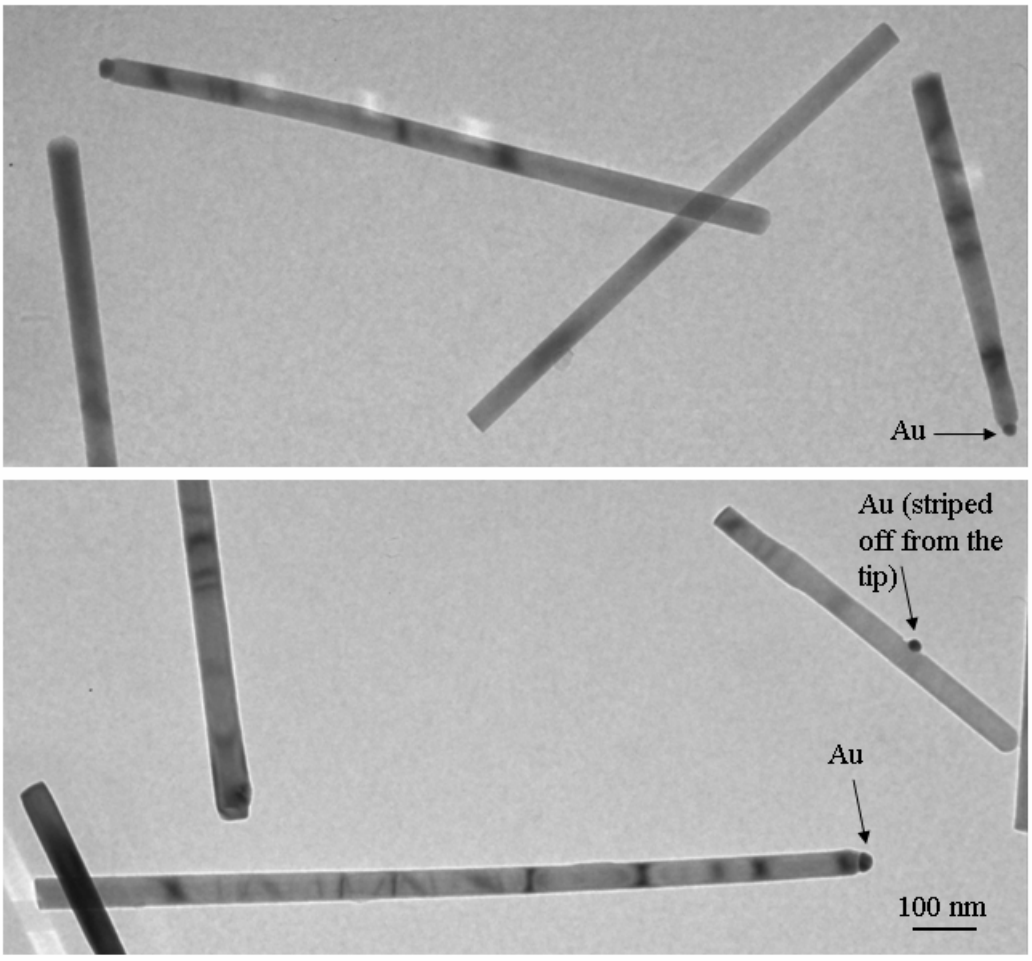

Figure 4.2 TEM images of ZnO nanowires showing no gold caps or with small gold caps at the growth fronts. Note the hespherical shape of the gold particles at the tips

4.1.1.2 Conductive AFM measurement of Nanogenerator

The measurements were performed by AFM (Molecular Force Probe MFP-3D™ from Asylum Research) using a Si tip coated with Pt film, which has a cone angle of 70^{o}. The rectangular cantilever had a calibrated normal spring constant of 0.76 N/m. The experimental procedure is illustrated in Figure 4.1C. In the AFM contact mode, a constant normal force of 5 nN is kept between the tip and sample surface. The tip scans over the top of the ZnO NW and the tip's height is adjusted according to the surface morphology and local contacting force. With considering the size of the NW, the thermal vibration of the NW at room temperature is negligible. For the electric contact at the bottom of the nanowires, silver paste was applied to connect the (large) ZnO film on the substrate surface with the measurement circuit. The output voltage across an outside load of resistance R_L = 500 MΩ was continuously monitored as the tip scans over the nanowires (note the defined polarity of the voltage signal). No external voltage was applied in any stage of the experiment.

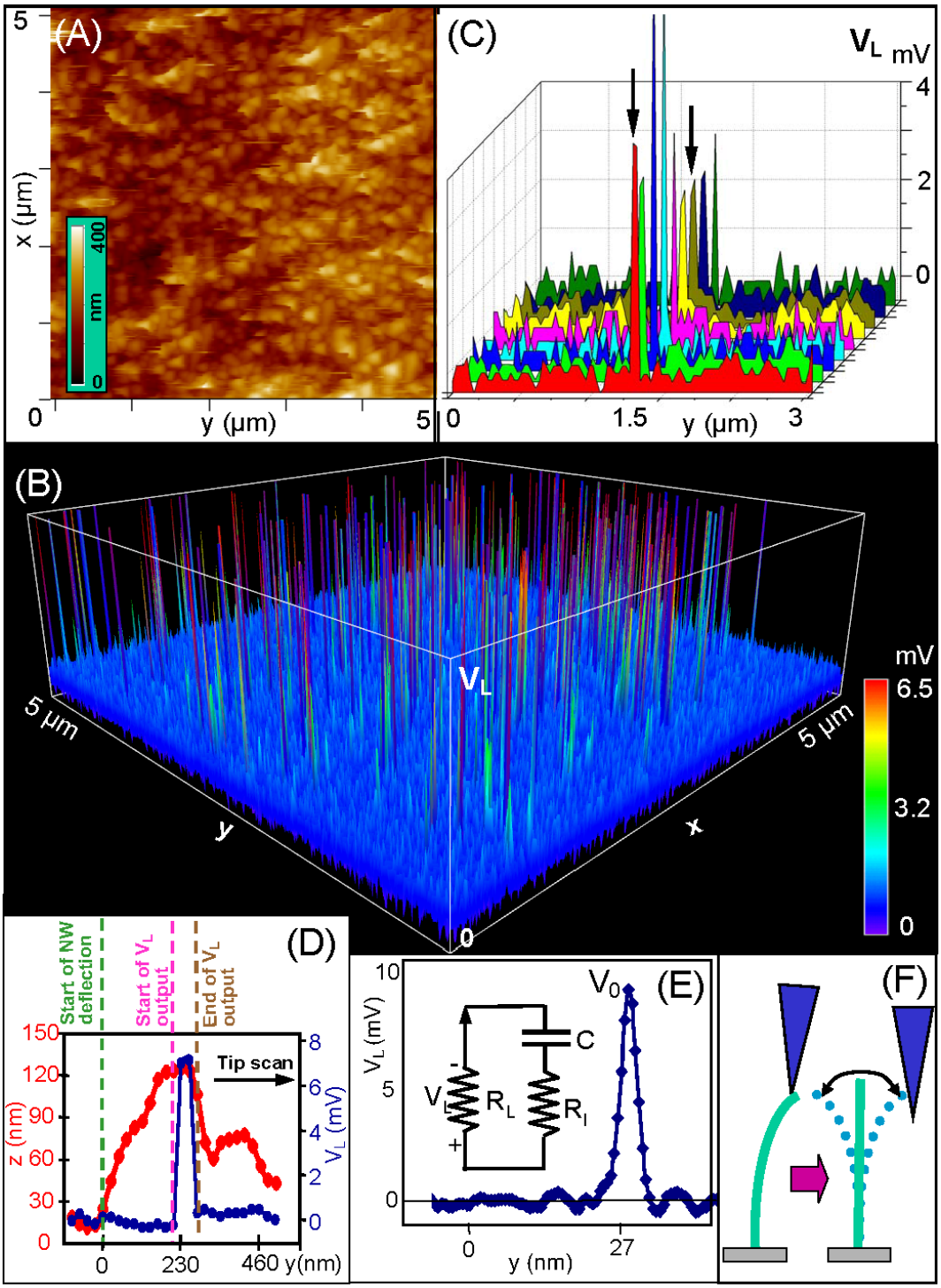

Figure 4.3 Electro-mechanical coupled discharging process of aligned piezoelectric ZnO NWs observed in contact mode. (**A**) Topography image and (**B**) corresponding output voltage image of the NW arrays. The discharging process is so quick that each discharge event is characterized by only a couple of data points. This gives a difficulty of displaying

the data by rainbow color (see Fig. 4.4). (**C**) A series of line profiles of the voltage output signal when the AFM tip scanned across a vertical NW at a time interval of 1 min. The data shows the registration of the electric signal with the location of the NW and the reproducibility of the event over an extended period of time. In (A-C), the scanning speed of the tip was 12.081 μm/s, and the time spent to acquire and output one scan point was 2 ms. (**D**) Line profiles from the topography (red) and output voltage (blue) images across a NW. The peak of the voltage output corresponds approximately to the maximum deflection of the NW, indicating the discharge occurs when the tip is in contact with the compressed side of the nanowire. When the tip touches the NW, piezoelectric charges start to accumulate, but no discharging. The discharge occurs when the deflection reaches close to the maximum y_m. Note the lateral deflection y includes the shape and contact geometry of the tip, which have to be subtracted to derive the true deflection of the NW. (**E**) Line profile of the voltage output signal when the AFM tip scanned across a vertical NW at 12.394 m/s, and the time spent to acquire and output one scan point was 0.05 ms achieved at the maximum scan frequency of the AFM. The inset is an equivalent circuit of the measurement to be used for simulating the discharging process. (**F**) The resonance vibration of a NW after being released by the AFM tip, showing that the stored elastic energy is transferred mainly into vibration energy after creating the piezoelectric discharge event.

Experimentally, both the topography (feed back signal from the scanner) (Fig. 4.3A) and the corresponding output voltage (V_L) images across the load (Fig. 4.3B) were recorded simultaneously when the AFM tip was scanned over the aligned NW arrays. In contact mode, as the tip scans over the vertically aligned NWs, the NWs are bent consecutively. The bending distance is directly recorded in the topography image, from which the maximum bending deflection distance and the elastic modulus of the NW as well as the density of NWs that have been scanned by the tip are directly derived. In the

output voltage image, many sharp output voltage peaks (like discharge peaks) have been observed, which are typically about 4-50 times higher than the noise level. The peak is rather sharp and narrow, and sometime one or two pixels represent one voltage peak due to the limited scanning speed of the AFM tip, so that the color distribution in the plot is not easy to display [See Fig. 4.4]. By reducing the scan range and increase the scan frequency, nice profiles of the discharge peaks are captured [See Fig. 4.5]. Most of the voltage peaks are ~ 6-9 mV in height. The density of NWs contacted by the tip is counted from Fig. 4.3A to be ~ 20/μm^2, and the average density of NWs whose voltage output events had been captured by the tip in Fig. 4.3B is ~ 8/μm^2, about 40% of the NWs contacted.

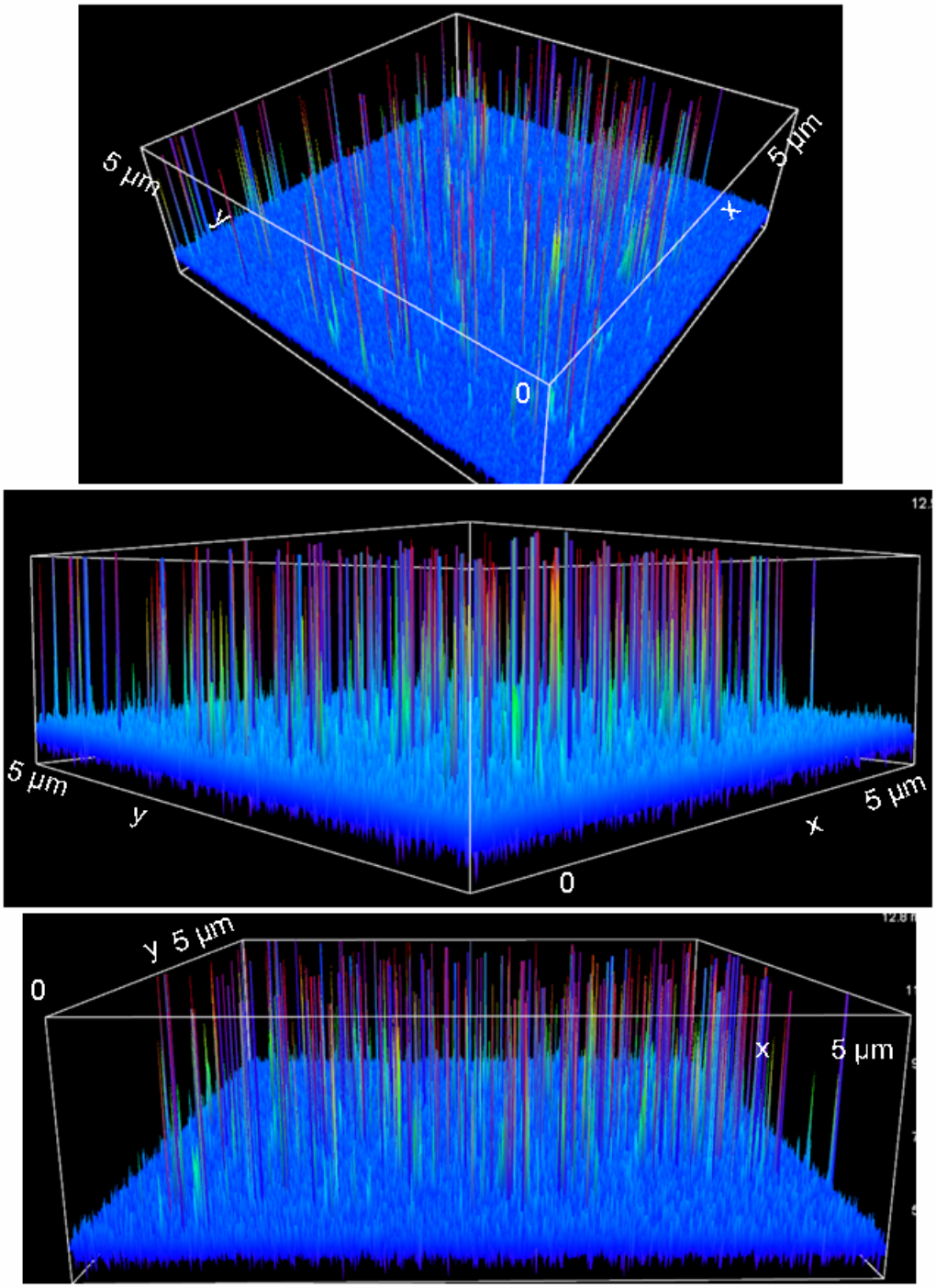

Figure 4.4 Three different perspectives of outputting the data shown in Fig. 4.3B to clearly image the sharp piezoelectric voltage peaks.

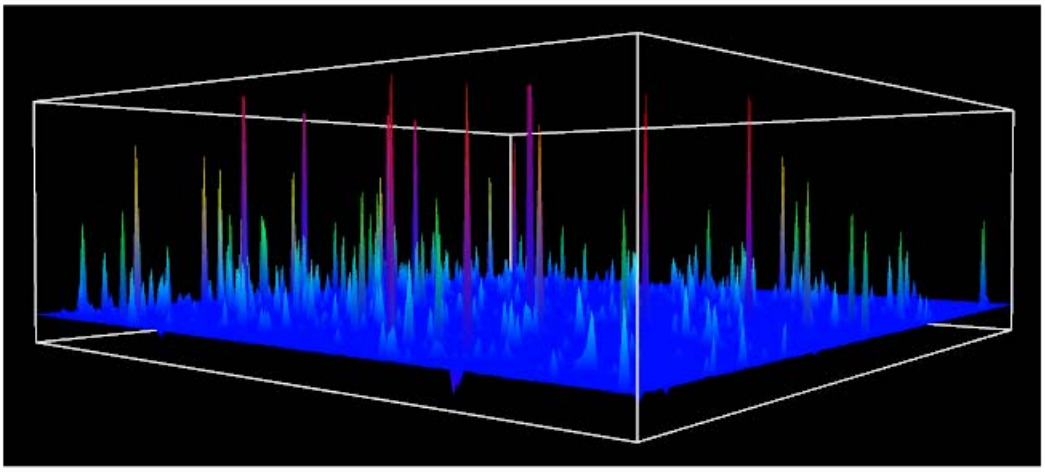

Figure 4.5 Piezoelectic output voltage received at a higher scan frequency at a small scan region, showing the shape of the discharge peaks. The output voltage peak is as high as 20 mV.

The location of the voltage peak is directly registered at the site of the NW. Figure 4.3C shows a time series of the voltage output line profiles across one NW acquired at a time interval of 1 min (Fig. 4.3C). Since the dowel time for each data point (or pixel) is 2 ms, which is longer than the average life time of the voltage peak of ~0.6 ms (see Fig. 4.3D), the peak at which the output voltage reached the maximum was possibly missed by the "slow" scanning tip, so that the voltage output shows a chopped top, as indicated by arrowheads in Fig. 4.3C. A sharp peak can be identified continuously at the location of the NW, and the NW outputs voltage in each scan of the tip. When the tip starts to deflect the NW, no voltage output is observed (Fig. 4.3D). The output voltage is detected when the deflection of the NW reaches almost to its maximum. The output voltage drops to zero when the NW is released by the AFM tip, indicating the piezo-electricity is output towards the end of the AFM scan over the nanowire.

The shape of the discharge peak can be further improved and analyzed by maximizing the tip scanning frequency and reducing the scanning range. Figure 4.3E

gives a line profile of the voltage output when the tip was scanned over a single NW at a scanning velocity of 12.394 μm/s. The FWHM of the voltage peak is estimated to be τ ~ 0.6 ms. The damping behavior of the voltage peak can be qualitatively described using an equivalent circuit, as inserted in Fig. 4.3E.

Before the further discussion of experimental data on nanogenerator based on ZnO nanowire arrays, the following several sections for the principles of the bending ZnO nanowire and equivalent circuit for the experimental set up will be introduced.

4.1.1.3 Equivalent Circuit of Nanogenerator

For Fig. 4.3E, the power generating process of nanogenerator is discharge process of an RC circuit, as show in Figure 4.6 below.

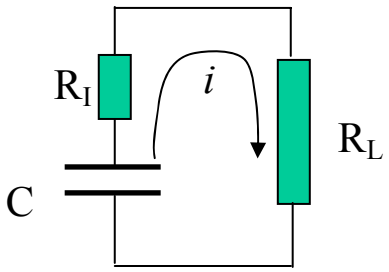

Figure 4.6 Equivalent circuit of the nanogenerator.

The basic function for this circuit could be expressed as

$$\frac{1}{C}\int i \cdot dt + (R_L + R_I) \cdot i = 0 \qquad (4.1)$$

This equation could be rewritten as the differential format:

$$\frac{i}{C} + (R_L + R_I)\frac{di}{dt} = 0 \qquad (4.2)$$

Then integrate the differential equation 4.2, we can get

$$i = I_0 \cdot e^{-\frac{t}{(R_L+R_I)C}} \qquad (4.3)$$

Initial condition: $t = 0$, $i = \frac{V_0}{R_L + R_I}$ plug into 4.3, then

$$i = \frac{V_0}{R + r} \cdot e^{-\frac{t}{(R_L + R_I)C}} \tag{4.4}$$

The decay time constant $\tau = (R_L + R_I)C$

The electric power consumed by the resistor R (the output work):

$$\begin{aligned} \Delta W_{PED} &= \int i^2 R \cdot dt \\ &= \frac{V_0{}^2 R_L}{(R_L + R_I)^2} \int_0^\infty e^{-\frac{2t}{(R_L + R_I)C}} \cdot dt \\ &= \frac{V_0{}^2 R_L C}{2(R_L + R_I)} \end{aligned} \tag{4.5}$$

For $R_I << R_L$

$$\Delta W_{PED} \approx \frac{V^2{}_0 C}{2} \tag{4.6}$$

The simple express of output electrical work of equation 4.6 shows the output work is related with the magnitude of electrical pulse and the capacitance of the circuit. For the output work is approximately lineally proportional to the second power of the magnitude of the electrical pulse, improve the magnitude of the electrical pulse could increase the output electrical work greatly.

4.1.1.4 Bending Theory for Nanogenerator

To better understand the bending induced piezoelectric voltage drop across a nanowire at the front end, the following analytical analysis will be presented.

The following calculation we consider the in-plane banding of a nanowire by an external point force F perpendicular to the nanowire. For a short segment of nanowire, the

local bending can be approximately by a small arc characterized by a small angle θ and local curvature of radius R see figure 4.7 below.

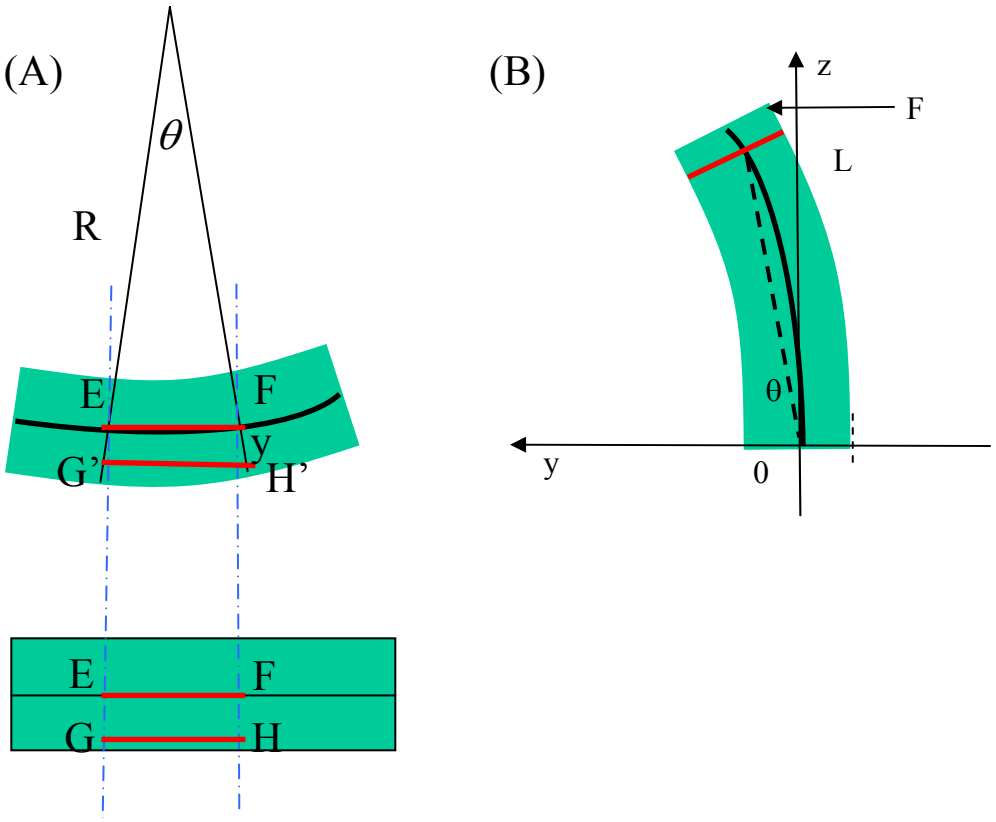

Figure 4.7 (A) A segment of a nanowire for calculating the bending induced piezoelectric potential across the two side surfaces. (B) The definition of coordination system under an external displacement force F.

The local strain is

$$\varepsilon = \frac{H'G' - HG}{HG} = \frac{H'G' - HG}{EF} \approx \frac{(R+y)\theta - R\theta}{R\theta} = \frac{y}{R} \qquad (4.7)$$

Using the stress and strain relationship, we have:

$$\sigma = Y\varepsilon = Y\frac{y}{R} \tag{4.8}$$

where Y is the elastic modulus. The static of the system is the balance of moment. The total moment of the bent nanowire is

$$M = \int y \cdot \sigma \cdot dA$$

By using Eq. (4.8)

$$M = \int \frac{Y}{R} \cdot y^2 \cdot dA = \frac{Y}{R} \cdot \int y^2 \cdot dA = \frac{Y}{R} \cdot I$$

we have $$\frac{M}{I} = \frac{Y}{R} = \frac{\sigma}{y} \tag{4.9}$$

From the geometry shown in Fig. S7(B), we have the following results under small angle approximation:

$$\frac{dy}{dz} = \tan\theta \approx \theta \qquad \text{thus} \qquad \frac{1}{R} = \frac{d\theta}{ds} \approx \frac{d\theta}{dz} = \frac{d}{dz}\left(\frac{dy}{dz}\right) = \frac{d^2y}{dz^2}$$

In combining with Eq. (4.9),

$$\frac{1}{R} = \frac{M}{YI} = \frac{d^2y}{dz^2} \qquad d\theta = \frac{1}{R} \cdot dz = \frac{M}{YI} \cdot dz \tag{4.10}$$

By the principle of balancing of moment: internal moment = external moment

$$M = YI\frac{d^2y}{dz^2} = F\cdot(L-z) \quad \rightarrow \quad \frac{d^2y}{dz^2} = \frac{M}{YI} = \frac{F\cdot(L-z)}{YI} \tag{4.11}$$

where the external force is assumed to act approximately perpendicular to the nanowire at the top and L is the nanowire length. Equation (4.11) determines the bending of the nanowire under the deflection of an external force at the front end.

Now we calculate the potential produced by piezoelectric effect. From the definition of the piezoelectric coefficient (d): $d = \frac{\varepsilon}{E}$, the corresponding electric field along z-axis is

$$E_z = \frac{\varepsilon}{d} = \frac{y}{d\cdot R} \tag{4.12}$$

This is the field that dominates the potential distribution under small bending angle approximation. For simplicity of analytical calculation and to illustrate the physical principle, we consider the potential at the side surface $y = a$ along the entire length of the nanowire:

$$E_z = \frac{a}{d\cdot R}$$

$$V = \int E\cdot ds = \int \frac{a}{d}\cdot\frac{1}{R}\cdot ds = \frac{a}{d}\cdot\int\frac{1}{R}\cdot ds = \frac{a}{d}\cdot\int d\theta$$

Using equation (4.10) and (4.12)

$$V = \frac{a}{d}\int \frac{M}{YI}\cdot dz = \frac{a}{d}\int \frac{F\cdot(L-z)}{YI}\cdot dz = \frac{aF}{dYI}\int_0^L (L-z)\cdot dz = \frac{aFL^2}{2dYI} \qquad (4.13)$$

Together with the relationship between the maximum deflection y_m and the applied force: $F = \frac{3YIy_m}{L^3}$ (see next section), we have the potential induced by piezoelectric effect:

$$V = \frac{3ay_m}{2Ld} \qquad (4.14)$$

4.1.1.5 Deflection of the Nanowire under External Force

We now consider the deflection of the nanowire under an externally applied force F perpendicular to the nanowire. From Equation (4.11) and boundary conditions:

$$y(z=0) = 0\,;\ \frac{dy(z=0)}{dz} = 0\,.$$

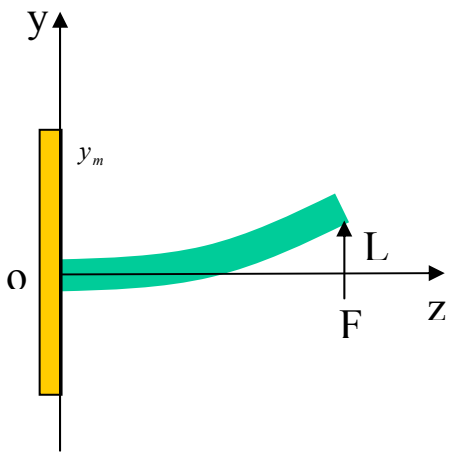

Figure 4.8 Coordinates for analysis of bending nanowire

integrating equation (4.11) gives

$$\frac{dy}{dz} = \frac{F}{YI}(Lz - \frac{1}{2}z^2)$$

and

$$y = \frac{F}{YI}(\frac{1}{2}Lz^2 - \frac{1}{6}z^3)\,\mathrm{z} \qquad (4.15)$$

For $z = L$, $y = y_m$

$$y_m = \frac{FL^3}{3YI} \quad \rightarrow \quad F = \frac{3YIy_m}{L^3} \qquad (4.16)$$

The mechanical work done by the external force for bending of the nanowire:

$$W = \int \vec{F} \cdot d\vec{l} = \int_0^{y_m} F(y)dy = \int_0^{y_m} \frac{3YI}{L^3} \cdot y \cdot dy = \frac{3YI}{2L^3} y_m^2 \qquad (4.17)$$

4.1.1.6 The Elastic Deformation Energy of the Nanowire

To calculate the energy loss after a single cycle of vibration, we assume that the amplitude of the nanowire resonance decays with time as described by:

$$y_m = y_{mo} e^{-t/t_0} \qquad (4.18)$$

where y_{mo} is the maximum deflection pushed by the AFM tip, and t_o is the decay constant of the vibration amplitude. Therefore, the elastic energy at a subsequent vibration is

$$W_{ELD} = \frac{3YI}{2L^3} y_m^2 = \frac{3YI}{2L^3} y_{m0}^2 \cdot e^{-2t/t_o} \qquad (4.19)$$

The energy dissipated after one cycle of vibration is

$$\Delta W_{ELD} = \frac{3YI}{t_0 L^3} y_{m0}^2 \cdot e^{-2t/t_o} \cdot \Delta t \qquad (4.20)$$

First the cycle: $t = 0$ and $\Delta t = \frac{1}{f}$:

$$\Delta W_{ELD} = \frac{3YI}{t_0 L^3} y_{m0}^2 \cdot \frac{1}{f} \qquad (4.21)$$

Under the first order approximation[75], the life time of the resonance t_o is related to the quality factor Q and resonance frequency f by

$$t_0 \approx \frac{\sqrt{3}Q}{\pi f}$$

Therefore

$$\Delta W_{ELD} = \frac{3YI}{2L^3} y_{m0}^2 \cdot \frac{2\pi}{Q\sqrt{3}} = W_{\max} \cdot \frac{2\pi}{Q\sqrt{3}} \qquad (4.22)$$

For ZnO nanobelts in a vacuum of 10^{-7} torr, $Q = 600$ [76], the efficiency of energy transform by the NW is $\Delta W_{PED} / \Delta W_{ELD}$.

4.1.1.7 Analysis and Discussion

For A piezoelectric material can be approximately characterized by a capacitor and a resistor. The capacitor represents the piezoelectric charges accumulated in the volume, and the resistor represents its inner resistance. The NW is approximated as a

capacitor C and an inner resistor R_I. The lifetime of the output voltage peak across the load V_L (note the polarity of the voltage) is $\tau = (R_L+R_I)C$. For the experiment we have designed, the resistance of the NW R_I is negligible in comparison to R_L. From our recent measurements of ZnO nanowires, the resistivity is from 10^{-2} -cm to ~10 -cm[77] depending on the contacts at the electrodes and the concentration of oxygen vacancies. For a NW of length 0.2 μm and diameter 40 nm, the resistance is between 16 KΩ . to 16 MΩ , which is much smaller than the applied external load of 500 MΩ̃ Here we ignored the resistance produced by the ZnO film at the bottom of the nanowires because it is very large and covers the entire area of the substrate, thus, the inner resistance is dominated by the NW. The equivalent capacitance of the NW is $C \approx \tau/R_L \approx 1.2$ pF.

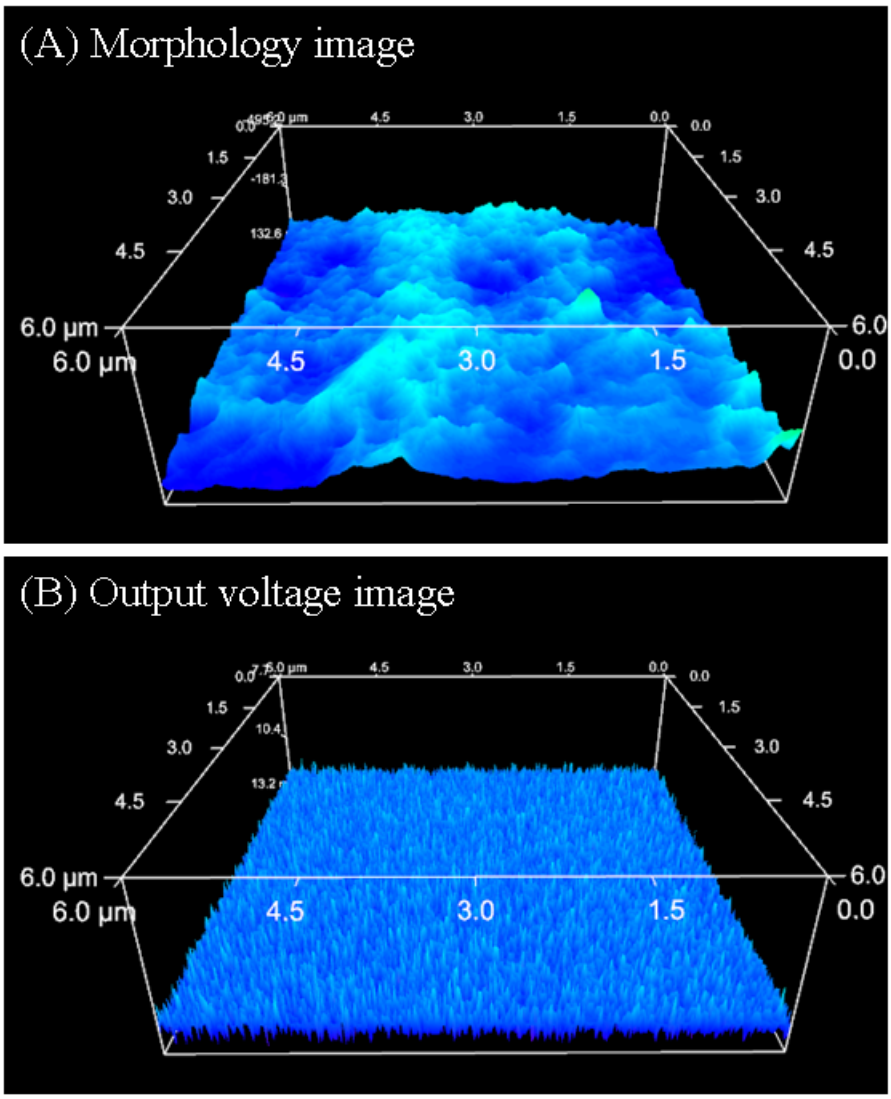

Figure 4.9 Conductive AFM scanning images of metal film. (A) topography image (B) corresponding electrical image

To ensure the voltage output signal in Fig. 4.3B is due to piezoelectric induced charging effect rather than friction or contact potential, we immediately scanned the AFM tip at a side area covered by a metal film of the sample under exactly the same experimental conditions used for acquiring Fig. 4.3B. The output morphology image (A) and the voltage signals (B) of the metal film are displayed as Figure 4.9 above. The output voltage shows no peaks but remains at the noise level, indicating that a metal film

even with a different contact potential does not produce the observed discharge process. The data rule out the possibility of friction or contact potential being the cause of the observed charging event.

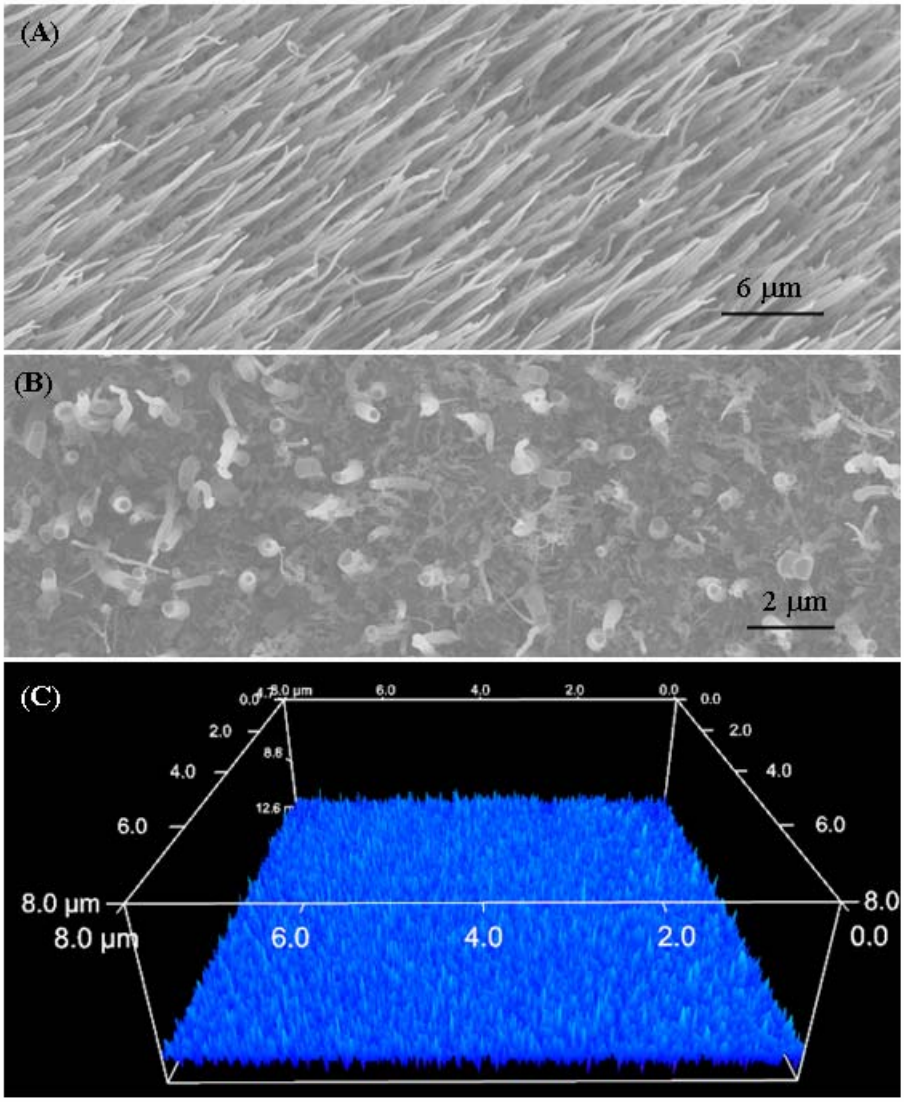

Figure 4.10 Experiment on carbon nanotube (A) SEM image of the side view aligned carbon nanotube. (B) SEM image of the top view of aligned carbon nanotube. (C) Corresponding electrical image from the conductive AFM scanning

To ensure the voltage output signal in Fig. 4.3B is due to piezoelectric induced charging effect rather than friction or contact potential, we carried out similar experiments using aligned carbon nanotubes. Figure 4.10 (A, B) are Side and top views of aligned carbon nanotubes. (C) The output voltage image shows no peaks but noise, indicating that carbon nanotubes do not produce the discharge process presented in Fig. 4.3B for ZnO nanowires. The data rule out the possibility of friction or contact potential being the cause of the observed discharging event.

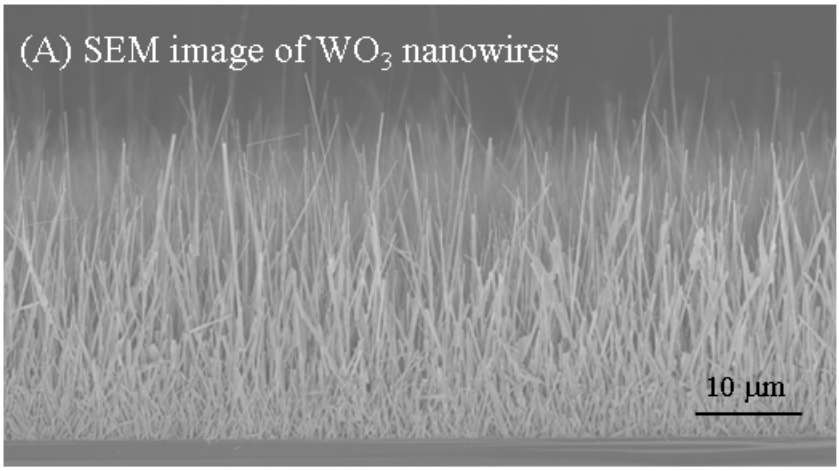

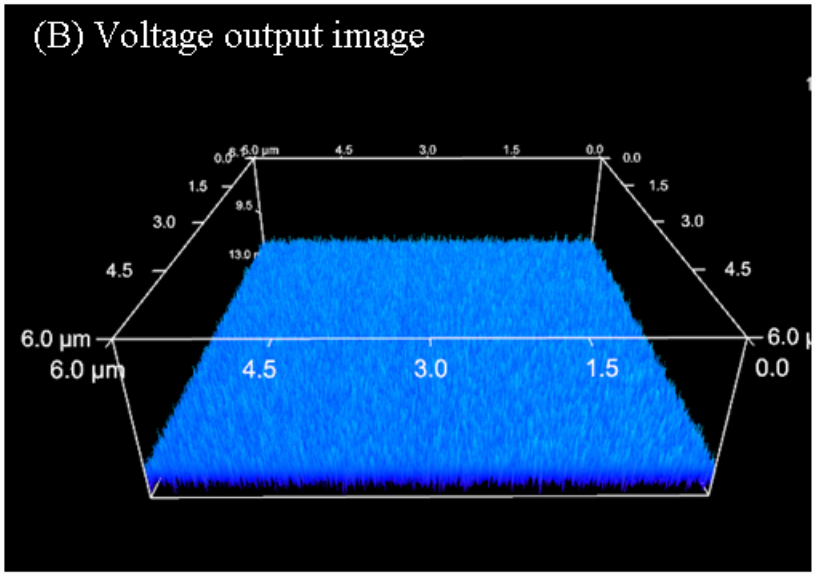

Figure 4.11 Experiment on aligned WO_3 nanowires sample (A) SEM image of WO_3 nanowires (B) corresponding electrical signals output from conductive AFM scanning

To ensure the voltage output signal in Fig. 4.3B is due to piezoelectric induced charging effect rather than friction or contact potential, we carried out similar experiments using aligned WO_3 nanowires. The output voltage image shows no peaks but noise, indicating that WO3 nanowires do not produce the discharge process presented in Fig. 4.3B. The data rule out the possibility of friction or contact potential being the cause of the observed discharging event for ZnO nanowires.

These data fully rule out the possibility of friction or contact potential being responsible for the observed voltage output phenomenon. The only possibility is piezoelectric behavior.

The efficiency of the electric power generated by this process can be calculated as follows. The output electric energy from one NW in one piezoelectric discharge (PED) event is $W_{PED} = V_0^2 C/2$ (as stated in section 4.1.1.3) where V_0 is the peak voltage of the discharge output. For simplicity, we approximately take the NW as a two-dimensional object for easy analytical calculation. The elastic deformation energy (W_{ELD}) created by the AFM tip for displacing the NW is $W_{ELD} = 3YIy_m^2 / 2L^3$ (as stated in section 4.1.1.5), where Y is the elastic modulus, I the momentum of inertia, L the length and y_m the maximum deflection of the NW. The elastic deformation energy is mainly dissipated in three ways: creating mechanical resonance/vibration after releasing the NW (as schematically shown in Fig. 4.3F), generating piezoelectric discharge energy W_{PED} for each cycle of the vibration, and overcoming the friction/viscosity from the environmental medium. The mechanical resonance of the NW continues for many cycles, but it is eventually damped by the viscosity of the medium. The piezoelectric discharge energy W_{PED} is generated in each cycle of the vibration, but the AFM tip in the current experimental design only catches the energy generated in the first cycle of vibration. With

consideration the energy dissipated by the NW in the first cycle of vibration W_{ELD} (refer to section 4.1.1.6), the efficiency of converting mechanical energy to electric energy is: $W_{PED}/\ W_{ELD}$. Therefore, an efficiency of 17-30% has been received.

4.1.1.8 The Unique Piezoelectric and Semiconducting Dual Properties of ZnO Nanowire

The physical principle for creating the piezoelectric discharge energy is related to the uniquely coupled piezoelectric and semiconducting dual properties of ZnO. For a vertical straight ZnO NW (Fig. 4.12A), The deflection of the NW by AFM tip creates a strain field, with the outer surface (right-hand side) being stretched (positive strain ε) and inner surface (left-hand side) compressed (negative strain ε) (Fig. 4.12B). Due to the electric-mechanical coupling characteristic of ZnO, electric field E_z along the NW (z direction) will be created inside its volume due to piezoelectric effect, $E_z = \varepsilon_z/d$, where d is the piezoelectric coefficient[78] along the nanowire direction that is normally the positive c-axis of ZnO with Zn atomic layer being the front terminating layer[79]. The piezo-electric field direction is closely parallel to the z-axis (NW direction) at the outer surface and anti-parallel to the z-axis at the inner surface (Fig. 4.12C). Under the first order approximation, across the width of the NW at the top end, the electric potential distribution from the left-hand side surface (compressed) to the right-hand side surface (stretched) is approximately between V_s^- to V_s^+ [with $V_s^{\mp} = \mp 3Ty_m/4Ld$ (refer to section 4.1.1.4)], where T is the thickness of the NW). The electrode at the root of the NW is grounded. Note the V_s^+ and V_s^- are the piezoelectric effect produced voltages, which are typically larger than a few tens of volts[80], respectively. The potential is created by the relative displacement of the Zn^{2+} cations with respect to the O^{2-} anions due to piezoelectric effect in the wurtzite crystal structure; thus, these ionic charges cannot freely move and cannot recombine without releasing the strain (Fig. 4.12D). This means that the potential difference is kept

as long as the deformation is in place and no foreign free charges (such as from the metal contacts) are injected in.

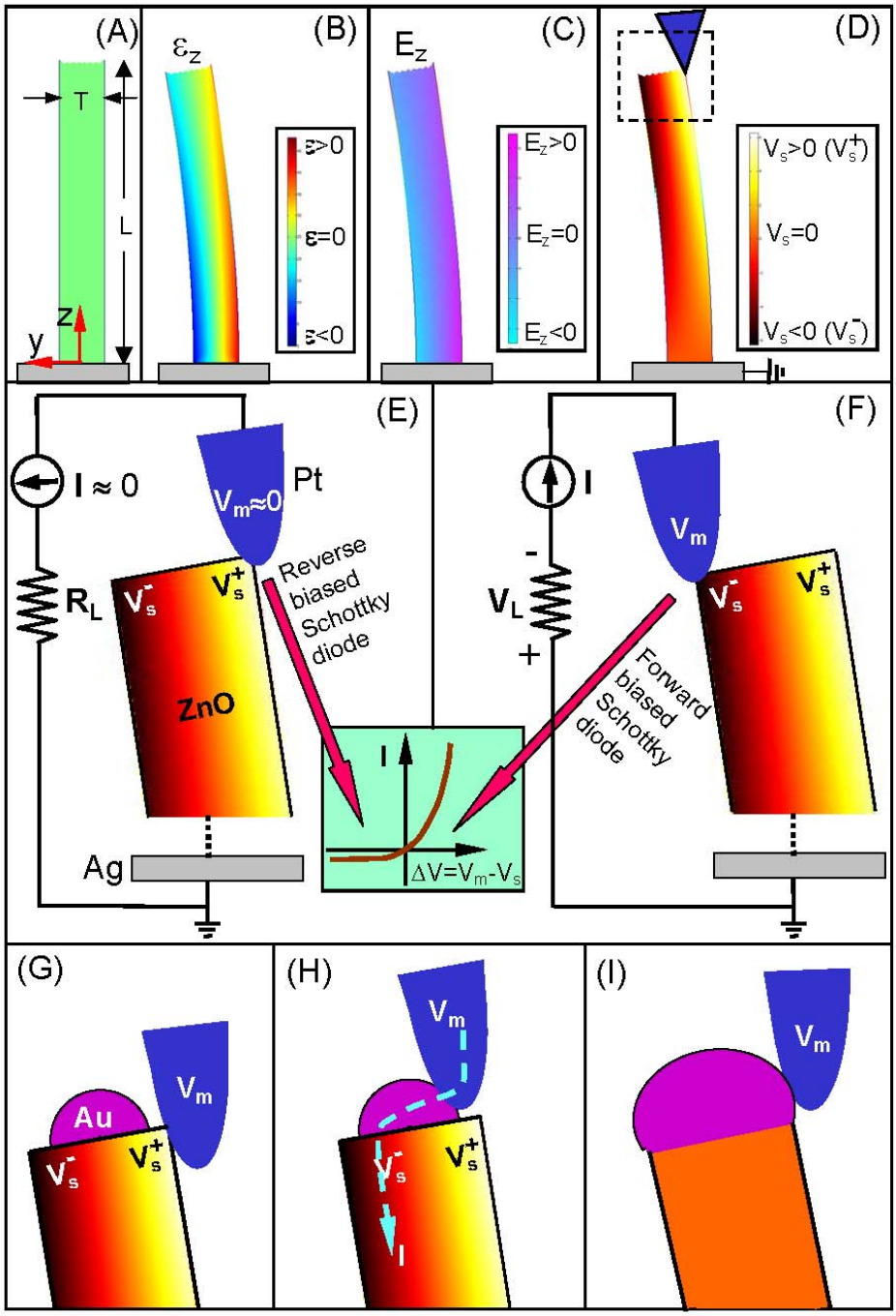

Figgure 4.12 Physical principle of the observed power generation process of a piezoelectric ZnO NW, showing a unique coupling of piezoelectric and semiconducting

properties in this metal-semiconductor Schottky barrier governed transport process. (**A**) Schematic definition of a NW and the coordination system. (**B**) Longitudinal strain ε_z distribution in the NW after being deflected by an AFM tip from the side. The data was simulated by FEMLAB for a ZnO nanowire of length 1 μm, aspect ration of 10. (**C**) The corresponding longitudinal piezoelectric induced electric field E_z distribution in the NW. (**D**) Potential distribution in the NW as a result of piezoelectric effect. The dashed box indicates the area to be examined in details in (E, F). (**E, F**) Metal and semiconductor contacts between the AFM tip and the semiconductor ZnO NW at two reversed local contact potentials (positive and negative), showing reverse and forward biased Schottky rectifying behavior, respectively (see text). It is this oppositely biased Schottky barrier across the NW makes it possible to preserve the piezoelectric charges and later produce the discharge output. Inset is a typical I-V characteristic of a metal-semiconductor (n-type) Schottky barrier. The process in (E) is built up the potential; the process in (F) is to discharge the potential. (**G, H**) Contact of the metal tip with a ZnO nanowire having a small gold particle at the top. The piezoelectric potential is built up in the displacing process (G), and later the charges are released through the compressed side of the NW (H). (**J**) Contact of the metal tip with a ZnO nanowire with a large gold particle at the top. The charges are gradually "leaked" out through the compressed side of the NW as soon as the deformation occurs, thus, no accumulated potential will be created.

The contacts at the top and the root of the NW are non-symmetric. The contact at the bottom is ZnO NW with ZnO film and the film with Ag, thus, the effective contact is between ZnO and Ag. Since the electron affinity of ZnO is 4.5 eV[81] and the workfunction of Ag is 4.2 eV, there is no barrier at the interface, thus, the contact between ZnO and Ag is Ohmic. At the tip of the NW, however, since the workfunction of Pt is 6.1 eV and the electron affinity of ZnO is 4.5 eV, the Pt-ZnO contact is Schottky[82], which dominates the entire transport process. As discussed above, the compressed side of the semiconductor

ZnO NW has negative potential V_s^- and the stretched side has positive potential (V_s^+). This is the cause of the two distinct transport processes across the Schottky barrier at the interface.

We now consider the case of NW without Au particle at the tip. In the first step, the AFM conductive tip that induces the deformation is in contact with the stretched surface of positive potential V_s^+ (Fig. 4.12D and E). Since the Pt metal tip has a potential of nearly zero, $V_m = 0$, the metal tip - ZnO interface is negatively biased for $\Delta V = V_m - V_s^+ < 0$. With consideration the n-type semiconductor characteristic of the as-synthesized ZnO NWs, the Pt metal- ZnO semiconductor (M-S) interface in this case is a reversely biased Schottky diode (Fig. 4.12E), resulting in little current flowing across the interface. In the second step, when the AFM tip is in contact with the compressed side of the NW (Fig. 4.12F), the metal tip - ZnO interface is positively biased for $\Delta V = V_L = V_m - V_s^- > 0$. The M-S interface in this case is a positively biased Schottky diode, resulting in a sudden increase in the output electric current, e.g., a sharp increase in output voltage V_L (positive). The current is the result of ΔV driven flow of electrons from the semiconductor ZnO NW to the metal tip. The flow of the free electrons from the loop through the NW to the tip will neutralize the ionic charges distributed in the volume of the NW and thus reduce the magnitude of the potential V_s^- and V_s^+. Therefore, the output voltage V_L starts to drop and reaches zero until all of the ionic charges in the NW are fully neutralized. This is why the discharge curve in Fig. 4.3E is nearly a symmetric peak. It is also anticipated that the discharge occurs when the NW is bent nearly to the maximum deflection according to the model, thus the voltage peak should have a small offset in reference to the corresponding topography peak along the direction of tip scan. This agrees to the experimental observation shown in Fig. 4.3D.

We now consider the case of a ZnO NW with a small gold particle at the top as a result of VSS growth (see Figs. 4.12G and H). In the first step of tip displacing the NW,

the tip is directly in contact with the ZnO NW but not the gold particle (Fig. 4.12G) due to its small size and hemisphere shape (see the TEM image in Figs. 4.1B and Figure 4.2). A similar process as described in Fig. 4.12E occurs, thus, no output voltage will be observed. When the tip is in contact with the gold particle, the tip is integrated with the particle as one metal contact; and at the local interface between the gold particle and the negatively charged, compressed side of the ZnO NW (V_s^-), a forward biased Schottky diode is formed; thus, the current flows from the tip through the gold particle to the interface region with negative piezoelectric voltage (V_s^-) (Fig. 4.12H). A discharge process similar to that shown in Fig. 3F occurs, and a sharp voltage output is produced.

In a case of a NW with a large gold particle that fully covers its top (Fig. 4.12I), the metal tip is directly in touch with the gold tip at the beginning of the forced displacement. With consideration the conducting channel at the compressed side of the NW, the polar charges produced by the displaced Zn^{2+} and O^{2-} ions due to piezoelectric effect are immediately neutralized by external free charges as soon as they are produced by the deformation. Therefore, no accumulative potential profile is formed at the M-S interface, and no measurable output voltage will be detected in the experimental set up we have designed (Fig. 4.1C).

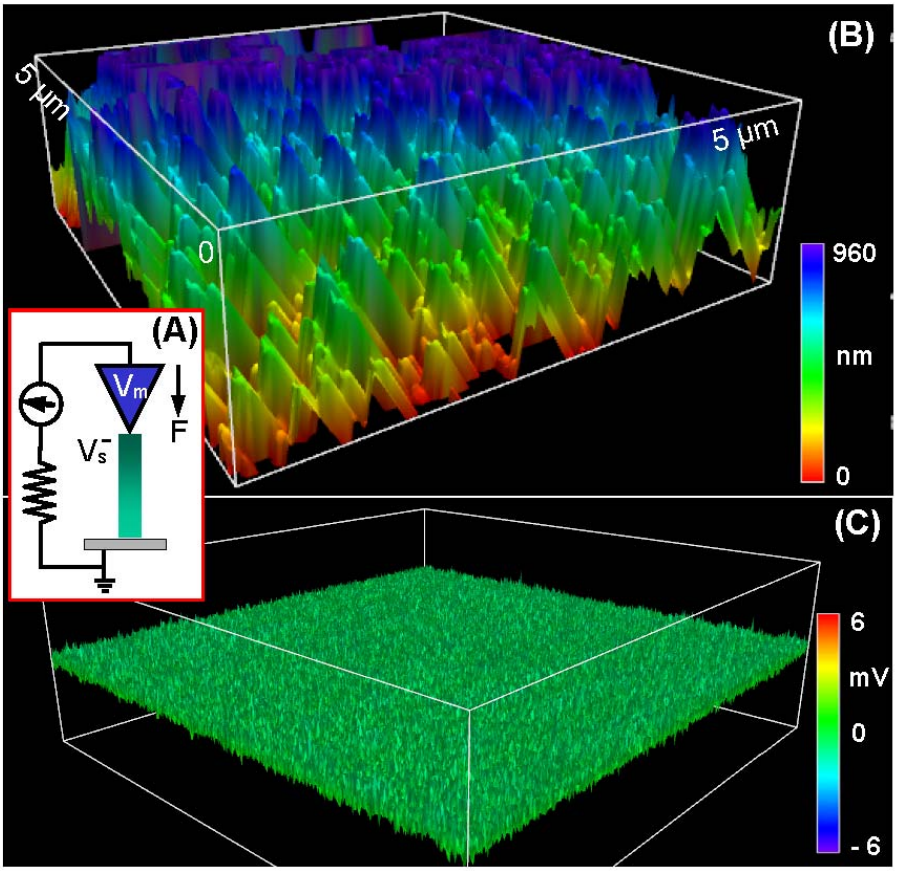

Figure 4.13 Electro-mechanical coupled discharging process of aligned piezoelectric ZnO NWs observed in tapping mode. (**A**) The experimental set up. (**B**) Topography image and (**C**) corresponding output voltage image of the NWs. The tapping force was 5 nN, tapping frequency 68 KHz and tapping speed 6 μm/s. The voltage output contains no information but noise, proving the physical mechanism demonstrated in Fig. 4.12.

To further examine the physical process proposed above, we measured the piezoelectric voltage output of the same samples of aligned ZnO NWs but at the AFM tapping mode. In this case, the deformation occurs longitudinally and there is no side displacement. The NW is vertically compressed, thus the voltage created at the top of the NW is negative V_s^-, provided the root electrode is grounded (Fig. 4.13A). There is no

voltage drop across the width of the NW. Thus, across the metal tip – ZnO interface, a positively biased Schottky diode is formed; hence, the electrons can freely flow across the interface. As a result, the electrons flow as the deformation occurs, resulting in no accumulation of net charges in the NW volume. This type of slowly "leaked" current produces no detectable signal. Therefore, for the ZnO NWs whose AFM image in tapping mode is shown in Fig. 4.13B, no output voltage V_L is detected beyond the noise level (Fig. 4.13C).

4.1.1.9 Possibility of Powering Nanodevices Using Nanogenerator

The piezoelectric energy output by one NW in one discharge event is ~ 0.05 fJ. For a NW of size 40 nm and length of 0.5 μm, The output power volume density per NW is ~ 80 MW/cm^3, about 450 times higher than the power volume density produced by bulk PZT power generator [83]. This is possibly due the largely increased elastic deformability limit of the NW at small dimensions[84]. For such a NW, the resonance frequency is ~ 1 GHz , the output power of the NW will be ~ 50 nW, if the density of NWs per unit area on the substrate is 20/μm^2. The output power density is ~ 1 μW/μm^2. This may be enough to drive a single nanowire/nanotube based device[85, 86, 87]. Therefore, it can be foreseen that, if we can find a way to induce the resonance of an array of nanowires and output the piezoelectric discharge induced power, a significantly strong power source may be possible for self-powering nanodevices. Alternatively, using an acoustic wave or ultrasonic wave of frequency from 1 MHz to 1 GHz to excite the vibration of the NWs, the maximum output power density could be ~ 1 nW/μm^2 to as high as 1 μW/μm^2.

4.1.2 Nanogenerator on Plastic Substrate

Research and applications in biomedical science and technology usually require various portable/wearable, easy-to-use, and/or implantable devices that can interface with biological systems[88, 89]. Organic or organic-inorganic hybrid micro and nano-electronics

have long been a choice[90,91,92,93,94]. But all of these devices require a power source, required to generate or store electrical energy created through chemical, mechanical, or thermal processes, such as electrochemical cells [95], piezoelectric transducers [96], thermoelectric transducer[97] and pyroelectric transducers[98]. Finding the power source has remained as a major challenge for many devices in bioengineering and medical devices.

The nanogenerator described in section 4.1.1 is a perfect solution to the nanopower source problem but the ceramic or semiconductor substrates use for growing ZnO NWs are hard, brittle and cannot be used in areas that require a foldable or flexible power source, such as implantable bio-sensors. In this paper, using the ZnO NW arrays grown on a flexible plastic substrate, we have demonstrated the first success of flexible power source built on conducting polymer films. Two specific advantages have been demonstrated in this study towards potential applications. One is the cost-effective, large-scale solution approach used to grow ZnO NW arrays at a temperature lower than 80 ^{o}C. The other is the large-degree of choice of flexible plastic substrates used for growing aligned ZnO NW arrays, which could play an important role in the flexible and portable electronics. Various dimensions, shapes and orientations of NWs and microwires of ZnO on flexible plastic substrate have been proved to be capable of producing piezoelectric voltage output, giving a real advantage for energy harvesting using large scale ZnO nanowires arrays. The voltage generated from a single NW can be as high as 50 mV, which is large enough for powering many nanodevices.

4.1.2.1 The synthesis of ZnO nanowires on Flexible Substrate

The ZnO NWs were grown in solution through chemical synthesis.

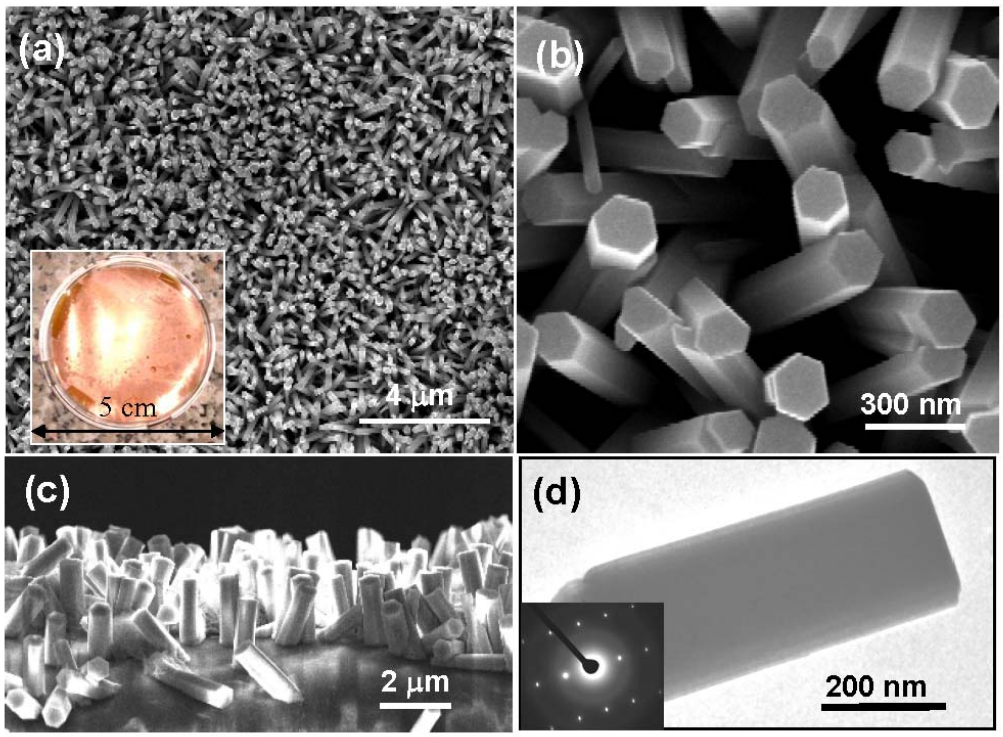

Figure 4.14 A series of SEM and TEM images of the typical ZnO NW arrays grown on a plastic substrate. a) and b) are respectively a low-magnification top view of the densely aligned NW arrays and a corresponding magnified SEM image. The inset is an optical image of the sample with NWs on polymer surface. c) A side view SEM image displaying orientation aligned ZnO NWs normal to the plastic substrate. d) A typical TEM image of an individual ZnO NW, inset is a corresponding selected area electron diffraction pattern.

Figure 4.14 shows a series of SEM and TEM images of the typical ZnO NW arrays grown on a conductive plastic substrate. Fig. 4.14a gives a low-magnification top view of the densely aligned NW arrays. The aligned NWs have a uniform diameter of 200-300 nm with a hexagonal cross-section, as indicated by the magnified SEM image in Fig. 4.14b. The side view SEM image in Fig. 4.14c displays orientation alignment of the grown ZnO NWs of lengths ~ 2 μm normal to the plastic substrate. Fig. 4.14d is a typical TEM image of a ZnO NW, which has a diameter of ~300 nm. The corresponding electron

diffraction pattern indicates that the NW growth direction is [0001] and its side surfaces are $\{2\bar{1}\bar{1}0\}$.

It is worth noting that by controlling the synthesis parameters such as temperature, concentration, reaction time and plastic substrate surfaces, NWs of different density distribution, dimensionality and orientation alignment have been achieved for electrical measurements. Figures 4.15a and b are respectively a low-magnification and an enlarged SEM image for the sparsely grown ZnO NW arrays on the plastic substrate. The grown NWs have a density of ~1/μm^2 on an Au-coated plastic substrate. The NW is of typical dimensions of 100-350 nm in widths and ~1 μm in heights. The inset SEM image in Fig. 4.15b is a side view of the NW array perpendicular to the plastic substrate.

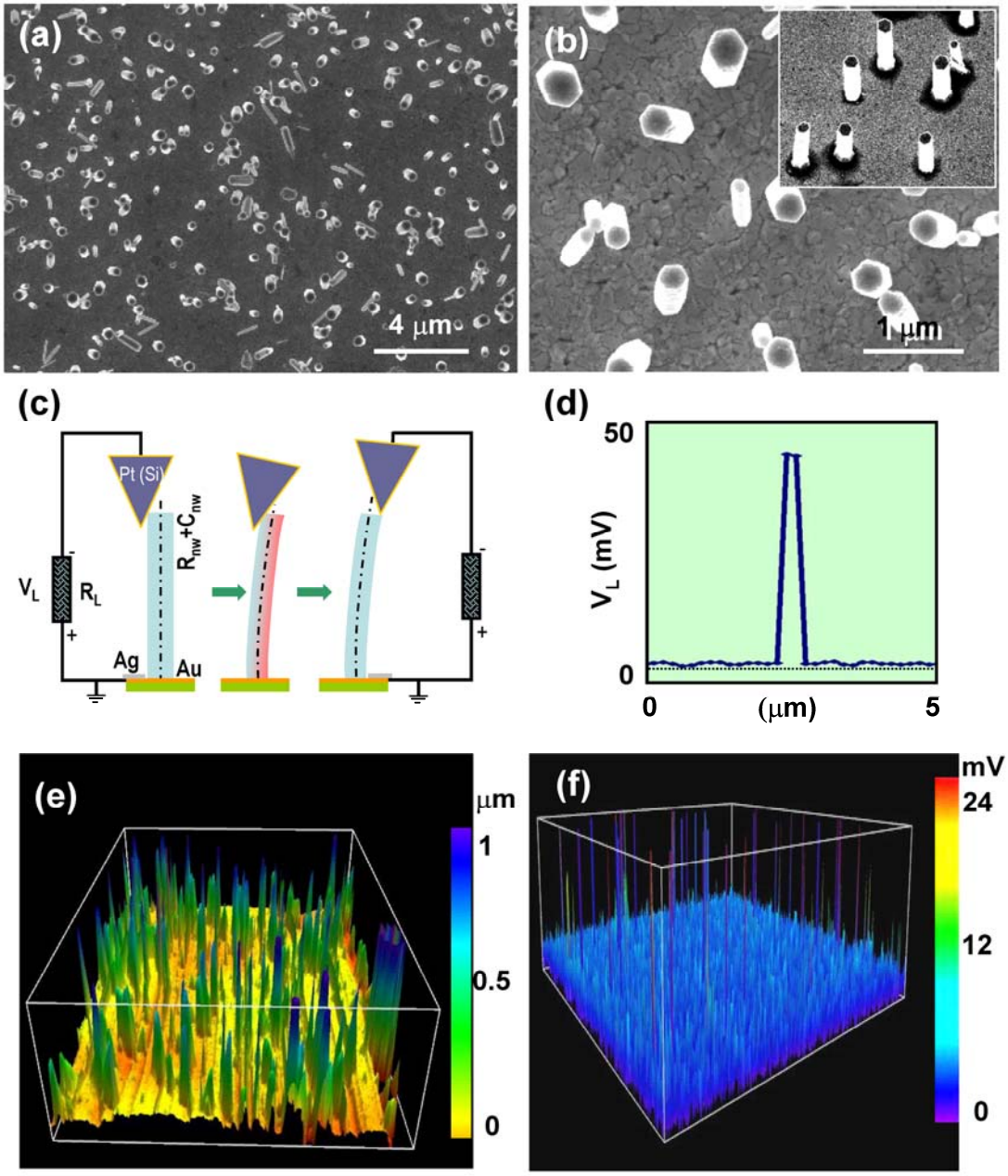

Figure 4.15 a) and b) are respectively a low-magnification and an enlarged SEM images for the sparsely grown ZnO NW arrays on the plastic substrate. c) Experimental schematic for the conductive AFM measurement on the NWs array. Note the polarity of the defined output voltage on the external load. d) typical voltage output profile for the AFM tip scanning over a single NW on the plastic substrate. e) and f) are 3D plotted

AFM topography image and voltage output profile received by scanning the AFM tip over a 40 μm x 40 μm area of aligned ZnO NWs on the plastic substrate.

4.1.2.2 Power Generating from ZnO NWs on Flexible Substrate

Figure 4.15c is an experimental set up for measuring the mechanically induced piezoelectric discharge from individual NWs. A conductive Si tip coated with Pt film with a cone angle of 70^{o} was used for the AFM measurement. The rectangular cantilever had a calibrated normal spring constant of 1.857 N/m. In the AFM contact mode, a constant normal force of 5 nN was maintained between the tip and sample surface. The tip scanned over the top of the ZnO NWs, the tip height was adjusted according to the surface morphology and local contacting force. For the electric contact at the bottom of the NWs, silver paste (Ag) was applied to connect the Au film on the plastic substrate surface with the measurement circuit. The contact of Ag and ZnO produces an Ohmic contact[99]. The output voltage across an external load of resistance R_L = 500 megohm was continuously monitored as the tip scanned over the NWs. In contact mode, as the tip scanned over the vertically aligned NWs, the NWs were bent consecutively. The tip forces the elastic deflection of the oriented ZnO NWs, and produces a charge separation and a voltage drop across the diameter of the NW, with the stretched side and compressed side have positive and negative piezoelectric potential, respectively. The center axis of the NW, as indicated by a doted line, remains neutral.

As the conductive tip scanning across the neutral axis, the discharge occurs when the tip touches the compressed side of the NW. A single NW of diameter 300 nm can produce an output voltage discharge of ~ 45 mV (Fig. 4.15d), which is the voltage drop across the external resistor converted using the measured electric current. In fact, the true output voltage should be higher if we consider the inner resistance of the NW. Figure 4.15d is a typical voltage output for an AFM tip scanning over a single NW. Due to the limited scan speed of the AFM tip in comparison to the discharge time, only two data

points were captured around the peak area, which may suggest that the true peak could be twice in height of the measured 45 mV shown in this profile.

The scanning speed of the AFM tip was 53.51 μm/s, and the full width at half maximum (FWHM) of the peak is 234 nm. So the lifetime decay constant of the circuit shown in Fig. 4.15c is estimated to be τ_c = 4.4 ms. Based on the equation of $\tau_c = (R_L + R_{nw})C_{nw}$, where R_L and R_{nw} are respectively the resistances for the external load (500 Mohm) and the ZnO NW, and C_{nw} is the capacitance of the NW and the measurement system. As previously reported, the R_{nw} is negligible in comparison to the external load, thus, the capacitance of the NW can be calculated to be $C_{nw} \approx \tau_c/R_L$. The output piezoelectric energy W_o for a single pulse is

$$W_o = \frac{1}{2} C_{nw} V_p^2 = \tau_c V_p^2/2R_L = 8.9 \times 10^{-15} \text{ J}$$

Here W_o only represents the harvested electric energy from the first half cycle of the NW resonance due to a single touch of the tip with the NW.

The power was calculated based on the average energy generated within the life time of the resonance, and it was assumed that the energy generated for half of the cycles of the resonance was collected. The dimensions of a single NW here typically are 300 nm in diameter with a hexagonal cross section, and ~ 1 μm in length. According to the mechanical vibration theory, the first harmonic resonance frequency of the NW can be calculated to be ~70 MHz; considering the damping effect in air, the lifetime of a single NW is ~ 50 μs [100]. So the effective cycles for energy harvest are about 3500 cycles. With consideration of the decay of vibration amplitude of the NW for the subsequent resonance, the output power by a single NW is 10-20 pW.

Figure 4.15e is a three-dimensional (3D) plot of the topography AFM image of the scanned ZnO NWs array in a 40 μm x 40 μm area, the scanning direction is from the front to the backside, which can be seen from the bumped but line traces on the flexible plastic substrate. Due to the flexibility of the plastic substrate, in spite of a firm fixation by the

silver paste, the substrate surface profile under tip contact was a kind of wavy. Relative to the plastic substrate, the NWs array was revealed to have a height distribution of 0.5-2.0 μm. The corresponding 3D plot of the voltage output image is shown in Fig. 4.15f. It can be seen that there are a number of sharp peaks that represent voltage outputs ranging of 15-25 mV. By counting the pulse numbers shown here with respect to the number of NWs in the topography profile in Fig. 4.15e, the ratio of voltage peaks to the number of available NWs is 90:150, about 60%, which suggests that the discharge events of the NW captured by the AFM tip are at least about 50% of the NWs. In fact, due to the limitation of the data collecting speed of the AFM, which has a data step size of ~156.2 nm in this measurement, the discharge peaks of some NWs were missed possibly due to poor contact between the tip and the NWs, and/or due to the multiple contact with neighboring NWs. It is suggested both suitable bonding strength between ZnO NWs and polymer substrate and uniform density distribution of NWs array might be very important in terms of improving the piezoelectric discharge efficiency. These two issues together with the power output calculations will be explored in the following discussions.

To calculate all of the total number of NWs that effectively produced electrical energy output, it is assumed that the average voltage peak height is ~20 mV, and the density of ZnO NWs on the plastic substrate is very conservely estimated to be 1 /μm^2, the power density per unit substrate area is ~1-2 pW/μm^2, i.e. 0.1-0.2 mW/cm^2, which is large enough for powering a variety of devices that operate at lower-power consumption, such as MEMS, NEMS and other nanoscale devices.

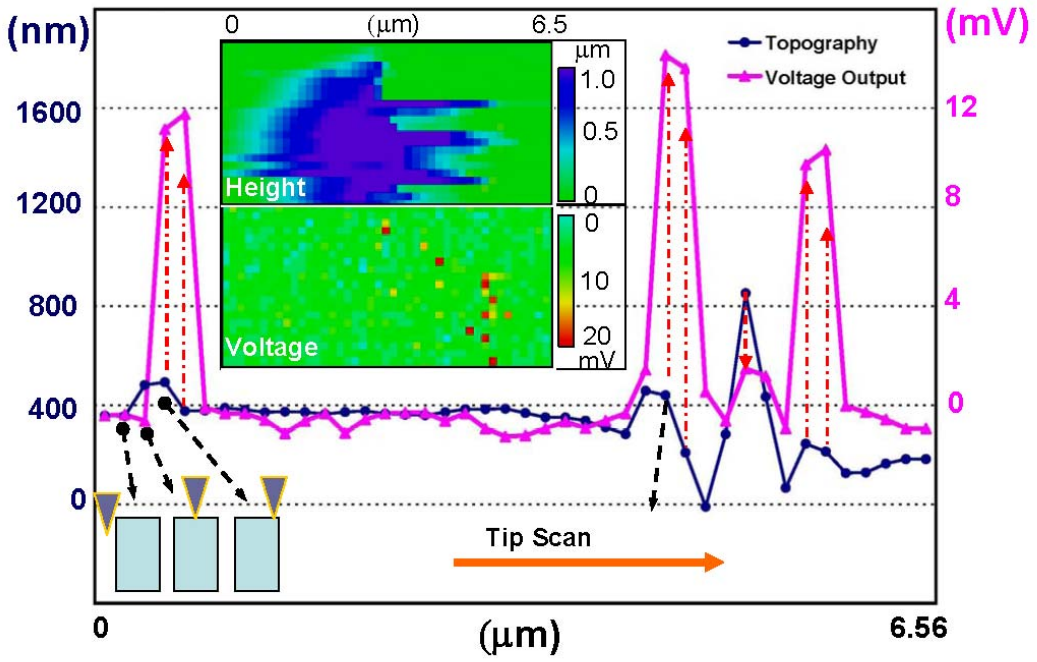

Figure 4.16 The simultaneously recorded line scanning topography image (blue dotted line) and corresponding voltage output profile (red line) from several aligned ZnO NWs. The inset at the upper part is a two-dimensional height profile (top) and the simultaneously recorded voltage output image (bottom) by scanning the tip across an area of 6.5 μm x 3.2 μm. Schematic tip to NW local contacts are displayed at the left-bottom corner for the corresponding locations.

Figure 4.16 displays the simultaneously recorded scanning height topography (blue line) and voltage output profile (red line) for a line scan of the AFM tip across the ZnO NW array. In the scanning range of 6.56 μm, at least four NWs have been contacted based on the topography profile. As registered with the topographical profile, the corresponding voltage output profile also shows four peaks of heights 12, 15, 2 and 10 mV, respectively. Comparing to the topography data points, each time the voltage output peak starts to increase when the AFM tip touches the flat cross-section of the NW, and the voltage peak reaches the maximum when the AFM tip reaches the side edge of the top flat

cross-section of the NW. When the AFM tip starts crossing the central axial line of the NW, the voltage discharge begins, which occurs in the middle of two data points, corresponding to the center of the discharge peak. When the tip completely releases the NW tip, the discharge is determined by the characteristics of the external circuit. The delay in voltage peak in reference to the topological profile is entirely consistent to the mechanism presented previously.

In the inset of Fig. 4.16, two-dimensional AFM topographical image and the corresponding voltage/current output image recorded simultaneously are displayed when the AFM tip scans over a 6.5 μm x 3.2 μm area. The height profile in the top indicates that the local density of the NWs are so high that the AFM tip could not resolve them individually due to tip size effect, so only the surrounding NWs edges could be resolved. From the corresponding voltage output profile, it is revealed that the red dots distribute only at the extreme right-hand side, indicating that the discharge occurs at the end of the tip scan over the NWs. In this case, the local high density of NWs array has prevented the deflection event from completion without a multiple contacts. Therefore, a reasonable NWs density distribution matching to the tip size and scanning speed would be necessary for improving the voltage output number.

In our previously report for the NWs of 20-40 nm in diameter and 0.2-0.5 μm in lengths grown on a sapphire substrate, a single NW can generate ~0.5 pW at 10 mV of electrical power using AFM tip deflection at a 5 nN contact force. Here, for the NW with diameter of 300 nm and lengths of 1 μm, grown on a polymer substrate, the output power reaches ~ 5 pW at 45 mV, which has been improved by an order of magnitude.

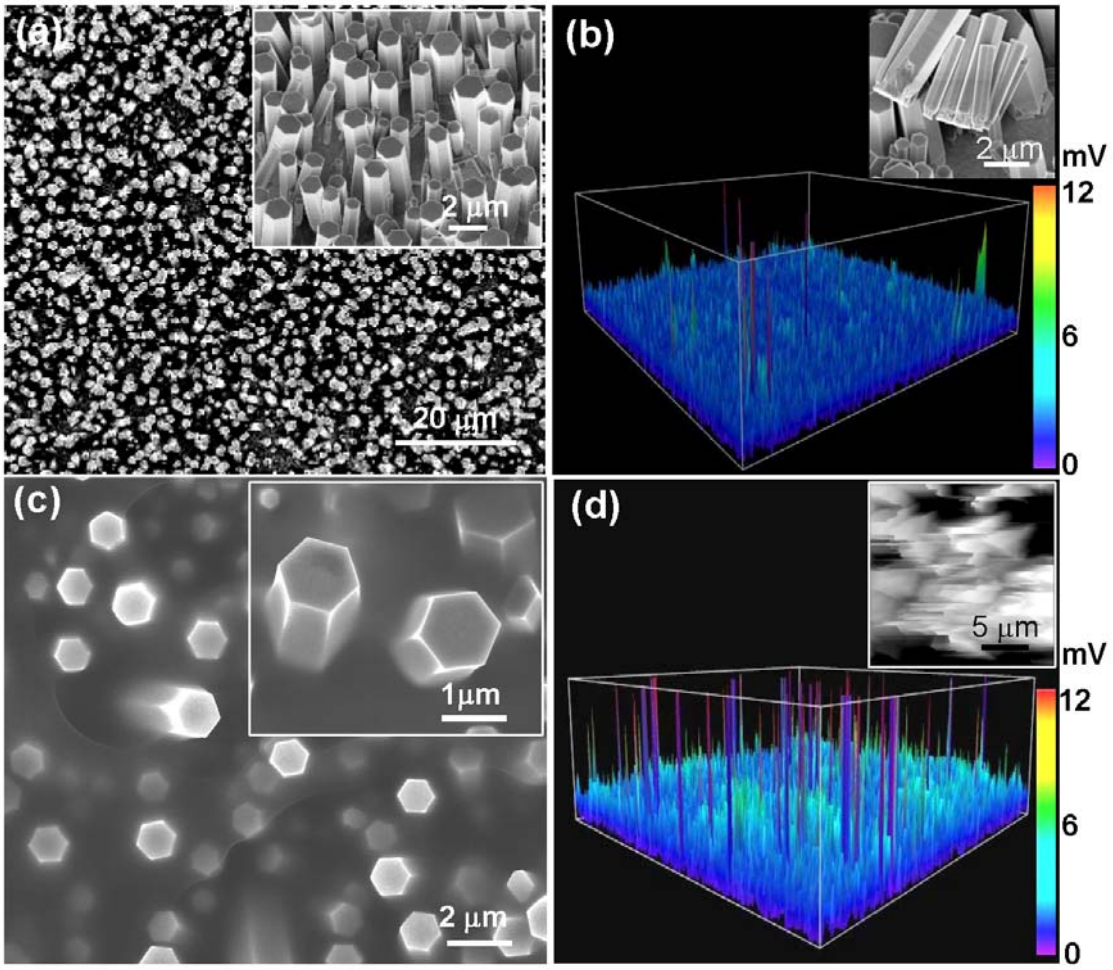

Figure 4.17 a) and b) are respectively a top view SEM image of the as-grown densely packed and vertically aligned ZnO microwires array (inset: a side view of aligned microwires array) on the plastic substrate and the corresponding AFM voltage output profile (20 μm x 20 μm). The inset SEM image in b) shows a portion of the microwires pushed-down by the AFM tip. c) and d) are respectively a top view SEM image showing the PMMA coating reinforced ZnO wires aligned on the plastic substrate (inset: an enlarged view of PMMA encapsulated microwires) and the corresponding AFM voltage output profile under AFM measurement (inset: topography image of the 20 μm x 20 μm area)

To evaluate the power-generating capability of ZnO NW array grown on the plastic substrate, differently configured NW arrays in terms of dimensions and

orientations have been tested for demonstrating the performance of the nanogenerator, which will be described in the following figures 4.17 and 4.18. Figure 4.17a is a top view of an as-grown densely packed and vertically aligned ZnO microscal wire array on the plastic substrate. The microwires are uniform with a width of 1-2 μm, and a height of 5-10 μm. The inset SEM image is a side view of the aligned wire array, which reveals a good vertical alignment on the plastic substrate. The separation of the microwires is 0.1-1 μm. The substrate surface area covered by the wires is 50-80% (the surface coverage in the case of Fig. 4.15 is only ~10%). Under the conductive AFM test, using the same test parameters as that for the case in Fig. 4.15, it is found that the voltage discharge events occurred are a lot less than that for the sparsely aligned NWs, simply indicating the densely packed NWs are not the optimum choice for enhancing the power output of the nanogenerators. Figure 4.17b is the corresponding 3D plot of the voltage image for an area of 20 μm x 20 μm. It is clearly seen that only a few (~10) sharp voltage peaks emerged out of the noise level. It is suggested that the small normal tip force (5 nN) may not be sufficiently strong to deflect the ZnO microwires. To find out why only a few peaks were detected in the AFM scan in an area that has at least 50 wires, the tested sample was examined by SEM. In the area after tip scanning, only a few wires have been left standing upwards on the substrate, most of the wires in the array have been pushed down by the AFM tip, as shown by the inset SEM image. Evidently several possible reasons may account for this result. The first reason is the adhesion between the Au coating base and the ZnO microwires is weak so that it cannot bear the force applied by AFM tip. The second reason could be that the microwire is too strong to be elastically deformed; once it is pushed by the AFM tip, they tend to be displaced owing to a weak link to the substrate rather than elastic deformation. The third reason is that the density of the wires is so high that there is not much room for deflecting the wire by the AFM tip

without touching neighboring wires, thus, the piezoelectric current, if any, may have been slowly leaked out, resulting in no abrupt discharge signal.

To improve the bonding between the wires and the substrate, a PMMA coating of thickness ~200 nm on the substrate after wire growth was introduced. Figure 4.17c shows the ZnO microwire array on plastic substrate after the PMMA coating, it is clearly seen that the bottom portion of the wires array has been encapsulated by the PMMA coating (inset). The top portions of the wire array are clean after a 10 min UV irradiation following the spin-coating and soft-baking process. In Fig. 4.17c, the shorter wires have been buried by the PMMA coating; most of the long microwires standing on the surface. The AFM measured result is shown in Fig. 4.17d. The number of voltage peaks in an area of 20 μm x 20 μm has increased to ~50. The peak voltage output amplitude remains in the range of 6-12 mV. The inset is an AFM topography image of the corresponding microwires array affixed by PMMA. It is clearly seen that the microwires are firmly held on the plastic substrate during the tip scan, as presented by the topological image. It is suggested by using reinforcing layer of polymer coating, the NWs/substrate bonding can be significantly improved.

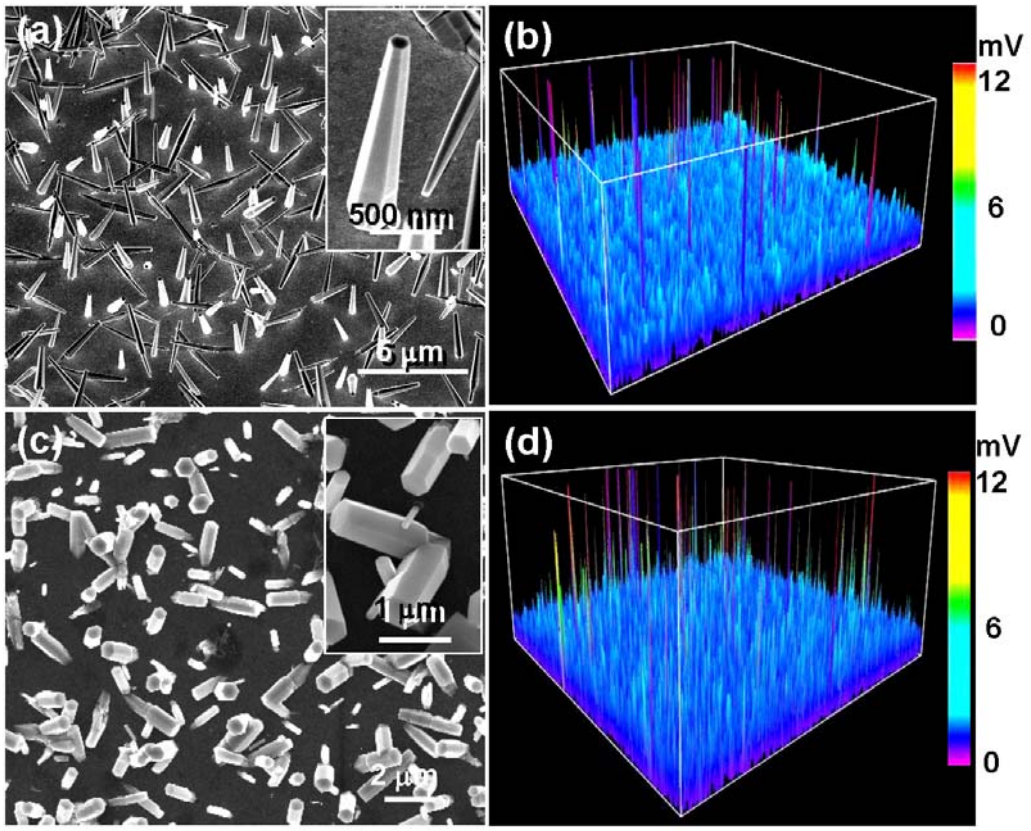

Figure 4.18 a) and b) are respectively a typical SEM image of sparsely grown aligned ZnO nanocones (inset: an enlarged view of a single nanocone) and the corresponding AFM voltage output profile (20 µm x 20 µm) under AFM measurement. c) and d) are respectively a typical top view SEM image of the randomly oriented ZnO NWs on a plastic substrate (inset: an enlarged view showing the randomly tilted NWs on plastic substrate) and the corresponding AFM voltage output profile (20 µm x 20 µm)

To find out the effect of NW shape and orientation on power generating, cone-shaped ZnO NWs and randomly oriented ZnO NWs on plastic substrates were grown and used for AFM measurements. Figure 4.18a is the as-grown cone-shaped ZnO hexagonal NWs with ~50% vertical alignment on the plastic substrate. The nanocones typically have tip diameters of 100-200 nm, base diameters of 300-500 nm and heights 3-5 µm (inset). Under the conductive tip deflection, only a number of voltage output peaks of 6-12 mV are observed (Fig. 4.18b). Figure 4.18c is a typical SEM image of the as-grown ZnO NWs

randomly oriented on the plastic substrate. Inset SEM image revealed the tilted hexagonal NWs rooted at the plastic substrate with dimensions of 200-600 nm in width, and 1-2 μm in height. The AFM measurement result is shown in Fig. 4.18d, which similarly has revealed an increased number of voltage output peaks of 6-12 mV. Therefore, it is suggested that as long as there is a process of bending the wire, no matter what kind of orientation with respect to the plastic substrate, the voltage/current signal is likely to be generated, leading to another validating advantage of the electricity harvesting utilizing the large scale NWs arrays made by solution approach.

In the literature, lead-zirconium-titania (PZT) ceramic is the most typical ceramic material for piezoelectric applications, which has been used for producing output voltage[101]. In comparison to PZT, the NW array grown on polymer substrate has the following advantages for generating electricity. First, the NW based nanogenerators can be subjected to extremely large deformation both on the NWs and the substrate, so that it can be used for flexible electronics as flexible/foldable power source. Secondly, the large degree of deformation that can be bared by the NWs is likely to have a much larger volume density of power output. Third, ZnO is a biocompatible and bio-safe material in contrast to PZT, it has the most profound potential for implantable power source in human body. Fourth, the flexibility of the polymer substrate used for growing ZnO NWs makes it feasible to accommodate the flexibility of human muscles so that we can use the mechanical energy (body movement, muscle stretching) in human body to generate electricity. Finally, ZnO NW nanogenerators can directly produce current due to its enhanced conductivity with the presence of oxygen vacancies.

4.2 Power Generating Process of Single ZnO Belt/Wire

The work discussed in the previous section 4.1 was based on measurements on an array of aligned ZnO nanowires. In this section, the detailed piezoelectric discharging

process of a single ZnO wire/belt is examined. By directly correlating the manipulation process of a wire/belt and the electric output voltage/current signal under atomic force microscopy, the details about the generation mechanism has been revealed. Discussion is given about the potential applications of this energy harvesting process from the environment.

4.2.1 Experiment Setup

The experiment was based on mechanical manipulation of a single ZnO wire/belt by an atomic force microscope (AFM). By selecting a long ZnO wire/belt that was large enough to be seen under an optical microscope, one end of the ZnO wire was affixed on a silicon substrate by silver paste, while the other end was left free. The substrate was an intrinsic silicon so its conductivity was rather poor. The wire laid on the substrate but kept a small distance from the substrate to eliminate the friction with the substrate except at the affixed side (Fig. 4.19A). The measurements were performed by AFM (Molecular Force Probe MFP-3D™ from Asylum Research) using a Si tip coated with Pt film (Electri-Lever AC240 from Olympus), which had a tetrahedral shape with an apex angle of 70° and 14 μm in height, and spring constant of 1.42 N/m. The measurements were done in AFM contact mode under a constant normal force of 5 nN between the tip and sample surface, and the scan area was 70 x 70 μm^2.

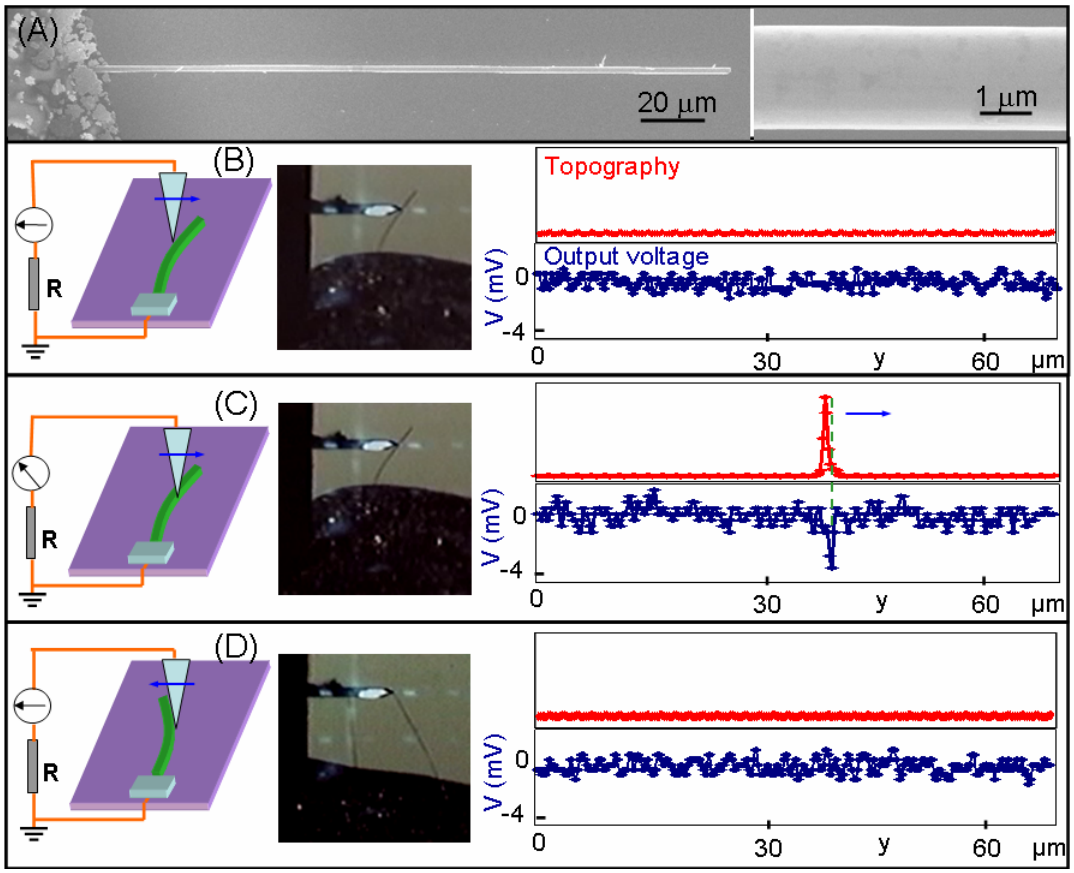

Figure 4.19 In-situ observation of the process for converting mechanical energy into electric energy by a piezoelectric ZnO wire. (**A**) SEM images of a ZnO wire with one end affixed by silver paste onto a silicon substrate and the other end is free. The wire has a hexagonal cross-section. (**B, C and D**) Three characteristic snapshots and the corresponding output voltage images when the tip scanned across the wire. The schematic illustration of the experimental condition is shown at the left-hand side, with the scanning direction of the tip indicated by an arrowhead. The scanning speed of the AFM tip was 105.57 μm/s and the sampling density is 256 per line. In (**B**), the AFM tip scanned over the top of the wire on the silicon substrate, and the voltage output is just in the noise level. In (**C**), the AFM tip touched the top end of the wire and the output voltage image showed a sharp negative peak. In (**D**), right after the AFM tip passed the top end of the wire and scanned towards its lower part, but without across the wire, no output voltage was detected.

Both the topography (feed back signal from the scanner) and the corresponding output voltage (V) images across a load were recorded simultaneously when the AFM tip was scanned across a wire/belt. The topography image reflects the change in normal force perpendicular to the substrate, which shows a bump only when the tip scans over the wire. The output voltage between the conductive tip and the ground was continuously monitored as the tip scans over the wire/belt. No external voltage was applied in any stage of the experiment. The entire experimental process and the output images were captured by video recording, so that we were able to directly visualize the electric generation process. The output data to be presented were obtained from snapshots of the characteristic events observed during the experiments.

The AFM tip scanned line-by-line at a speed of 105.57 μm/s perpendicular to the wire either from above the top end to the lower part of the wire or from the lower part towards the top end. For a wire with hexagonal cross-section (Fig. 4.19A), three characteristics features were observed. When the tip scanned above the top end of the wire without touching the wire but the silicon substrate, the output voltage signal was nothing but noise (Fig. 4.19B). When the tip scanned until it touched the top end of the wire, a spark output voltage signal was observed (Fig. 4.19C). The output voltage is negative for the load R_L for almost all of the observed cases, indicating the tip has a lower potential than the grounded silver paste. When the tip scanned down along the wire, it deflected the wire but could not go over it, and the output voltage showed no peak but noise (Fig. 4.19D).

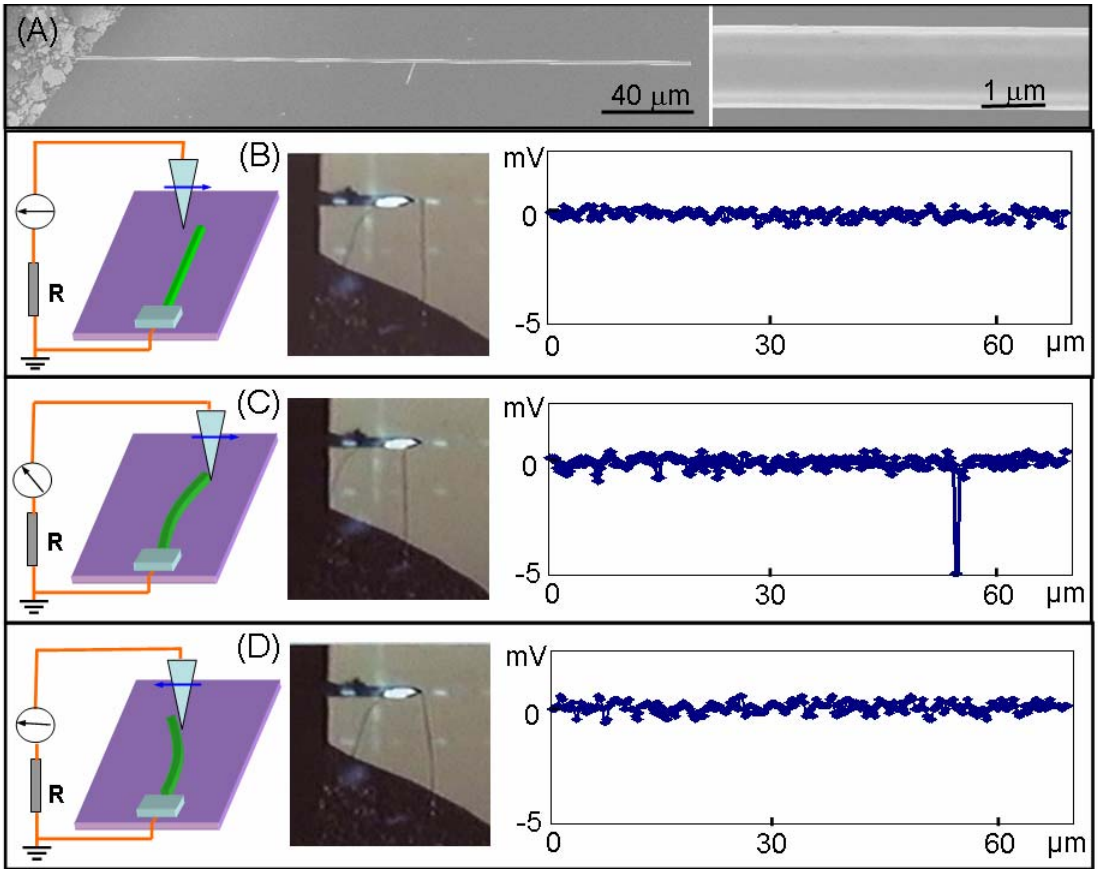

Figure 4.20 In-situ observation of the process for converting mechanical energy into electric energy by a piezoelectric ZnO belt. (**A**) SEM images of a ZnO belt with one end affixed by silver paste onto a silicon substrate and the other end is free. The belt has a rectangular cross-section. (**B, C** and **D**) Three characteristic snapshots and the corresponding topography (red curve) and output voltage (blue curve) images when the tip scanned across the middle section of the belt. The schematic illustration of the experimental condition is shown at the left-hand side, with the scanning direction of the tip indicated by an arrowhead. The scanning speed of the AFM tip was 105.57 μm/s and the sampling density is 256 per line. In (**B**), the AFM tip pushed the belt towards the right-hand side but did not go above and across its width, as judged from the topography image, no output voltage was detected. In (**C**), the AFM tip pushed the belt towards the right-hand side and went above and across its width, as judged from the peak in the topography image, the output voltage image showed a sharp negative peak. There is a

delay in the output voltage peak in reference to the normal force image (the peak in the topography image). In (**D**), for an alternative belt, the AFM tip pushes the belt towards the left but did not go above and across its width, as judged from the topography image, no output voltage was detected beyond noise level although the deflection was large.

The observation for a large belt is given in Fig. 4.20. The SEM images clearly display the rectangular cross-section of the belt (Fig. 4.20A). In this experiment, we selected a strong belt and used an AFM tip to push perpendicular to the belt at its middle section. When subjecting to a displacement force, one side of the belt is stretched (left-hand-side), and the other side (the right-hand side) is compressed. The objective of this experiment is to observe if the piezoelectric discharge occurs when the tip touches either the stretched side or the compressed side, or both sides. The topography image directly captured if the tip passed over the belt or not because it was a representation of the normal force received by the cantilever. When the tip pushed the wire but did not go over and across it, as judged by the flat output signal in the topography image (Fig. 4.20B), no voltage output was produced, indicating the stretched side produced no piezoelectric discharge event. Once the tip went over the belt and in touch with the compressed side, as indicated by a peak in the topography image, a sharp voltage output peak is observed (Fig. 4.20C). By analyzing the positions of the peaks observed in the topography image and the output voltage image, we noticed that the discharge occurred after the tip nearly finishing across the wire. This clearly indicates that the compressed side was responsible for producing the negative piezoelectric discharge voltage. For another belt, when the tip retracted from the right-hand side to the left-hand side (Fig. 4.20D), no output voltage was detected because the tip just touched the stretched side of the belt without across it.

4.2.2 Summary of the Experimental Observation

There are three key results in the experimental observation. First, piezoelectric discharge is observed for both wire and belt, and it may occur only when the AFM tip touches the end of the bent wire/belt. Second, the piezoelectric discharge occurs only when the AFM tip touches the compressed side of the wire/belt, and there is no voltage output if the tip touches the stretched side of the wire/belt. Third, the piezoelectric discharge gives negative output voltage as measured from the load R_L. Finally, in reference to the topography image, the voltage output event occurs when the AFM tip is about finishing across the width of the wire/belt, which means that the discharge event is delayed to the last half of the contact between the tip and the wire/belt.

In order to explain the observed phenomena, we now examine the potential distribution in the wire/belt based on piezoelectric induced potential distribution. Our discussion is for illustrating the physics process and principle rather than a rigorous numerical calculation. We simply considering the polarization introduced in a belt as a result of elastic deformation. The relationship between strain (ε) and the local piezo-electric field (E) is given by $\varepsilon = dE$, where d is the piezoelectric coefficient. For a belt of thickness T and length L as shown in Fig. 3A, under the displacement of an external force F from the AFM tip applied perpendicularly at the top of the belt (z = L), a strain field in the belt would be formed.

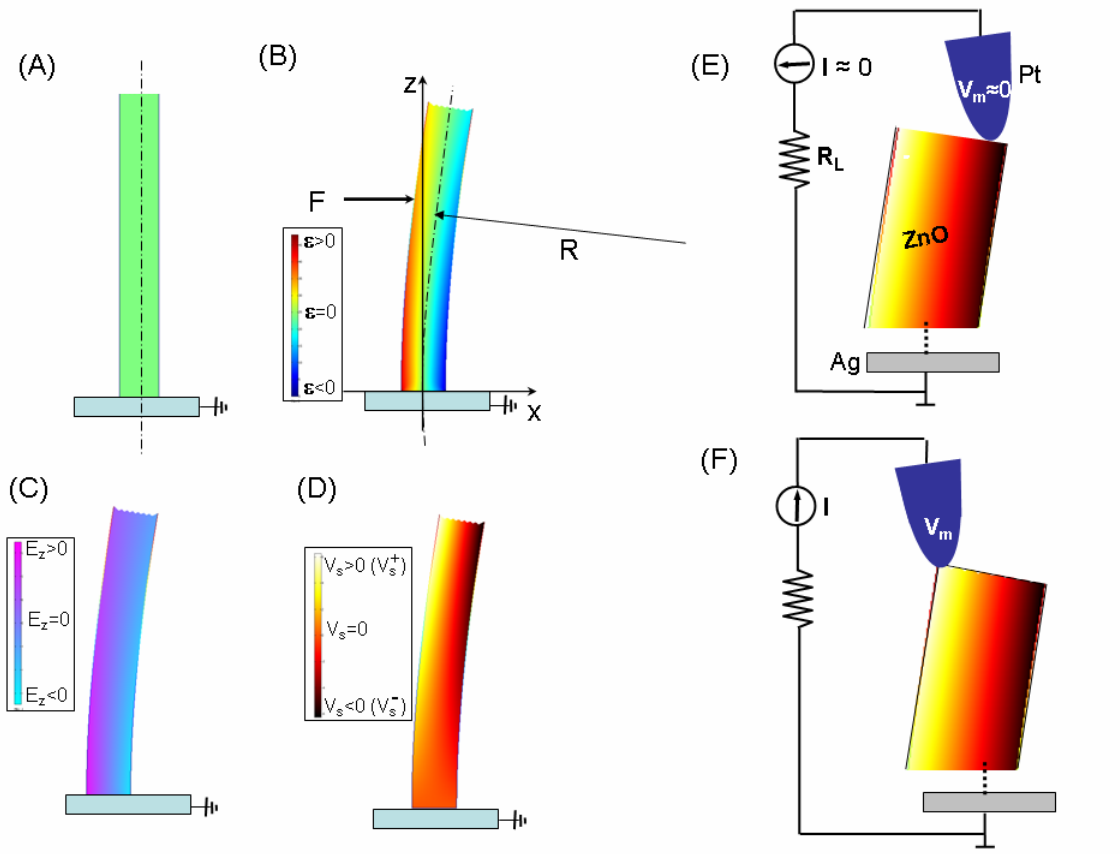

Figure 4.21 Working mechanism for the power generation process of a piezoelectric ZnO wire/belt as a result of coupled piezoelectric and semiconducting properties in conjunction with the Schottky barrier at the AFM tip-semiconductor interface. (**A**) Schematic definition of a belt. (**B**) Longitudinal strain ε_z distribution in the belt after being deflected by an AFM tip from the side. (**C**) The corresponding longitudinal piezoelectric induced electric field E_z distribution in the belt with. (**D**) Potential distribution in the belt as a result of piezoelectric effect, with the stretched and compressed side surfaces being positive and negative potentials, respectively. (**E, F**) Metal and semiconductor contacts between the AFM tip and the semiconductor ZnO belt at two reversed local contact potentials (positive and negative), showing reverse and forward biased Schottky rectifying behavior, respectively. It is this oppositely biased Schottky barrier at the tip-belt interface makes it possible to preserve the piezoelectric charges and later produce the discharge output. The one-way switching role played by the

Schottky diode is important for our observation of the piezoelectric output. The process in (E) is to build up and preserve the charges/potential; the process in (F) is to discharge the potential through a flow of electrons from the circuit. The negative output voltage on the load is a result of current flow from the AFM tip through the ZnO belt to the ground.

For any segment of the belt along its length, the local bending is described by its local curvature 1/*R*, R is the local radius for describing the bending of the belt, which is related to the shape of the belt by $\frac{1}{R} = \frac{d^2y}{dz^2}$ (see Fig. 4.21B). The shape of the belt can be described by the static deflection equation of the belt: $\frac{d^2y}{dz^2} = \frac{F \cdot (L - z)}{YI}$, where *Y* is the elastic modulus of the belt and *I* is its momentum of inertia. The local strain in the belt is $\varepsilon = y / R$, and the corresponding electric field along z-axis is (Fig. 4.21C) $E_z = \frac{\varepsilon}{d} = \frac{y}{d \cdot R}$. This is the electric field that dominates the potential distribution under small bending approximation and the ignorance of the electric field effect on local strain via the piezoelectric effect. For simplicity of analytical calculation to illustrate the physical principle, we consider the potential at the two side surfaces $y = \pm T/2$ by integrating the electric field along the entire length of the belt:

$$V^{\pm} = \int E \cdot ds = \pm \int \frac{T}{2d} \cdot \frac{1}{R} \cdot ds = \pm \frac{T}{2d} \cdot \int d\theta = \pm \frac{a}{d} \cdot \theta_{\max}$$

where $\theta_{\max}$ is the maximum deflection angle at the top of the wire. Then, we have

$$V^{\pm} = \pm \frac{TFL^2}{4dYI}$$

Using the relationship between the maximum deflection y_m and the applied force: $F = \frac{3YIy_m}{L^3}$, we have the potential induced by piezoelectric effect at the stretched and compressed side surfaces, respectively, being:

$$V^{\pm} = \pm 3Ty_m / 4Ld$$

The detail principles see section 4.1.

For the purpose of proposing the mechanism for the piezoelectric generator, we now examine the electric contact in the measurement system we have designed. For the wire/belt used in the measurements, the contacts at the top and the root are non-symmetric. At the top of the wire, since the workfunction of Pt is 6.1 eV and the electron affinity of ZnO is 4.5 eV[102], the Pt-ZnO contact is Schottky[103]. The contact at the bottom is ZnO with silver paste. Since the electron affinity of ZnO is 4.5 eV[14] and the workfunction of Ag is 4.26 eV[104], there is no barrier at the interface, thus, the contact between ZnO and Ag is likely to be Ohmic. To verify this expected result, we have done the following experiment. If we use the silver paste to connect both ends of a wire, the current that flowed through the system was rather high and the IV curve shows anti-symmetry, indicating that the entire system has the Ohmic contact characteristic (Fig. 4A).

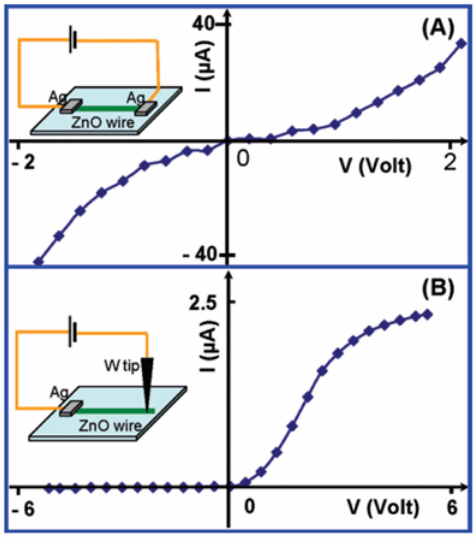

Figure 4.22 Experiments to verify that the contact between silver paste with ZnO wire/belt is Ohmic. (**A**) I-V characteristic of a ZnO wire with both ends in contact with silver paste. (**B**) I-V characteristic of a ZnO wire with one end in contact with silver paste and the other end with tungsten tip.

This is possible only if the contact between Ag and ZnO is Ohmic. Alternatively, if one end is in contact a tungsten tip and the other end is with Ag, the I-V characteristic of the system is Schottky (Fig. 4.22B). This is apparent because the W-ZnO contact is Schottky. Therefore, the transport property of the experimental set up as shown in Figs. 4.19 and 4.20 is governed by the Schottky contact at the interface between the AFM Pt tip and ZnO wire/belt.

We now examine the contact between the AFM conductive tip with the stretched and compressed side surfaces of the belt. As discussed above, the compressed side of the semiconductor ZnO wire/belt has negative potential V^- and the stretched side has positive potential (V^+). This is the cause of the two distinct transport processes across the Schottky barrier at the interface, as described below. When the tip contacts the stretched side surface, the Pt metal tip has a potential of nearly zero, $V_m = 0$, the metal tip - belt interface is negatively biased for $V = V_m - V^+ < 0$. With consideration the n-type semiconductor characteristic of the as-synthesized ZnO belt, the Pt metal- ZnO semiconductor (M-S) interface in this case is a reversely biased Schottky diode (Fig. 4.21E), resulting in little current flowing across the interface. In this case, the piezoelectric static charges, mainly due to Zn^{2+} and O^{2-} ions, are accumulated and preserved, but without creating a current flow through the belt. This is a key process that prevents the slow "leakage" of the current as the deformation is being built up by the tip, otherwise, no observable output electric signal in the next step. As the tip continues to scan and touches the compressed side of the belt (Fig. 4.21F), the metal tip - belt interface is positively biased for $V = V_L = V_m - V^- > 0$. The interface is thus a positively biased Schottky diode, and it is possible to have current flow from the tip through the belt. The flow of electrons is to neutralize the piezoelectric ionic charges distributed in volume, resulting in a sudden increase in the output electric current. The output voltage measured

on the load is negative in reference to the grounded root of the belt with consideration the flowing direction of the current.

The elastic deformation energy as created by the displacement force *F* is mainly dissipated in three ways: creating mechanical resonance/vibration after releasing the belt (as schematically shown in Fig. 4.23A), generating piezoelectric discharge energy for each cycle of the vibration, and overcoming the friction/viscosity, if any, from the environmental and substrate.

The mechanical resonance of the belt continues for many cycles, but it is eventually damped by the viscosity of the medium. The piezoelectric voltage output is generated in each cycle of the vibration, but the AFM tip in the current experimental design may be too slow to collect the electric signal output from each cycle of the belt vibration. In our experiment, we have found that the discharge signal can sometime be collected for an extensive period of time, during which the belt may have resonated for over 10 cycles, as shown in Fig. 4.23A, producing a continuous and constant output DC voltage. The resonance frequency of the wire was ~ 10 kHz, and the scanning speed of the tip was ~ 10 μm/s, it is very feasible that the wire had contacted the AFM forover 100 times before it departed too far to be in touch. The corresponding optical image of the belt shows a blurred trace, which is an indication of many cycles of vibration of the belt.

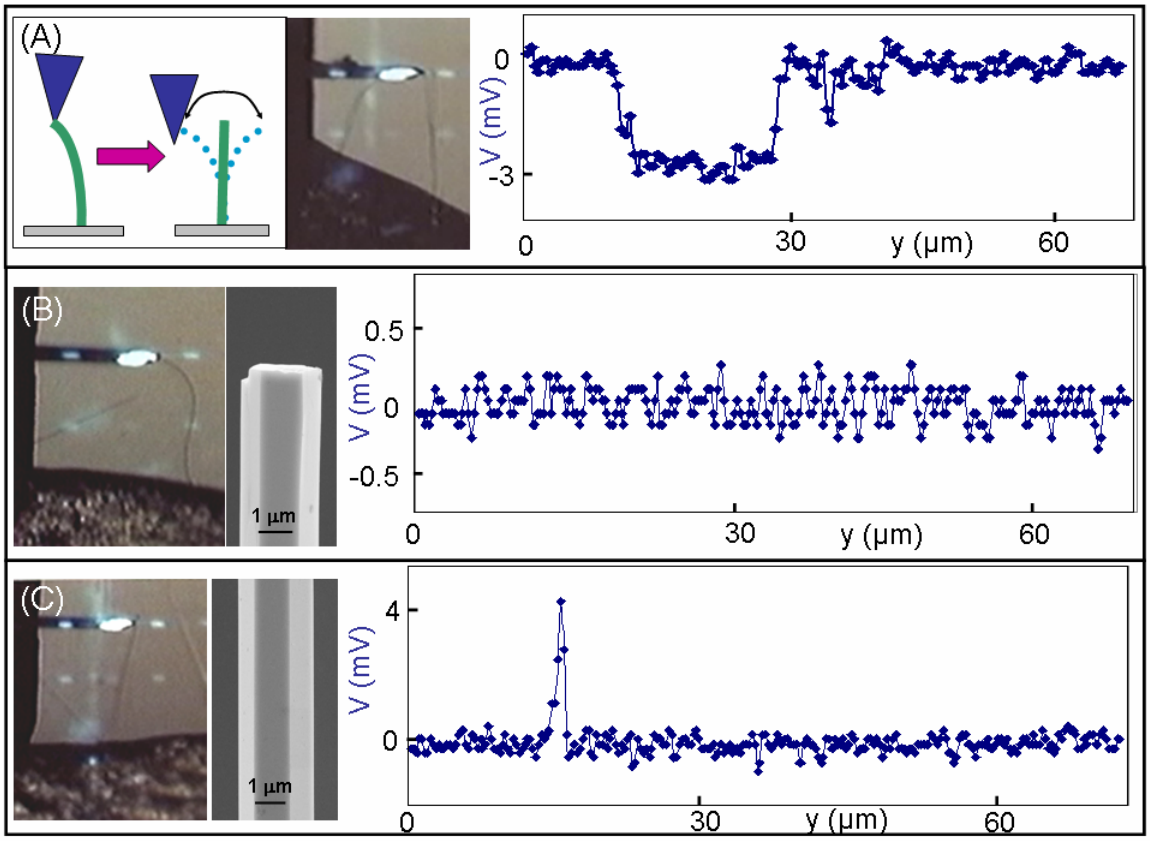

Figure 4.23 Three occasionally observed phenomena in the AFM manipulation of a ZnO wire/wire, showing some unique characteristics for the power generator that may be missed in most of cases due to the slow response of the AFM tip in scanning speed and data output rates. (**A**) Schematic of the resonance vibration of a wire after being released by the AFM tip, showing that the stored elastic energy is transferred mainly into vibration energy after creating the piezoelectric discharge event. But piezoelectric power is generated in each cycle of the vibration. The output voltage image in the right-hand side with a flat and wide plateau is a result of continuous collection of the output voltage from the over 10 cycles of the wire vibration. (**B**) A largely bent wire and its corresponding SEM image, but with no output voltage signal. (**C**) A bent wire, its corresponding SEM image and a positive output voltage peak at the very beginning of the AFM deformation, possibly corresponding to a breakdown of the Schottky barrier at the tip-wire interface due to a larger local potential. This phenomenon was rare to be observed.

This observation unambiguously shows that the piezoelectric output voltage is created in each cycle of the vibration. If we can find a way to continuously collect the output voltage, we simply could have a DC power source.

As illustrated in Fig. 4.21D, there is current flow only when the AFM tip is in contact with the compressed side of the belt/wire. If the AFM tip contacts the stretched side, no output current is possible even under extremely large elastic deformation. This expected result is observed experimentally as shown in Fig. 4.23B, where a ZnO wire is subjected to a large deformation, but no output voltage is received.

As presented for most of the experimental observations, the output voltage is always negative in reference to the grounded root of the wire/belt. We did, however, have a couple of occasions that a positive output voltage was observed at the very beginning when the tip contacted the wire from above (Fig. 5C), but it quickly disappeared for the subsequent scans, and the later measurements showed only negative output voltage peaks. We suspect that the positive voltage peak may be produced by the breakdown of the Schottky barrier under high local piezoelectric voltage when the tip contacted the stretched side of the wire. It must be pointed out that such a phenomenon was observed only a couple of times among the over 20 experiments we have done.

4.3 Introduction of New Field: Nano-Piezotronics

Semiconducting and piezoelectric nanostructures have exciting application in electronics, optoelectronics, sensors, et al.. The nanogenerator introduced in last section (4.1) built the basis of a brand new research field: nano-piezotronics, which could be defined as piezoelectric-semiconducting coupled property for fabricating novel and unique electronic devices and components. In this section, the piezoelectric field-effect transistor based on ZnO nanowire/belt will be illustrated as a sample of nano-piezotronics[105].

4.2.1 Piezoelectric Field-effect Transistor

Field-effect transistors based on nanowirers are most attractive nanodevices. A typical nanowire transistor is composed of a semiconducting nanowire connected at ends by two electrodes and placed on a silicon substrate covered by a layer of oxide. The silicon substrate acts as the gate electrode, which could be build on the top or bottom of the nanowire. The signal output from the drain electrode of the nanowire is controlled by a gate voltage applied on the gate electrode and the nanowire.

A sensor can be fabricated from a source-drain structured nanowire field-effect transistor without the gate electrode. Due to this special design, a large portion of the nanowire is exposed to the environment, which causes the sensing ability of sensing gases, biomolecules, and even virus due to the creation of a charge depletion zone in the semiconductor nanowire by surface adsorbed targets[106].

A sensor can be fabricated from a source-drain structured NW FET without a gate. Thus, a large portion of the NW is exposed to the environment. The mechanism for sensing gases, biomolecules, and even viruses relies on the creation of a charge depletion zone in the semiconductor NW by surface-adsorbed targets17. By connecting a ZnO NW across two electrodes that can apply a bending force to the NW, the piezoelectric field created across the bent NW serves as the gate for controlling the electric current flowing through the NW. This piezoelectric FET can be considered as a new type of transistor that is turned on/off by applying a mechanical force. As a result, it can act as a force sensor capable of measuring forces in the nanonewton range and smaller. The experimental setup is shown in Figure 4.23a. W metal electrodes form ohmic contacts with the ZnO NW. A force is applied to one of the movable electrodes by an external piezoelectric actuator, bending the NW. During this process, the *I-V* characteristics of the device are monitored continuously. Five typical bending curvatures of the ZnO NW are shown in SEM images in Figure 4.23a-e, and their corresponding *I-V* curves are presented in Figure 4.23f. The symmetric shape of the *I-V* curves indicates good ohmic contacts at both ends of the NW19. The current drops significantly with increased bending (curves b-e in Figure

4.23f), indicating decreased conductance with increased strain.

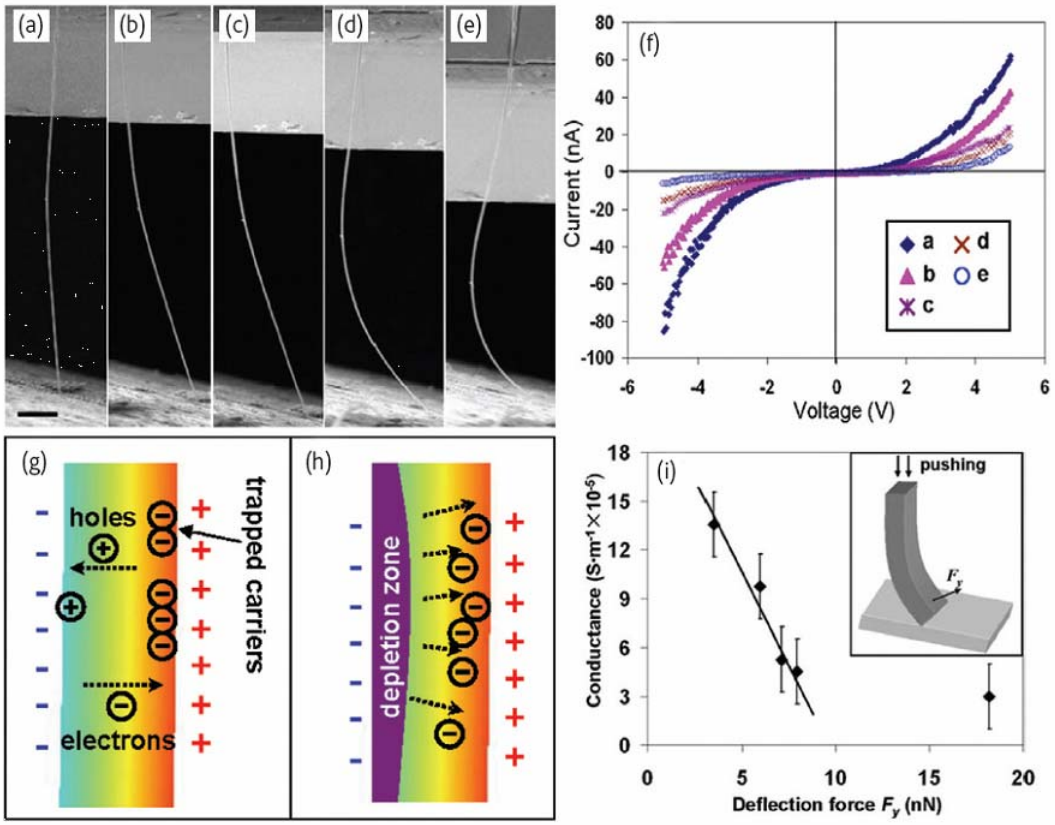

Figure 4.24 (a-e) SEM images showing five different examples of bends introduced into a ZnO NW. Scale bar = 10 μm. (f) Corresponding I-V characteristics of the ZnONW for the five different bending cases. Schematics showing the mechanisms responsible to the conductance change: (g) the carrier trapping effect; and (h) thecreation of a charge depletion zone. (i) Plot showing the relationship between the ZnO NW conductance and the deflection force derived from the experimentaldata, demonstrating a nanoscale force or pressure sensor using a single NW. Inset: schematic of the deflected NW.

A possible mechanism has been proposed to explain the observed phenomenon. First, it is worth examining the coupling between the piezoelectric and semiconducting properties. In 1970, a 75% decrease in in-plane conductance of a semiconducting Si slab was observed when it was sandwiched between two pieces of piezoelectric

leadzirconium-titania (PZT) crystal and the assembly excited by application of an ac signal across its cross section[107]. The drop in Si conductance in the direction orthogonal to the propagation of the elastic wave in PZT was attributed to the trapping of free carriers at the surfaces of the Si plate. This is a result of coupling between the semiconductor Si crystal and the PZT piezoelectric crystal. The coupling effect can now be achieved in a single ZnO NW because of its dual semiconducting and piezoelectric properties. As shown in Figure 4.24, a bent ZnO NW can have positively and negatively charged surfaces at the outer and inner bending arcs of the NW, respectively, because of the stretching and compression of the surfaces. The charges are induced by the piezoelectric effect and are static and nonmobile ionic charges. Upon build up of the electric field, two possible effects can be proposed to account for the reduction of the NW conductance: a carrier trapping effect and the creation of a charge depletion zone.When a piezo-potential is induced across a bent NW, some free electrons in the *n*-type ZnO NW may be trapped at the positive, outer surface, thus lowering the effective carrier density in the NW (Figure 4.24g). Although the positive potential could be partially neutralized by the trapped electrons, the negative potential would remain unchanged. Hence, the piezoelectric field is retained across the width of the NW. This situation can be compared to the case of applying a gate voltage across the diameter of the ZnO NW, as in a typical NW FET. Free electrons will be repelled by the negative potential and form a charge depletion zone around the compressed side, as shown in Figure 4.24h. Consequently, with NW bending, the width of the conducting channel in the ZnO NW becomes smaller and smaller, while the depletion region becomes larger and larger. The depletion zone can develop up to the strain-free plane as a maximum (close to central axis of the NW), considering the piezoelectric field that naturally sets an upper limit to the effect contributed by the depletion charges. The two effects presented in Figure 4.24g and h are likely to contribute to the dramatic drop in the conductance of the ZnO NW with an increase in bending. Based on the principle of the piezoelectric FET, a nanoscale

force/pressure sensor can be demonstrated. The mechanical force applied to the NW can be determined from its bent shape. Thus, a force sensor is established that can measure tiny forces in the nanoNewton range (Figure 4.24i).

There are a lot more nanodevices have been fabricated by using nano-piezotronics, such as nano-piezoelectric-gated diode[108], nano-piezoelectric-resonator, et al..

CHAPTER 5

DC NANOGENERATOR DRIVEN BY ULTRASONIC WAVE

Chapter 4 has demonstrated an innovative approach for converting nano-scale mechanical energy into electric energy by piezoelectric zinc oxide (ZnO) nanowire (NW) arrays[109]. By deflecting the aligned NWs using a conductive atomic force microscopy (AFM) tip in contact mode, the energy that was first created by the deflection force and later converted into electricity using piezoelectric effect has been measured for demonstrating nano-scale power generator. Although this approach has explored the principle and potential of the nanogenerator, for practical applications, we must make innovative design to drastically improve the performance of the nanogenerator in following aspects. First, we must eliminate the use of AFM for making mechanical deformation of the NWs so that the power generation can be achieved by an adaptable, portable and cost-effective approach over a larger scale. Secondly, all of the NWs are required to generate electricity continuously and simultaneously, and all of the electricity can be effectively collected and output. Finally, the energy to be converted into electricity has to be provided in a form of wave/vibration from the environment, so that the nanogenerator can operate "independently" and wirelessly. This paper shows an innovative approach that uses ultrasonic wave to drive the nanogenerator built from an array of vertically aligned ZnO NWs. The design is simple and cost effective and has the potential to meet the requirements outlined above. The approach could be the foundation for optimizing and improving the performance of nanogenerator for its practical applications in nanotechnology.

5.1 First Prototype DC Nanogenerator Driven by Ultrasonic Wave

5.1.1 Fabrication of DC Nanogenerator

The experimental set up is schematically shown in Fig. 5.1A[110], in which an array of aligned ZnO NWs is covered by a zig-zag Si electrode coated with Pt. The Pt coating is not only for enhancing the conductivity of the electrode but also creating a Schottky contact at the interface with ZnO.

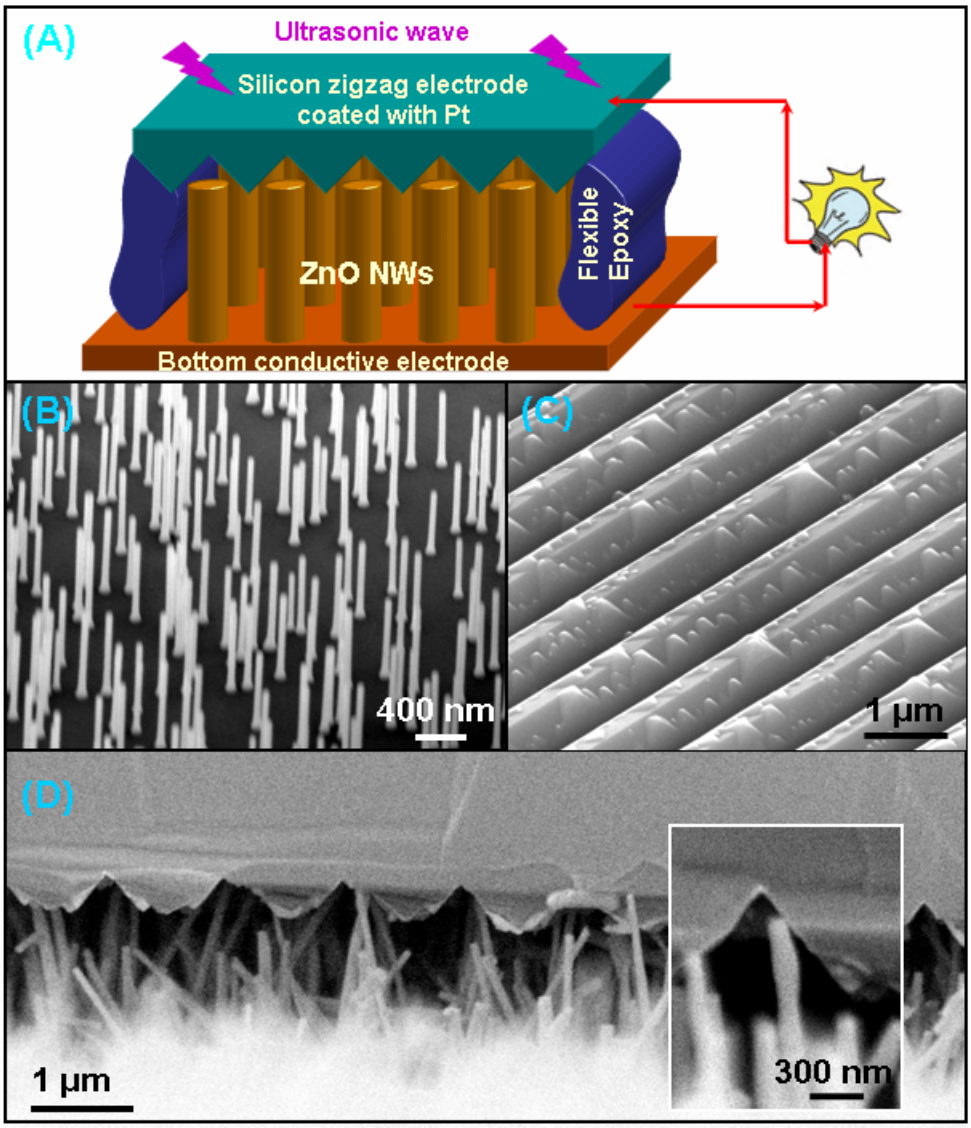

Figure 5.1 Nanogenerators driven by ultrasonic wave. (**A**) Schematic diagram showing the design and structure of the nanogenertor. Aligned ZnO NWs grown on a solid/polymer substrate are covered by a zig-zag electrode. The substrate and the electrode are directly connected to an external load. (**B**) Aligned ZnO NWs grown on a GaN substrate. The gold catalyst particles used for the growth had been mostly vaporized, thus, the final NWs are purely ZnO with flat top ends.

(**C**) The zig-zag trenched electrode fabricated by standard etching technique. (**D**) A cross-section SEM image of the nanogenerator composed of aligned NWs and the zig-zag electrode. The inset shows a typical NW that is forced by the electrode to bend, resulting in output of electricity once touches the left-hand adjacent tooth.

The NWs were grown on GaN substrates that are covered by a thin layer of ZnO film (Fig. 5.1B), which serves as a common electrode for direct connecting with the external circuit. The density of the NWs is ~ 20/μm^2, with heights ~ 1.5 μm and diameter ~ 40 nm. The top electrode is composed of parallel trenches fabricated on a (001) orientated Si wafer [111] and coated with a thin layer of Pt (~200 nm) (Fig. 5.1C). Then the electrode was placed above the NW arrays with a small gap, which was fixed and packaged by flexible epoxy. A cross-section image of the packaged NW arrays is shown in Fig. 5.1D, displaying a "lip-teeth" relationship between the NWs and the electrode. Some NWs are in direct contact with the top electrode, but some are located between the teeth of the electrode. The electricity produced by the relative deflection/displacement between the NWs and the electrode via either vibration and/or the resonance is expected to be output simultaneously and continuously. The packaged device was supported by a metal plate, which was directly in contact with the water contained in the cavity of an ultrasonic generator. The operation frequency of the ultrasonic wave was ~41 KHz. The output current and voltage were measured by an external circuit at room temperature.

5.1.2 The Mechanism of DC Nanogenerator

The design is based on the physical principle of the nanogenerator reported previously [99,109], which relies on a unique coupling between piezoelectric and semiconducting properties of the aligned ZnO NWs. This is also the fundamental physical principle of nano-piezotronics[112] including piezoelectric-field effect transistor and diode[113]. The asymmetric piezoelectric-potential across the width of a ZnO NW and the Schottky contact between the metal electrode and the NW are the two key processes for

creating, separating, preserving/accumulating, and outputting the charges. A top electrode is designed to achieve the coupling process and to replace the role of AFM. The role of the zig-zag trenches is to act as an array of parallel packed AFM tips (Fig. 5.2A).

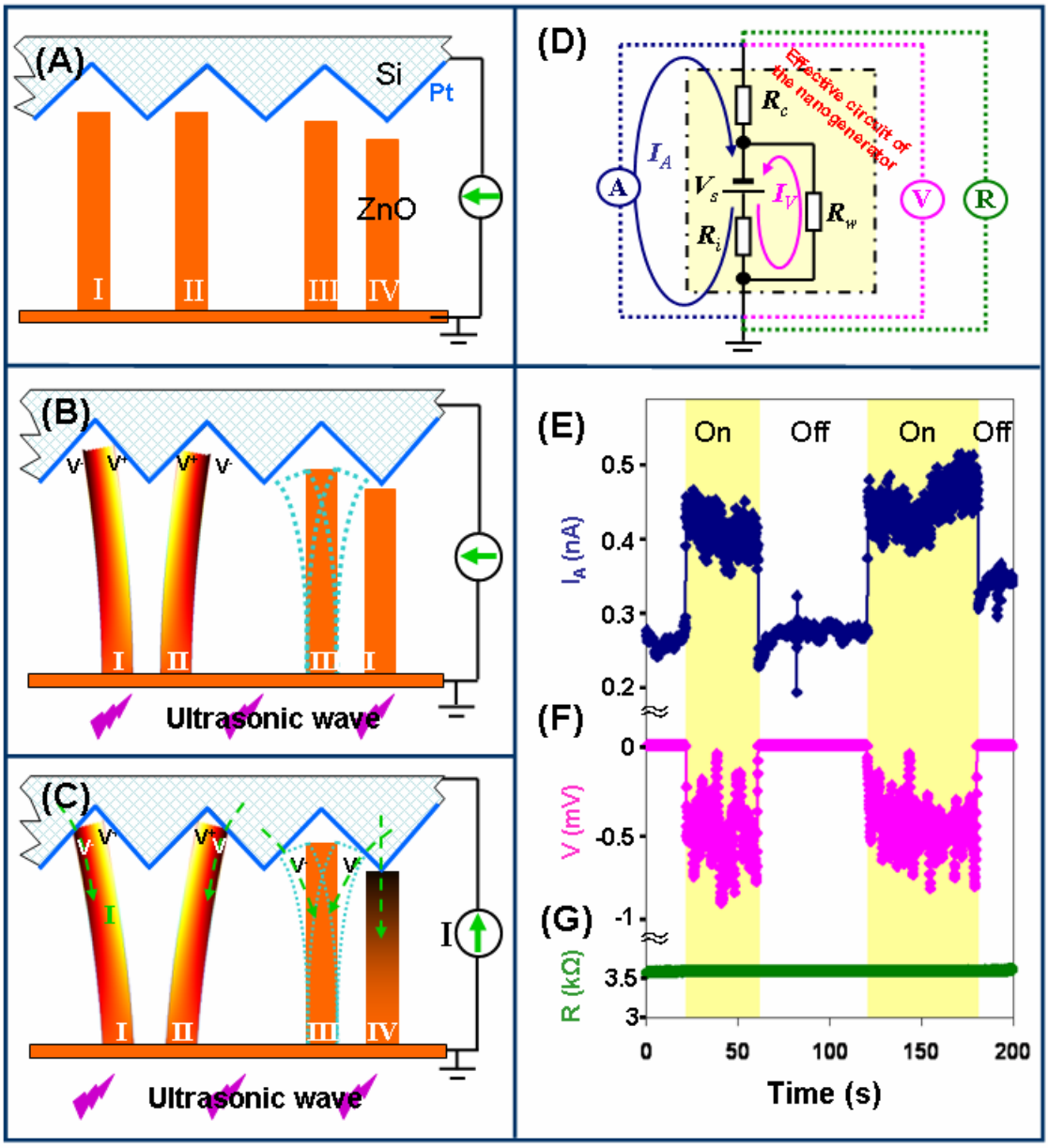

Figure 5.2 The mechanism of the nanogenerator driven by ultrasonice wave. (**A**) Schematic illustration of the zig-zag electrode and the four types of representing configurations of the NWs. (**B**) The piezoelectric potential created across the NW I and II

under the push/deflection of the electrode as driven by the ultrasonic wave, but without flow of current due to the reversely biased Schottky diode at the electrode-NW interface. The NW III is in resonance under the stimulation of the ultrasonic wave. (**C**) Once the NWs touche the surface of the adjacent teeth, the Schottky diode at the electrode-NW interface is forward biased, piezoelectric discharge occurs, resulting in the observation of current flow in the external circuit. (**D**) The effective circuit of the nanogenerator and the set up for measuring the output current I, output voltage V and the resistance R (see text). (**E, F, G**) Measured output current I, output voltage V and the resistance R using the connections shown in (D), respectively, when the ultrasonic wave was turned on and off periodically. A pixel averaging was applied to reduce the noise.

We now take NW I as an example to illustrate the process of outputting piezoelectric energy generated in each cycle of the NW bending/deflection. When subjecting to the excitation of ultrasonic wave, the zig-zag electrode could move down to push the NW, which leads to a lateral deflection of the NW I, creating a strain field across NW width, with the NW outer surface being in tensile and inner surface in compressive strain. The inversion of strain across the NW results in an inversion of piezoelectric field E_z along the NW, which produces a piezoelectric potential inversion from V^- (negative) to V^+ (positive) across the NW (Fig. 5.2B). When the electrode contacts the stretched surface of the NW, which has a positive piezoelectric potential, the Pt metal- ZnO semiconductor (M-S) interface is a reversely biased Schottky diode, resulting in little current flowing across the interface. This is the process of creating, separating and preserving/accumulating charges. With the further pushing of the electrode, the bent NW I will reach the other side of the adjacent tooth of the zig-zag electrode (Fig. 5.22C). In such a case the electrode is also in contact with the compressed side of the NW, where the M-S interface is a forward biased Schottky diode, resulting in a sudden increase in the

output electric current flowing from the top electrode to the NW. This is the discharge process.

There are several possible configurations for creating piezoelectric driven charge movement. Figure 5.2A-C shows the four possible configurations of contacts between a NW and the zig-zag electrode. In analogous to NW I, the same process applies to the charge output from NW II. NW III is chosen to elaborate the resonance induced by ultrasonic wave. As shown in Fig. 5.2C, when the compressive side of NW III is in contact with the electrode, the same discharge process as for NW I occurs, resulting in the flow of current from the electrode into the NW. For NW IV, which may be short in height, and it is in a compressive strain by the electrode without bending. In such a case, the piezoelectric voltage created at the top of the NW is negative. Thus, across the electrode–ZnO interface, a positively biased Schottky diode is formed; hence, the electrons can freely flow across the interface. As a result, electrons flow from the electrode into the NW as the deformation occurs. This slow discharging process, if significant, may also contribute to the measured current.

An equivalent electric circuit is shown in Fig. 5.22D to understand the measurements and outputs of the nanogenerator. The NWs that are active for producing current in the nanogenerator is equivalent to a voltage source V_s with an inner resistance R_i that also contains the contact resistance between the NWs and the electrode. On the other hand, there are a lot of NWs that are in contact with the electrode but cannot bend or move freely, thus, they do not actively participate in the current generation but they do provide a path for conducting current. These NWs are simply represented by a resistance R_w that is in parallel to the portion that generates power. A resistance R_c is introduced to represent the contact resistance between the electrode and the external measurement circuit. The capacitance in the system is ignored in the circuit for simplifying the discussion about DC measurement.

The current and voltage outputs of the nanogenerator are shown in Fig. 5.2E and F, respectively, with the ultrasonic wave being tuned on and off periodically. A jump of ~0.15 nA is apparent when the ultrasonic wave was turned on, and the current immediately fell back to the base line once the ultrasonic wave was turned off. Correspondingly, the voltage signal exhibited similar on and off tendency but with negative output of ~ - 0.5mV. The negative sign is of voltage is consistent to the mechanism presented in Fig. 5.2C. The signal-to-noise ratio for the current is significantly better than that for the output voltage for the following reason. When the current was measured, since the inner resistance of the current meter (ideally zero) is much much smaller than R_w, the current generated by the nanogenerator would by-pass R_w, and the current path is indicated by the solid blue curve in Fig. 5.2D; the measured current is $I_A = V_s/(R_c + R_i)$. However, for the voltage measurement, since R_w was much much smaller than the inner resistance of a voltage meter (ideally infinity), a loop was formed between the power generating portion and R_w, as shown by the solid pink curve in Fig. 5.2D, and the current is I_V and the measured voltage V is that across the power generating portion, $V = - V_s R_w/(R_i + R_w)$. During the ultrasonic vibration, for the instable contacts between NWs and the electrodes, the measured current I_A is affected by the instability of two factors of V_s and R_i, and the measured voltage V is affected by the instability of three factors of V_s, R_i and R_w, As a result, V has higher noise level than that of I_A, in consistent to the observations displayed in Figs. 5.2C and D. Therefore, the current signal is more reliable to characterize the performance of the DC nanogenerator.

The resistance R of the entire nanogenerator was also measured with and without turning on the ultrasonic wave, as shown in Fig. 5.2G, the resistance remained a very stable regardless if the wave was on or off. This measurement indicates that the change in current was not due to the variation of resistance, confirming that the current signal presented in Fig. 5.2E was truly generated by the nanogenerator itself!

5.1.3 The Performance of DC Nanogenerator

The output electricity of the nanogenerator is sustainable and reasonably stable. By turning the ultrasonic wave on and off, the output current shows good correspondence (Fig. 5.3A). The output current is in the nano-Ampere range. The nanogenerator can work continuously for an extended period of time beyond one hour (Fig. 5.3B). The stability of the current is good.

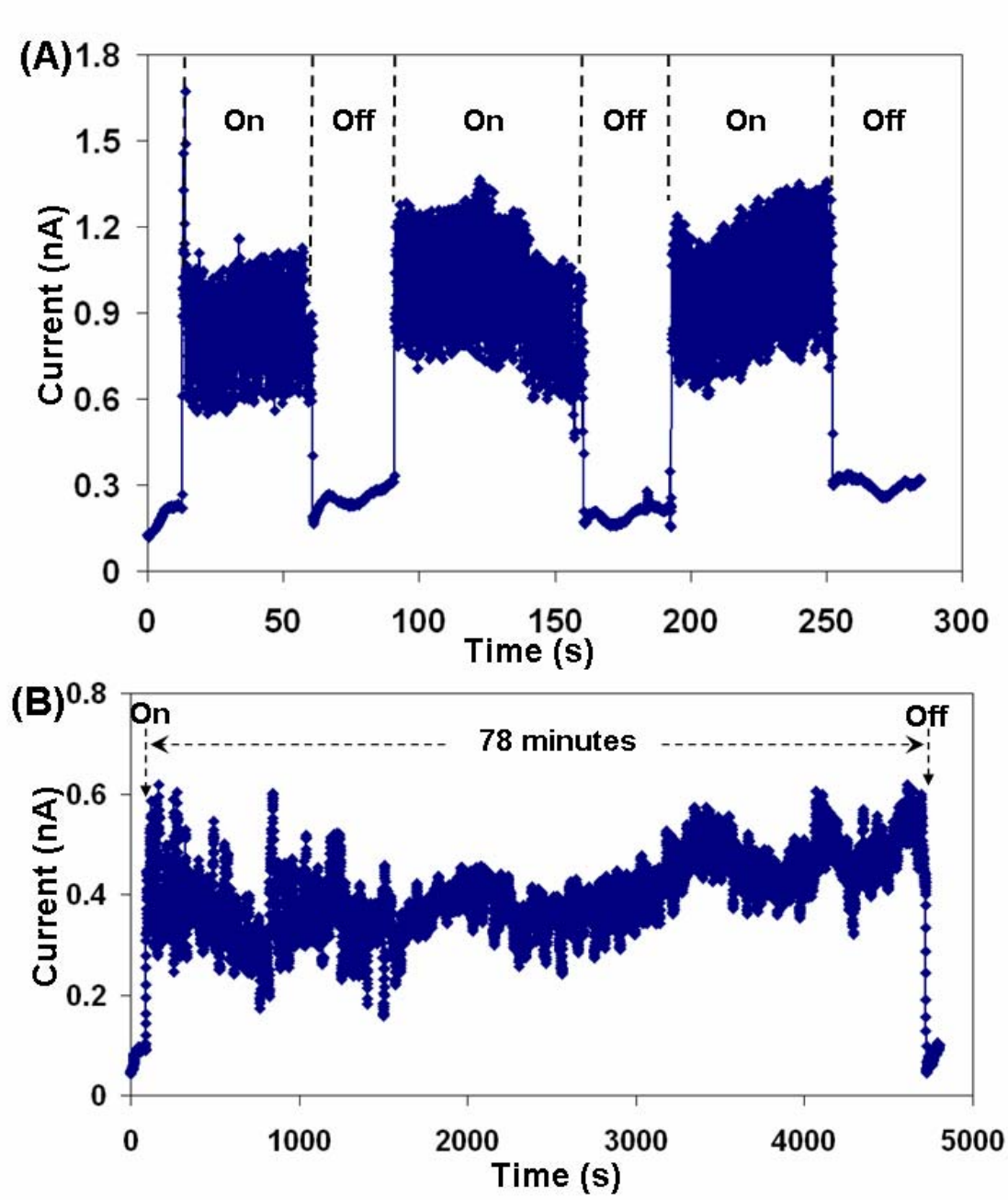

Figure 5.3 Continues DC output of the nanogenerator. (**A**) Reproducible and highly repeatable current output of the nanogenerator when the ultrasonic wave was turned on and off. (**B**) Continuous current output of the nanogenerator for an extended period of time. The data are displayed after correcting the background introduced by electronic drift.

The design as presented in Fig. 5.1 has been tested in comparison to the experiments conducted using different materials or configurations. As presented in Fig. 5.1A, simply by replacing ZnO NW array by an array of carbon nanotubes (CNTs), no output current was observed (Fig. 5.4A).

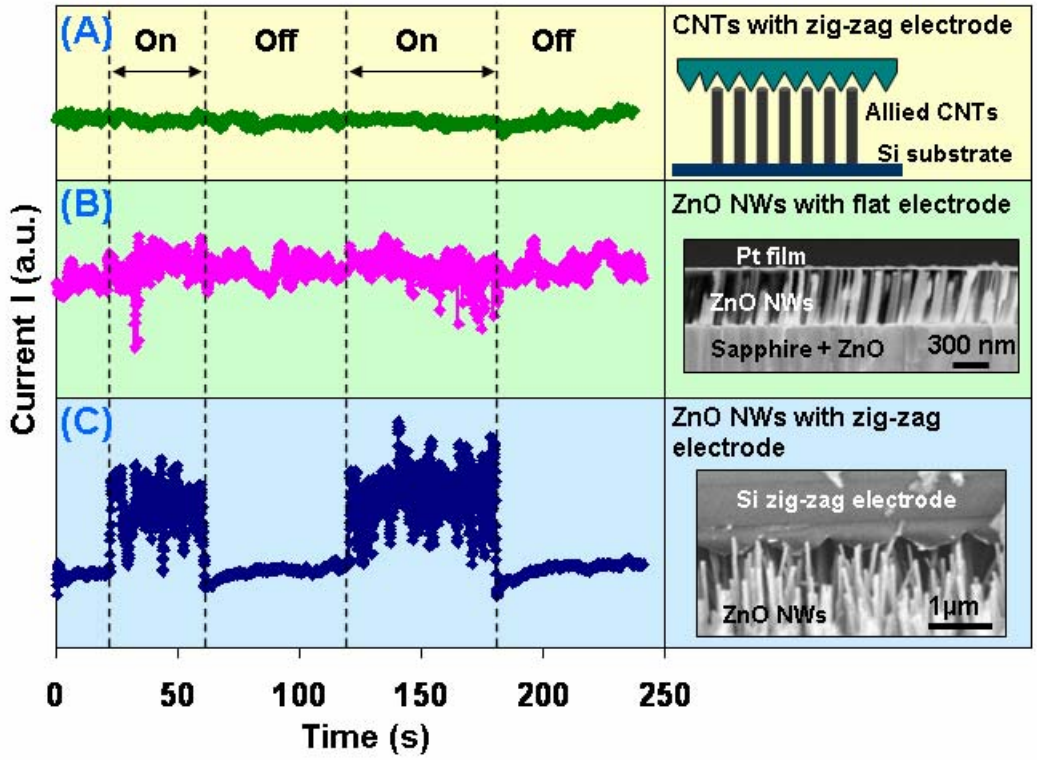

Figure 5.4 Output of the nanogenerator using different materials and different design configurations. (**A**) Nanogenerator based on arrays of carbon nanotubes with a zig-zag top electrode, showing no output current regardless the ultrasonic wave was on or off. (**B**) Nanogenerator based on arrays of ZnO NWs but with flat top electrode, showing no output current while stimulated by ultrasonic wave. (**C**) Nanogenerator based on arrays of ZnO NWs with a zig-zag top electrode, showing detectable output current when the ultrasonic wave was turned on.

This is because that CNT is not piezoelectric. Using ZnO NW array but replace the top electrode with a flat thin Pt film that totally covers the tips of the NWs, as shown in Fig. 5.4B, no output current was observed either. This is because that the design does not follow the mechanism of the nanogenerator. Output was only detected when the top electrode is a zig-zag shape with the use of ZnO NWs (Fig. 5.4C). These experiments rule out the possible contribution from electronic noise of the system and measurement error or artifacts in producing the output current, and they consistently support the process proposed in Fig. 5.2A-C for piezoelectric NWs.

In comparison to the AFM aided nanogenerator illustrated in chapter 4, the design shown in Fig. 5.1A has achieved three major objectives: replacing the use of an expensive and sophisticated AFM tip by ultrasonic wave/vibration for inducing elastic deformation; integrating an array of "tips" into a zig-zag electrode for simultaneous creating and outputting electricity generated by many NWs; and the output DC is fairly stable and continuous. Since the voltages created by all of the NWs are in parallel, the output voltage is effectively the voltage created by one NW. As limited by the smaller degree of ultrasonic wave induced elastic deformation to the NWs as comparison to that induced by an AFM tip, the output voltage is naturally smaller.

The number of NWs that were effective for producing output electricity can be estimated from the output power of the nanogenerator. From our previous study, the NW deformed by AFM produced an energy of $E_{AFM} \sim 0.01$ fJ for each cycle of discharge, which lasted for ~ 0.1 ms; thus, the power generated by one NW was $W_{AFM} \sim 0.1$ pW. In the current experimental design, the vibration amplitude of the NW is much smaller than that of the NW directly deflected by an AFM tip, thus, the output voltage is ~ 1 mV, about 5-10 times smaller than that received using AFM as the deformation tool. In such a case, the output power of a NW as driven by ultrasonic wave is $W_{wave} = (0.001 - 0.004)$ pW. From Fig. 5.2C-D, the output power of the nanogenerator with an area of 2 mm^2 substrate

area is $W_{wave} = IV \approx 1$ pW. Therefore, the number of NWs that were active for producing electricity was $N = W_{wave}/ \ W_{wave} \approx 250 - 1000$. As limited by the multiple contacts between the NWs and the electrode in the current design (see Fig. 5.1D), majority of the NWs did not produce electricity due to their large non-uniformity in height, so that the output current is rather small in the current design. These technical difficulties are likely to be overcome by an optimized design of the nanogenerator, such as using of a regular tip arrays as the electrode, and the designed and patterned growth of high quality uniform NW arrays matching the design of the electrode. If the area taken by each tip is 1 μm x 1 μm, the grown density of NWs is $10^8/cm^2$. If one NW produces ~10 fW of power by optimizing its size and shape, the output power per unit area will be ~ 1 $\mu W/cm^2$. The power used for powering the device made using one NW/nanotube is ~ 2-10 nW. The nanogenerator built using the NWs grown on an area of 1 cm^2 could be effective for powering 100-500 nanodevices.

5.2 Integrated Nanogenerators in Biofluid

In section 5.1 a direct-current nanogenerator that is driven by ultrasonic waves is discussed. The basic principle is to use piezoelectric and semiconducting coupled nanowires (NWs), such as ZnO, to convert mechanical energy into electricity.10,11 This nanogenerator (NG) has the potential of directly convert hydraulic energy in the human body, such as flow of body fluid, blood flow, heart beat, and contraction of blood vessels, into electric energy. Although a prototype of the NG has been demonstrated by indirect driving using ultrasonic waves through a metal frame suspended in air, it is essential to develop nanogenerators that work in water or biofluid. This section presents an improved design of NG that is able to generate electricity in biocompatible fluid as driven by ultrasonic waves. The output current of the NG has been improved by a factor of 30. By integrating several NGs, the potential of improving output voltage and current is demonstrated. This research sets the platform toward threedimensional architectured NGs

as practical power sources.

5.2.1 The Fabrication and Setup

The NG was modified from our original model composed by vertical aligned ZnO NWs and a Pt-coated zigzag top electrode, as described in detail elsewhere.9 The NG core was completely packaged by a polymer to prevent the infiltration of biofluid into the NG. The polymer also has certain flexibility to remain free of relative movement between ZnO NWs and the top of the electrode. As shown in Figure 1a, the NG was placed inside a container filled with 0.9% NaCl solution, which is a typical biocompatible solution. The substrate and the top electrode were connected by waterproof extension cord to the outside of the container and marked as the positive and negative electrode, respectively. The definition of the two electrodes is according to the flow of current in the external circuit, which is always from the bottom substrate to the top zigzag electrode owing to the rectifying effect of the Schottky barrier between ZnO and Pt in the core of the NG.10 An ultrasonic stimulation was applied through the bottom of the container with a frequency of _41 kHz. The ultrasonic wave transported through the fluid and triggered the vibration of the electrode and NWs to generate electricity. For the following studies, the size of the NG was about 2 mm2, on which there are more than one million NWs.

5.2.2 The Performance of The Integrated Nanogenerator

The performance of the NGs was characterized by measuring short circuit current *I*sc and open circuit voltage *V*oc. The output of the NGs is in the nanoampere and millivolt level. Measuring electric signal at such a small scale is always challenging because of system and/or environmental interference, such as system capacitance, thermal/instability drifting, and the bias of the amplifier. Caution must be taken at each step to ensure the signal was generated by the NG instead of the measurement circuits. We found that a “double-side” testing was very effective for ruling out artifacts. As

illustrated in Figure 5.5a, during the measurements, the current/voltage meter was forward connected (positive and negative probes were connected to the positive and negative electrodes, respectively) and reversely connected (positive and negative probes connected to negative and positive electrodes, respectively) to the two electrodes of the NG. The corresponding *I*sc and *V*oc signals are shown in parts b and c of Figure 5.5, respectively. After an ultrasonic wave was switched on, current output peak reached as high as 17 nA, with an average output of ~9 nA and a "noise/instability" within (4 nA (pink line in Figure 5.5b). When the current meter was reversely connected, current signal with the same amplitude was received but reversed in sign (blue line in Figure 1b). This measurement clearly eliminated the effects from measurement system error and confirmed that the current was generated by the NG.

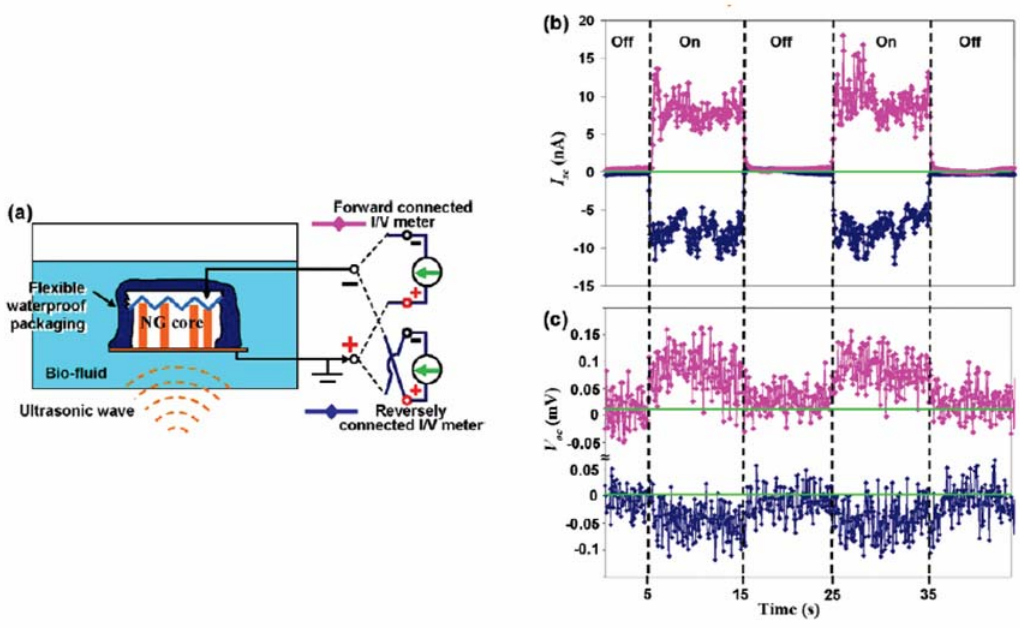

Figure 5.5 (a) Schematic of a NG that operates in biofluid and the two types of

connections used to characterize the performance of the NG. The pink and blue curves represent signals from forward connected current/voltage (*I*/*V*) meter and reversely connected *I*/*V* meter, respectively. (b, c) The short circuit current and open circuit voltage measured by the two types of connections when the ultrasonic wave was turned on and off.

The corresponding voltage output is rather low and noisy compared to the current signal. As shown in Figure 1c, a typical voltage level is ~0.1 mV, and a jump of the signal can still be clearly distinguished from the baseline. The voltage exhibited the same sign as the corresponding current signal, and its sign was reversed while the meter connection was switched. Previous atomic force microscopy (AFM) deflection of a single NW generated a voltage output in the range of 5-10 mV, which is much larger than that of the NG as driven by ultrasonic waves. The low voltage could possibly result from two reasons. First, the bending angle of a NW as deflected by an AFM tip with direct contact was much larger than that produced by an indirect ultrasonic wave. From theoretical calculation, the piezoelectric voltage produced by a NW is proportional to its lateral deflection. Therefore, AFM can generate much higher voltage between the ZnO NW and its tip. Second, although the parallel packaged NW array as shown in Figure 1a gives, in principle, a similar voltage output as a single NW used in AFM deflection, a large difference in capacitance between the two cases may result in much reduced voltage output. The capacitance of the NG shown in Figure 1a was measured to be ~18-22 pf in the frequency range of 75 kHz to 1 MHz, while the capacitance of a single NW and the AFM system used in our previous study was ~1.2 pf.10 More than 97% of the NWs in the NG were not active for producing current but did serve as capacitors for storing changes created by the active NWs (<3%).9 The large capacitance effectively reduces the output voltage. Therefore, the output voltage could be reduced by ~20 times for the NG. This is probably why the output voltage of the NG was ~0.5 mV or even smaller.

5.2.3 The Improvement of the Integrated Nanogenerator

For technological applications, raising the voltage and current outputs of the NG are essential for raising the output power. If we take each NG as a battery, the most straightforward way to increase the current/voltage is to put them in parallel/serial. This has been demonstrated experimentally.

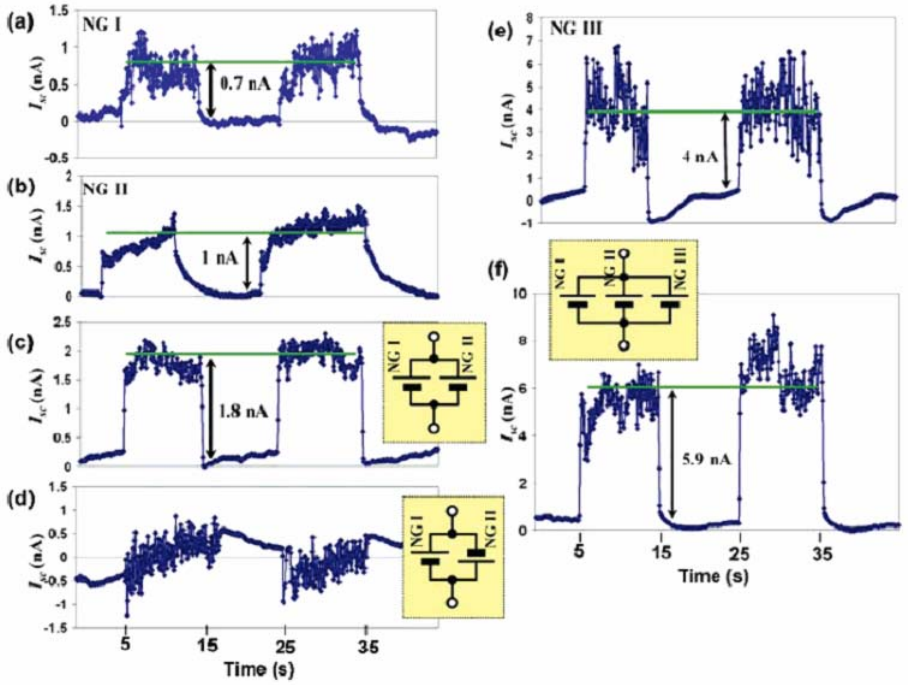

Figure 5.6 Short circuit current measured from an integrated NGs system. (a, b) Current signal measured from two individual NGs, I and II. (c, d) Current signal measured from parallel and antiparallel connected NG I and NG II, respectively; the connection configurations are schematically shown in the insets. (e) Current signal measured from NG III with a better performance. (f) Current signal measured from parallel connected NG I, II, and III; inset shows the connection configuration.

As shown in parts a and b of Figure 5.6, two NGs I and II have been tested under the same experimental conditions. NG I exhibited an average *I*sc of ~0.7 nA, and NG II showed a lower noisy signal of 1 nA. These two NGs were then connected in parallel

(inset of Figure 5.6c) and tested under the same condition again. The resultant output current reached an average of ~1.8 nA, which is the sum of the two individual outputs (Figure 5.6c). This concept was further proved by antiparallel connecting NG I and NG II (inset of Figure 5.6d). Since the magnitudes of the *I*sc of the two NGs were very close, the total current was mostly cancelled out by the "head-to-tail" connection in parallel, and the received signal was around the baseline (Figure 5.6d), just as we expected. If more NWs were located in the activate position when packaging the top zigzag electrode, the output current can be improved by several times. As shown in Figure 5.6e, with a better assembly, NG III exhibited an average *I*sc of ~4 nA. Once NG III was added to the parallel connection with NG I and NG II (inset of Figure 5.6f), their total output current was the sum of the three NGs (5.9 nA ≈0.7 nA + 1 nA +4 nA), as shown in Figure 5.6f. This series of experiments demonstrated that the short circuit current can be effectively improved by parallel connecting multiple NGs. This sets the platform for developing three-dimensionally stacked NGs. Although the voltage signals were much noisy than current, as explained in section 5.1, the increasing trend can still be clearly distinguished when NGs were connected in serial.

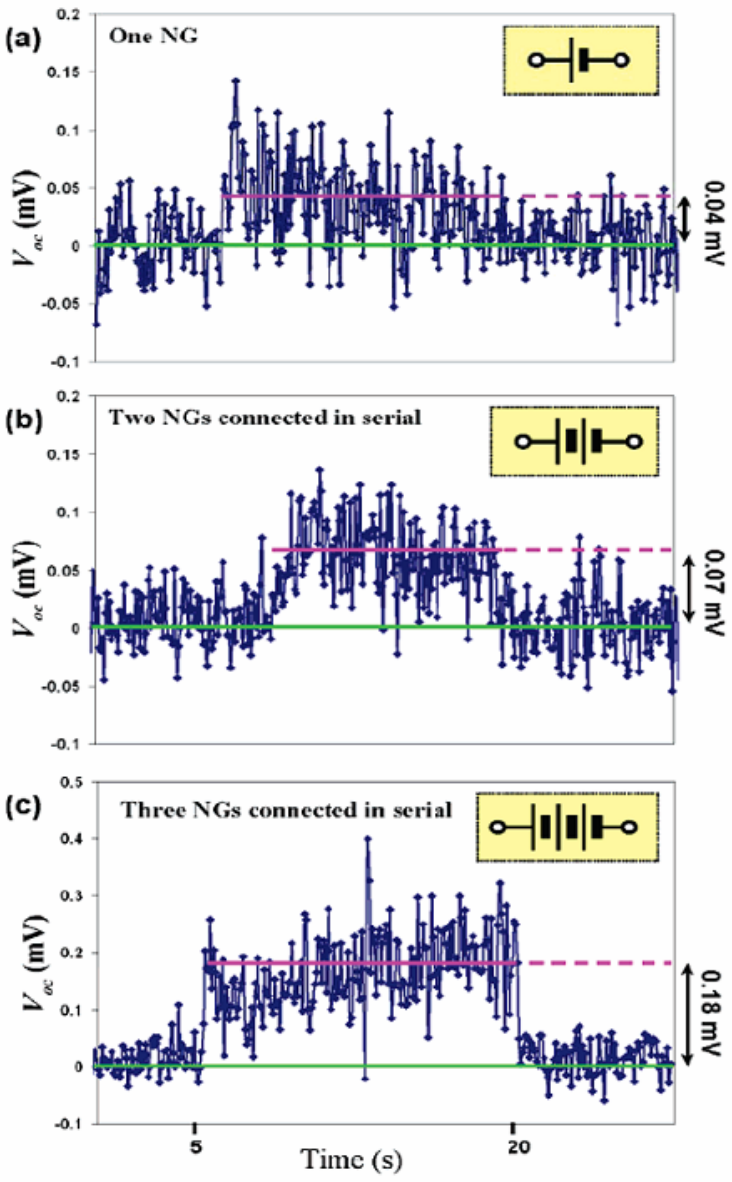

Figure 5.7 Open circuit voltage measured from an integrated NGs system. (a-c) Voltage signal measured from one, two, and three serial connected NGs. The connection configurations are schematically shown in the insets.

As shown in Figure 5.7a, a single NG gave a very noisy voltage output of only ~0.04 mV (NG I). When two similar NGs (I and II) were connected in serial, their output voltage was almost doubled to an average value of 0.07 mV (Figure 5.7b). Once the NG III was added to the serial, the resultant voltage output clearly jumped above the baseline

and reached an average of ~0.18 mV. Therefore, similar to the current output, the open circuit voltage can be effectively improved by connecting multiple NGs in serial. Although the individual voltage output might be low, microfabrication techniques can be used to integrate hundreds of NGs onto one chip or stack them vertically for receiving high output voltage.

5.2.4 The Effect of Ultrasonic Wave Intensity

The local intensity of the ultrasonic wave was important for improving the output of the NG. As schematically shown in Figure 5.8a, the biofluid was placed into a glass container with a diameter of 11 cm and a height of 9.5 cm. The ultrasonic wave source was placed at the center beneath the container.

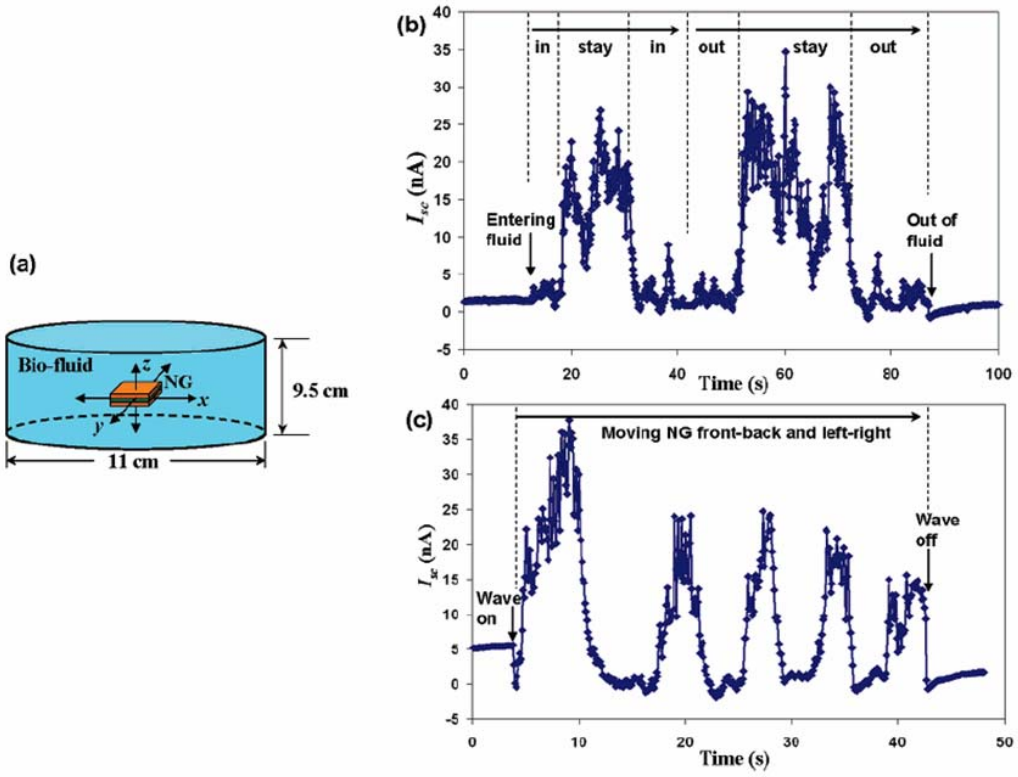

Figure 5.8 Enhanced output power by seeking the strong local intensity of the ultrasonic waves. (a) Schematic of the NG's position and moving directions inside biofluid. (b)

Short circuit current signal measured during the movement of NG along the *z* direction (from water surface to the bottom and then back to surface). (c) Short circuit current signal measured during the movement of NG along the *x* and *y* directions while the *z* position was kept 3.3 cm below the water surface.

Once the ultrasonic wave was excited inside the container, it was reflected by the container's wall and the water surface. As a result, the wave intensity was enhanced in a certain region inside the fluid. A NG was placed inside the fluid and held by a clamp that can be freely moved in any direction to trace the enhanced ultrasonic wave, while the output current was continuously monitored. First, the NG was placed at the center region above the water surface and the ultrasonic wave was kept on. The corresponding current signal is shown in Figure 5.8b. Then the NG was slowly moved into the fluid along the *z* direction (depth direction) and a jump in current for ~1 nA was immediately detected once the NG touched water surface. When the NG reached ~3.3 cm below the water surface, the current quickly jumped to ~20 nA. The output can be kept at such a high level as long as the NG stayed at this depth. After 15 s of steady high output, the NG was moved further down and the current dropped back to the 1-2 nA level again. When the bottom of the container was reached, the NG was pulled upward to the water surface. The same 20-25 nA high current output was observed again once the NG reached 3.3 cm depth. The current signal dropped back to its baseline after the NG was pulled out of water. Then, the NG was kept 3.3 cm below water surface but moving along the *x* and *y* directions. The output current is shown in Figure 4c. Starting at the central region, when the ultrasonic wave was turned on, the current quickly jumped to 25 nA and soon reached the highest peak of 35 nA. Then the NG was slowly moved away from the central region while its vertical position was kept unchanged. The current quickly dropped to ~1 nA when the NG was ~2-3 cm away from the center point. The NG was continuously moved from left to right and from front to back. Only when it passed through the central region

of the container, the high current output of ~20 nA was detected. These two experiments illustrated how the intensity of ultrasonic wave dictated the NG's output. At the center and 3.3 cm inside the fluid, the short circuit current was increased by 20-30 times. This is because the current relies on the number of NWs involved in power generating and the degree of bending of the NWs. It appears that the strong ultrasonic wave was effective for stimulating the output of the NG. The 35 nA achieved here for a nanogenerator with an effective area of 2 mm2 is more than 30 times higher than that obtained in our previous report. The NG has a long lifetime. We have kept the ultrasonic wave on for 4 h without interruption, the NG was sustaining active for generating electricity without stop. We expect the lifetime of the NG is much longer than the time we have tested.

CHAPTER 6

DETAILED INVESTIGATION OF THE PRINCIPLE OF NANOGENERATORS

6.1 Carrier Density and Schottky Barrier with DC Nanogenerator

Using aligned ZnO nanowire (NW) arrays, Chapter 5 has demonstrated a nanogenator (NG) for converting mechanical energy into electricity. The mechanism of the nanogenerator relies on the coupled semiconducting and piezoelectric properties and is composed of two steps. When a clean ZnO nanowire (NW) or nanobelt is bent by an atomic force microscope (AFM) tip, an asymmetric strain is produced across the width of the NW. As a result of piezoelectricity, the stretched side of the NW has a positive potential and its compressed side has a negative potential. The contact between a Pt coated tip with ZnO is a Schottky diode. When the tip contacts the NW and bends it, the contact between the tip and the stretched side is a reversely biased Schottky diode. In such a case, piezoelectric potential is created in the NW, but there is no charge exchange across the Schottky diode although there is a piezoelectric potential in the NW side, resulting in a charge creation and accumulation. This is the first process. When the tip scans in contact mode and reaches the compressed side of the NW, a forward biased Schottky diode is formed at the interface, thus, the external electrons can flow across the interface under the driving of the piezoelectric potential, resulting in an external current detected by the measurement meter. This is the current output process.

The mechanism of the nanogenerator (NG) is based on two important physical quantities. One is the height of the Schottky barrier, which must be high enough to hold the charges from leaking, but low enough so that the strain created piezoelectric potential can effectively operate and control the diode. Secondly, the conductivity and carrier density of the ZnO NW are (have to be) adequately low in the first step to preserve the

piezoelectric potential distribution in the NW from being "neutralized" by the freely flowing charge carriers, which are electrons for n-type ZnO, but they need to be high enough to transport the current under the driving of the piezoelectric potential in the charge releasing process. From our extensive experimental studies, these conditions have been satisfactorily met by the as-synthesized ZnO NWs. In this section, series of experiments to tune the height of the Schottky barrier and the carrier density by UV irradiation to study their effects on the performance of the nanogenerator (NG) are designed. A Schottky diode between the top metal electrode and the NW arrays (array) is a must for the NG, while the carrier density has an optimum value at which the output of the NG is expected to be maximized. A testing criterion is demonstrated for determining the effectiveness of a NG for generating current

6.1.1 The Experiment Design

The aligned NW arrays (array) to be used for the experiments were grown epitaxially on an optically transparent AlN/Sapphire substrate using a method reported elsewhere. The bottom of the substrate was polished for enhancing optical transparency. At the roots of the NWs, a thin layer of ZnO film was also grown simultaneously, which served as a common electrode for electrical measurements. The fabrication of DC nanogenerator (NG) follows the methodology developed in chapter 5. A Pt coated Si zigzag electrode was aligned on top of the ZnO nanowires (NWs). A flexible spacer was placed between the top electrode and the AlN/Sapphire substrate to ensure a proper space required for the NG. The device was then packaged with a water-proof polymer. The entire NG was mounted on a UV-transparent quartz slide (SPI 01016-AB quartz slide) before testing. The packaged NG was placed upside down in a well isolated water bath, with the quartz slide and AlN/Substrate facing up so that the UV light was able to penetrate the slide and reach the core of the NG, as shown in Fig. 1(a). A 41 kHz ultrasonic wave generator was used as the source to excite the NG from the bottom of the water bath.

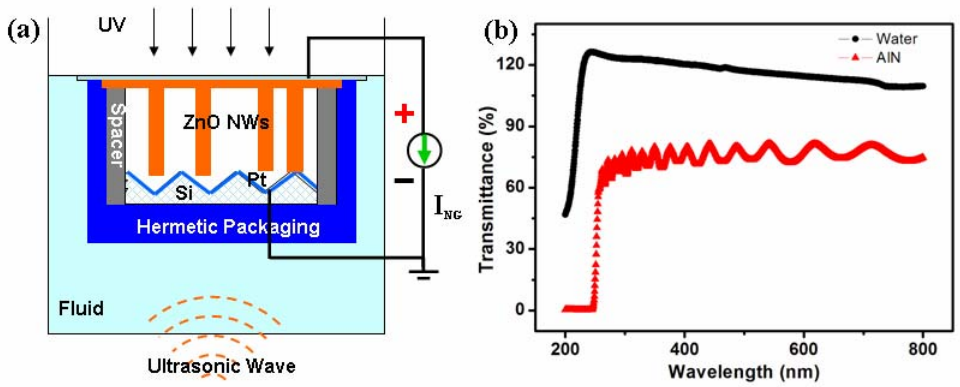

Figure 6.1 (a) Experimental set up for measuring the UV response of an assembled nanogenerator (NG) in liquid. The nanogenertor (NG) is placed up side down to ensure the UV illumination from the substrate side. (b) UV transmittance spectra through AlN/sapphire substrate and water to ensure the penetration of the UV into the core of the nanogenerator (NG).

The transmission spectrum of UV light of wavelength 260 nm (from 200nm to 800nm) was measured to ensure that the UV reached the ZnO NWs, as shown in Fig. 6.1(b). The first measurement was done for a standard UV transparent plate. Then the UV transmittance of the AlN/sapphire substrate was measured by stacking the substrate onto the plate, as shown by the red curve in Fig. 6.1(b), where the oscillation in the measured data is due to the interference of the light reflected from the substrate and the plate. Finally, the UV transmittance was measured for two parallel plates filled with water between. Due to the reduced total reflection in the water and plate interface, the measured transmittance is even better than that without water (> 100%) (dark curve). The measurement data clearly show that the UV has effectively penetrated through the substrates and water to reach the ZnO NWs.

6.1.2 Carrier Density on the Output of Nanogenerator

To evaluate the UV response of ZnO nanowires (NWs) as well as an assembled NG, two experiments have been carried out. Figure 6.2(a) shows the UV response of the vertically aligned ZnO nanowires (NWs) and the underlying ZnO thin film by connecting two electrodes at the two ends of the film, as shown in the inset.

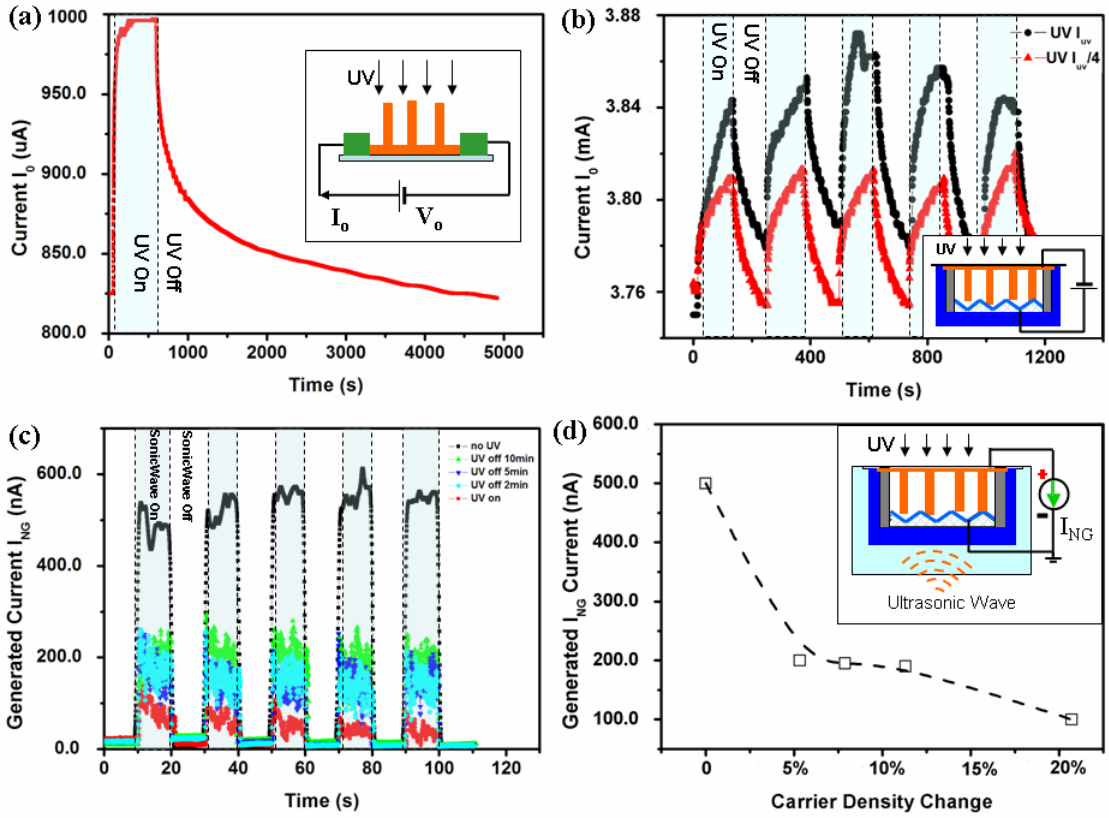

Figure 6.2 Tuning the transport property of ZnO and an assembled nanogenerator (NG) by UV excitation. (a) Response of the current transported through a thin ZnO film with NWs on top when subjecting to UV illumination, showing a long delay in the recovering process. The externally applied voltage $V_0 = 2$ V. The inset is the measurement set up. (b) Current transported through an assembled NG under an externally applied voltage $V_0 = 2$ V when the UV light was tuned on and off. The dark and red curves represent the response curve at full UV intensity I_{UV} and $I_{UV}/4$, respectively. The inset is the measurement set up.

By applying a constant voltage V_0, the transport current was monitored when the UV was turned on or off. The conductance of the film responded rapidly to UV and reached saturation after ~300 seconds. But the current decayed very slowly after the UV being turned off, possibly due to the following reason. The UV light can effectively create electron-hole pairs in ZnO, and greatly increase the carrier density. After turning off the UV, the electrons and holes would recombine and thus decrease the conductivity. But some carriers may be trapped in the surface/vacancy states in the film and NWs, greatly delayed the electron-hole recombination rate, possibly resulting in a long decay in conductivity.

The second experiment was to characterize the I-V property of an assembled NG, as shown in the inset in Fig. 6.2(b). By reducing the relative UV intensity from I_{UV} to ~ $I_{UV}/4$, the conductance of the NG changed for about 2%. The NG also responded to the on and off of the UV, clearly showing that the UV can effectively increase the carrier density in the NG and thus its conductivity.

After examining the increased conductivity in NG after UV irradiation, we now investigate the performance of the NG for generating electricity. Figure 6.2(c) is the generated current (I_{NG}) of a NG when subjecting to ultrasonic wave excitation by changing the UV irradiating condition. When the UV light was off for an extended period of time, the generated current was ~500 nA for a NG with 6 mm^2 in size, corresponding to an output current density of 8.3 $\mu A/cm^2$. This value is about 20 times higher than that reported in chapter 5. As soon as the UV light was turned on, the generated current dropped to as low as 30-80 nA. At the same time, we monitored the generated current I_{NG} after the UV was turned off for 2, 5 and 10 min, the generated current increased to ~180, 190 and 205 nA, respectively. Such a graduate increase in generated current corresponds to a slow decay in conductivity as shown in Fig. 6.2(b). This set of experiments apparently shows that an increase in carrier density, e.g., conductivity, reduces the output current of the NG. By extracting the relative change in carrier density from Fig. 6.2(a)

and the correspondingly measured NG output I_{NG} from Fig. 6.2(c), fig. 6.2(d) illustrates the monotone decrease relationship between the increased percentage in carrier density and the output current I_{NG}. This striking result indicates that the conductivity of the as-synthesized ZnO NWs is the "best" for achieving the best NG output. An annealing in oxygen may further increase the output current, but an over reducing in conductivity towards insulating would decrease the output current. We believe that there is an optimum setting for conductivity to maximum the NG output.

In a separated experiment, the output of a NG was monitored when the ultrasonic wave was continuously on but with the UV being turned on and off, as shown in Fig. 6.3. The data reproducibly show that the UV reduced the output current by 30-45%.

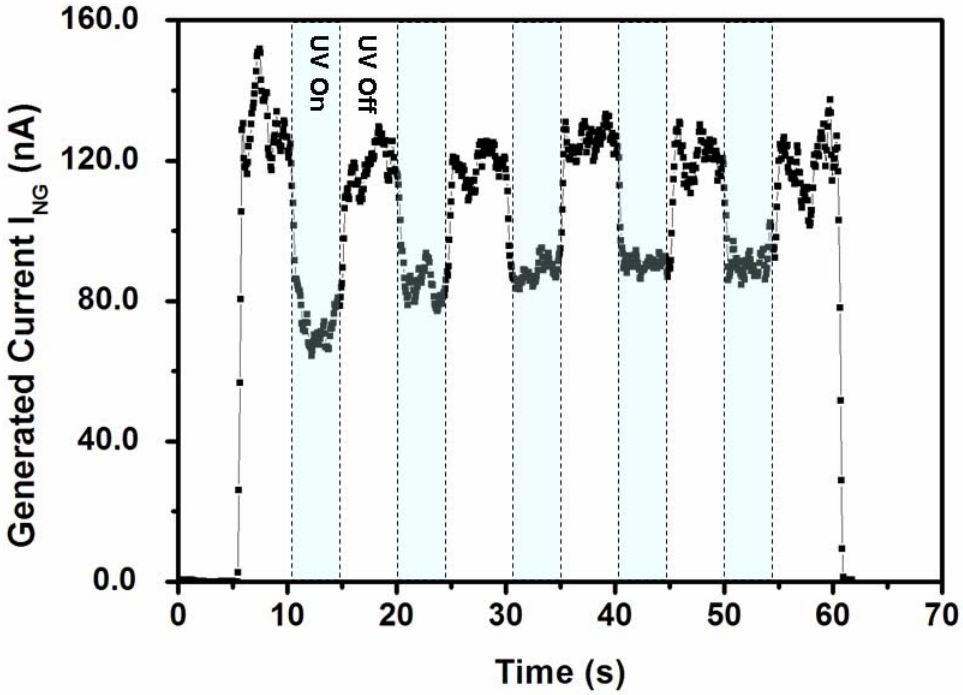

Figure 6.3 The output of a nanogenerator (NG) as excited by ultrasonic wave when the UV light was turned on and off. The UV light can reduce the output current 30-50%, indicating increasing (increase) of carrier density is not beneficial for improving the output power.

6.1.3 Schottky Barrier on the Performance of the Nanogenerator

The Schottky contact between the metal contact and ZnO nanowire (NW) is another key factor to the current generation process. Investigating its effect on the performance of NGs is very helpful in designing and fabricating high output NGs. The I-V characteristic of an assembled NG to understand its performance for current generation has been characterized. Figure 6.4 shows the I-V characteristics of a nanogenerator (NG) that does produce current once excited by ultrasonic wave (see the inset).

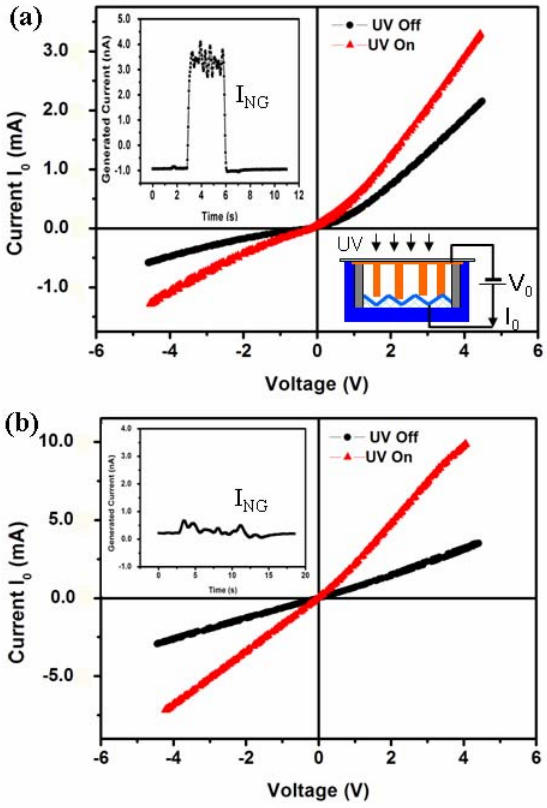

Figure 6.4 I-V characteristic of an assembled nanogenerator (NG) for identifying its performance for producing current. (a) For an NG that actively producinig (producing) current, as shown in the inset, its I-V curve when the ultrasonic wave was off clearly shows a Schottky diode behavior. UV light not only increased the carrier density (or conductivity) but also might reduce the barrier height. (b) For a "defective" NG that did

not produce current, the I-V curve clearly shows a clearly Ohmic behavior. The UV light clearly increased the conductivity.

The experimental setup for the measurement is inset at the right-lower corner in Fig. 6.4(a). The NG exhibits a Schottky-like I-V characteristic, which means that the NG has different response for forward and reverse biases. When illuminated by UV, the NG showed (shows) an increased conductance, and its Schottky-like rectifying effect is largely reduced due to the increased conductance. A "defective" NG that does not produce current in responding to ultrasonic wave is chosen, its I-V characteristics is clearly Ohmic even before being illuminated by UV. By examining over 10 assembled NGs, the corresponding I-V characteristics reliably indicate if the NGs are good. This provides a criterion for identifying a working NG vs a defective one.

To examine the role played by Schottky barrier in the NG, we used the atomic force microscopy (AFM) set up as used in our first study for demonstrating the piezoelectric NG under same experimental conditions (see Fig. 6.5(a)) to study the output of an arrays (array) of ZnO NWs with the use of two types of conducting tips.

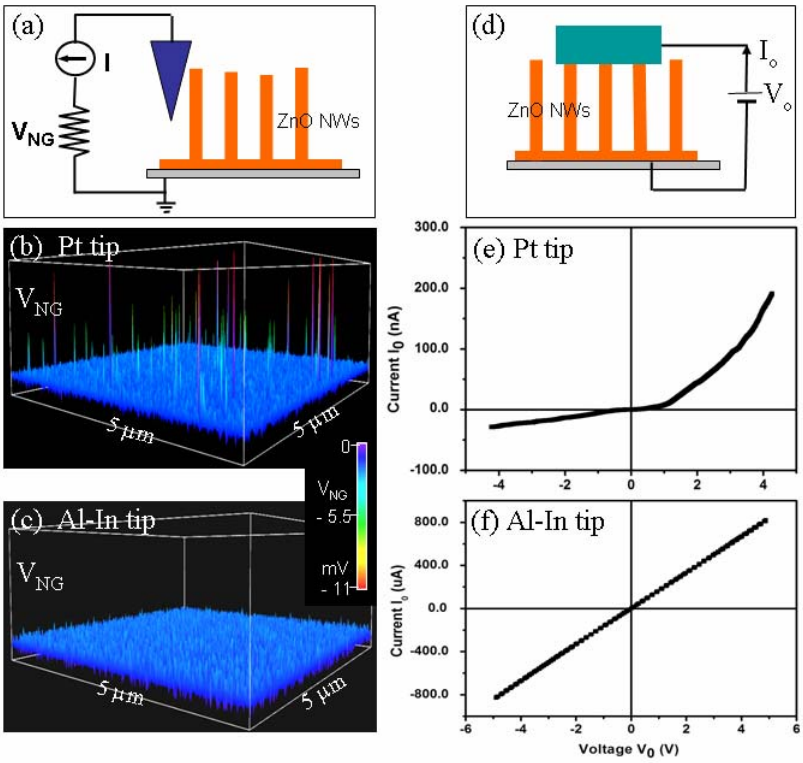

Figure 6.5 (a) AFM based measurement set up for correlating the relationship between the metal-ZnO contact and the NG output. (b) Output potential generated by ZnO NW array when scanned by a Pt coated Si tip. (c) No output potential is generated by ZnO NW array when scanned by an Al-In coated Si tip. (d) Experimental set up for characterizing the I-V transport property of metal-ZnO NW contact. (e) I-V curve of a Pt-ZnO NW contact, showing Schottky diode effect. (f) I-V curve of an alloyed Al/In-ZnO NW contact, showing Ohmic behavior.

The AFM scans in the contact mode and the generated piezoelectric current is detected by measuring the voltage at an external load in reference to the grounded end. The first tip is a Pt (100 nm) coated Si tip, using which output potential peaks were observed when the tip scanned in contact mode across the NW arrays (Fig. 6.5(b)), and the output voltage peaks were in the order of ~ - 11 mV (the negative sign means that the current flowed from the grounded end through the external load). By changing the tip into

an Al-In (30 nm/30 nm) alloy coated Si tip, the ZnO NWs shows (showed) no piezoelectric output (Fig. 6.5(c)). In order to understand the two distinct performances of the two types of scanning tips, The I-V characteristics of the contacts the two types of metal electrodes and the ZnO NWs have been measured. To ensure the stability of the contact, a large electrode that is in contact with a group of NWs is used, as shown in Fig. 6.5(d). As for the Pt-ZnO contact, the I-V curve clearly presents a Schottky diode (Fig. 6.6(e)), while the Al-In alloyed electrode has an Ohmic contact with ZnO. In reference to the piezoelectric output presented in Fig. 6.5(b, c), a Schottky contact between the metal electrode and ZnO is mandatory for any working the NG.

6.14 UV illumination on the Performance of the Schottky Barrier

As illustrated in the last section, the presence of a Schottky barrier between the metal electrode and the ZnO NWs is a key for determining the performance of the NG. Now examine the influence of UV light on the I-V characteristic of a Schottky diode. Using a pair of Au electrodes interconnected by a ZnO NW, a Schottky diode based device was fabricated (see the inset in Fig. 6.6), which may be produced by the asymmetric contacts of the ZnO NW with the two electrodes.

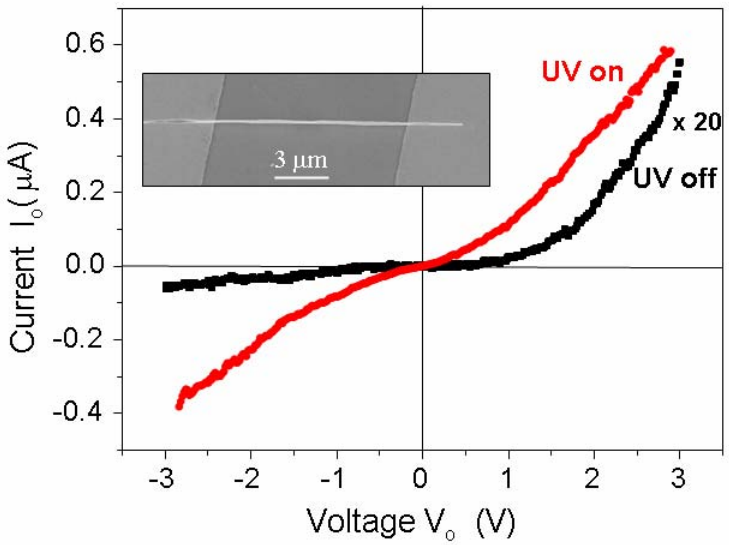

Figure 6.6 Two-electrode based device fabricated using a ZnO nanowire for measuring its transport property when subjecting to UV illumination. An SEM image of the device is inset. The asymmetric contact at the two ends results in a Schottky diode. The UV not only increased the carrier density but also reduced the barrier height at the interface.

The I-V characteristic of the diode is apparent. After being illuminated by a UV light, the conductance of the device has been improved over 20 times; more importantly, the threshold voltage of the diode has been greatly reduced from close to 1 V to almost zero before and after UV illumination (Fig. 6), and the I-V curve shows an Ohmic-like behavior. Therefore, a weakening or disappearing rectifying effect of the diode is likely to be the reason why the performance of the NG as shown in Fig. 2(c, d) is deteriorated with the increase of UV generated carrier density.

In summary, by assembling a ZnO nanowire (NW) array based nanogenerator (NG) that is transparent to UV light, the performance of the NG by tuning its carrier density and the transport property of the Schottky barrier between the metal electrode and the NWs have been investigated. The presence of a Schottky diode between the top metal electrode and the ZnO NWs is mandatory for the effective operation of the NG. UV light not only increases the carrier density in ZnO but also can reduce the barrier height between the metal electrode and ZnO. A reduced Schottky barrier height greatly weakens the function of the barrier for preserving the piezoelectric potential in the NW. A replacement of a Schottky contact by an Ohmic contact override (overrides) the role played by the barrier for accumulating the piezoelectric charges. If there is no charge accumulation in the first step, no charge would be released in the a later step. Our study shows that identifying the existence of the Schottky diode transport property of a NG is an effective means for identifying if the NG is good or defective.

An increased carrier density speeds up the rate at which the piezoelectric charges are screened/neutralized. But a very low carrier density may improve the local

piezoelectric potential and prevents (prevent) the flow of current through the NWs, as well as increases (increase) the inner resistance of the NWs and possibly the contact resistance at the interface. Therefore, there should be an optimum choice of nanowire (NW) conductance for maximizing the output of the NG. NWs with excellent conductivity may greatly reduce the life time of the piezoelectric charges, resulting in very small or no output current. A comprehensive computer simulation with considering the dynamics of charge transport is necessary for predicting the value of the optimum conductance.

6.2 P-Type Oligomer Functionalized ZnO Nanowire Nanogenerator

In Chapter 3,4 we have used nanowire arrays of ZnO for converting mechanical energy into electricity[109,114]. The principle of the nanogenerator relies on the coupled semiconducting and piezoelectric properties[99,115]. When a clean ZnO nanowire or nanobelt is bent by an atomic force microscope (AFM) tip, as a result of piezoelectricity, the stretched side of the NW has a positive potential and its compressed side has a negative potential. Due to the existence of a Schottky barrier between the AFM metal tip and the ZnO NW, the contact between the tip and the stretched side is a reversely biased Schottky diode, while the contact with the compressed side is a forward biased Schottky diode; a charge creation-accumulation and charge release process is created at the interface when the tip scans across the NW, resulting in a current flowing from the metal tip to the ZnO NW. The voltage drop across an external load shows a negative voltage pulse. This is the process of the piezoelectric energy conversion.

It is well known that the surface chemical and physical properties of a semiconductor oxide can be substantially improved by polymer functionalization[116]. As a unique advantage of NWs, surface functionalization can drastically improve its performances, such as its UV response and conductivity[117, 118]. The mechanism of the nanogenerator largely depends on the surface contact, which may critically affect the

charge accumulation and release process. Surface functionalization is therefore expected to be an effective pathway to alternate, rectify, or enhance the potential output. In this section, the investigation about the piezoelectric output of a ZnO wire/belt coated with a thin layer of p-type oligomer will be discussed. An explanation is provided about the observed "abnormal" output voltage, which provides additional evidence about the mechanism proposed previously for the piezoelectric nanogenerator.

6.2.1 The Experiment Setup

The experiment was based on mechanical manipulation of a single ZnO wire/belt using AFM. The selected ZnO wire/belt was long enough to be directly visualized under optical microscope built in AFM. One end of the ZnO wire/belt was fixed on to a flat intrinsic silicon substrate using silver paste that is electrically grounded; while the other end was left free (see the left-lower corner inset in Fig. 6.7).

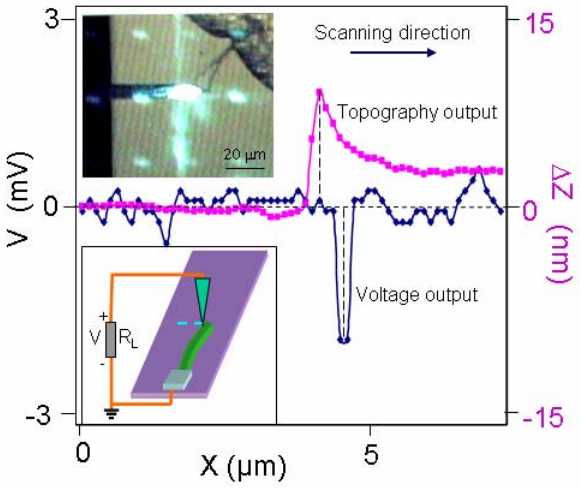

Figure 6.7 In situ observation of the process of outputting piezoelectric potential by scanning a one-end-free ZnO wire/belt using an AFM tip. The ZnO is clean without oligomer coating. Top inset is a snapshot optical image of the AFM tip that is deflecting the wire/belt. Bottom inset is a schematic experimental setup. The curves are the aligned

plot of the output voltage (blue curve) over the external load and the topography profile (pink curve).

The silicon substrate was an insulator. The ZnO wire/belt was laid parallel to and a little bit above the substrate in free suspension to eliminate friction. A resistor R_L = 500 MΩ is connected between the fixed end of the ZnO wire/belt and the AFM tip, and the output signal is characterized by a voltage drop across the resistor in reference to the grounded end. The measurement was performed using an AFM (model MFP-3D from Asylum research) with a Pt coated silicon tip (Electri-Lever AC240 from Asylum research), which has a tetrahedral tip of 14μm in height. The cantilever has a spring constant of 1.6 N/m. All of the measurements were performed in contact mode with a set point of 5 nN and a scanning speed between 60 to 160μm/s. No external voltage was applied at any stage of the experiment. Both the topography and potential output (V) images on the resistor were monitored simultaneously during the tip scan. The entire experiment was recorded at video rate so that the electric energy generation process can be directly visualized. The data presented in the figures were snapshots of the characteristic events extracted from the video and the corresponding experimental data.

For comparison purpose, we first studied the piezoelectric output from a clean ZnO wire/belt that had no surface coating. During the scan, when the tip only touched the stretched side of the wire/belt and did not lift up to go beyond the central line of the wire/belt to reach the compressed side, there was no voltage output signal. The output voltage peak was observed only when the tip went beyond the wire/belt to reach its compressed side, as characterized by a peak in the topography image (pink curve) in Fig. 6.7. The corresponding output voltage is represented by the blue curve in Fig. 6.7, which is always a negative peak in reference to the grounded end of the wire/belt. It is also important to note that the center of the voltage peak was delayed in reference to the peak in the topography image. These are the most important characteristics for a ZnO wire/belt

without surface functionalization, and they have been explained as a result of a "switch effect" created by the Schottky barrier between the AFM tip and the ZnO wire/belt.

6.2.2 Phenomena of Power Generating from OPV Functionalized ZnO Wire/belt

This part presents the case when the ZnO wire/belt was coated with a thin layer of OPV (oligomer (p-phenylene vinylene)) derivatives, which is selected because they are extensively studied p-type oligomers for light emitting, field-effect transistors, supramolecular assembly, and amphiphilic due to their high absorption coefficient, strong donating ability, and good thermal, chemical, and photochemical stability[119, 120, 121, 122].

6.2.2.1 Experiment Setup and Preparation

The as-synthesized ZnO wire/belt was immersed in 1% Mol/L (alpha,omega-bis(methylthioacetate) oligo(phenylene vinylene)-COOH) (OPV2) menthol solution for 48 hours. Then, the wire/belt was taken out and rinsed by deionizer water and dried in air. A 2-3 nm-thick OPV2 was coated on the surface of ZnO wire/belt (see the inset TEM image in Fig. 6.8). Using this functionalized wire/belt, we performed the same experiment as described in Fig. 6.7 and a typical voltage output is presented in Fig. 6.8a.

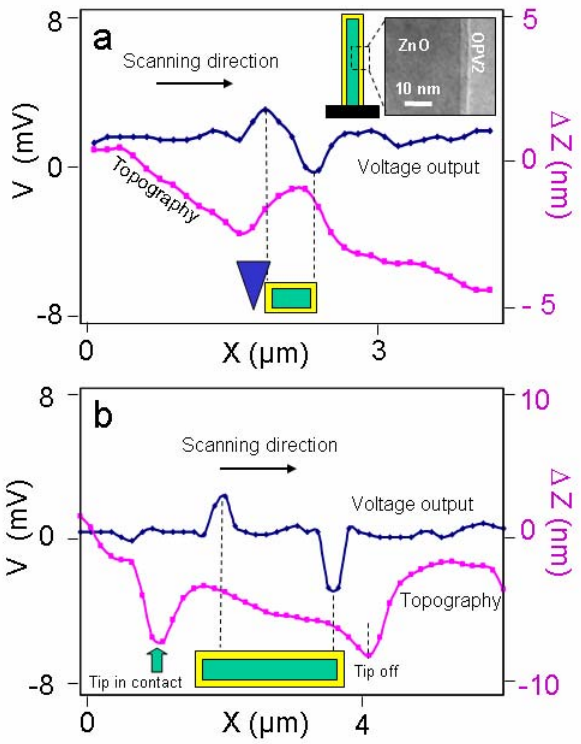

Figure 6.8 In situ observation of the process of outputting piezoelectric potential of a one-end-free ZnO wire/belt that is coated with a thin layer of OPV2. (a, b) Aligned plot of the output voltage (blue curve) over the external load and the topography profile (pink curve) measured from two different wires/belts. Top inset is a TEM image showing the thickness of the oligomer coating. Schematic cross-section of the wire/belt is illustrated.

In contrast to the case of ZnO wire/belt without surface functionalization, a pair of positive and negative output voltage peaks was observed. The positive peak appeared when the tip was in contact with the stretched side of the wire/belt, and the negative peaks showed up when the tip was in contact with the compressed side, which was determined by examining the peak positions in reference to the signal in the topography image. The uneven background in the topography image is caused by the downward bending and/or slight vibration of the free-standing wire/belt during the scan. In our experiments, some of the scans produced only positive voltage pulses; some generated only negative pulses;

and some generated both. In reference to the information provided by the topography image, the negative pulse was generated only when the AFM tip scanned over the central line and reached the compressed side of the wire/belt, which is consistent to our previous observation.

6.2.2.2 Special Phenomena

Figure 6.8b shows a typical tip scan profile across a ZnO belt, in which both the positive and negative pulses were generated when the tip scanned from the stretched side to the compressed side of the belt. In the contact mode, the tip was lifted up by the belt to keep a constant normal force. Since the belt was freely suspended, it may move slightly downward or even vibrate when it was pushed by the tip, thus, the uneven background was recorded. Moreover, the width of the topography profile was rather wide in comparison to the actual width of the wire/belt because the wire/bent was continuously pushed and bent when the image was acquired. The vertical distance, ΔZ, may not be the actual thickness of the wire/belt owing to its free-standing configuration and the shape of the tip. The positions at which the tip touched the belt and started to lift up can be clearly identified, as indicated by an arrowhead in Fig. 6.8b. By correlating the relative position of the voltage peak to the topography image of the belt, no voltage was released when the tip first contacted the belt. The positive voltage peak appeared after the tip pushed the belt for ~0.5 μm along the scanning direction. This indicates that the belt had to be bent to a certain angle/distance before the voltage pulse was released. The delayed discharging peak clearly shows that a simple physical contact cannot produce the voltage pulse, which rules out the contributions from surface/volume electrostatic charge, friction charge or even measurement circuit. As for the negative voltage peak, it appeared that the voltage pulse was released before the tip lost contact with the belt, as indicated by the dip in the topography curve.

6.2.3 Proposed Principle of Power Generating from OPV Functionalized ZnO Wire/belt

To understand the phenomena we observed in Fig. 6.8, the transport properties of the ZnO wire/belt, OPV2 and OPV2 functionalized ZnO wires were characterized. Two pieces of ZnO NW arrays were cut from the same sample grown on ITO glass substrate, with only one of them being functionalized with OPV2. To maintain the reliability and stability of the I-V measurements, two ~2 mm^2 size Pt electrodes were employed for the contact measurements. One Pt electrode was connected to the bottom ITO layer, and the other Pt electrode was put in contact to the tips of the nanowire arrays, as shown in the inset of Fig. 6.9.

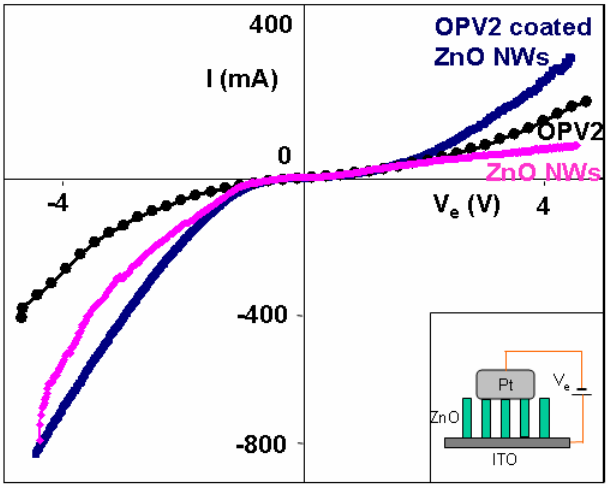

Figure 6.9 I-V Characteristics of the contacts between Pt electrode and ZnO nanowires without coating (pink); Pt electrode and OPV2 (black); Pt electrode and OPV2 functionalized ZnO nanowires (blue). Inset is a schematic diagram of the experiment set up. A flat Pt electrode was placed on the top of the aligned ZnO nanowire with or without coating a layer of p-type oligomer.

The externally applied voltage was swap from -5 to 5 V. The I-V curve shows that the contact between Pt and ZnO nanowire is a typical Schottky contact (pink curve in Fig. 6.9). To characterize the contact between Pt electrode and OPV2, I-V measurement was performed on an OPV2.covered ITO glass substrate, where one electrode contacted ITO glass and the other one was in contact with the OPV2 layer. The contact between Pt and OPV2 is Ohmic (black curve in Fig. 6.9). The contact between OPV2 coated ZnO NWs and Pt electrode is a non-symmetric curve. When $0<V_e< 1.5$ V, the I-V characteristic is the Schottky type, but when $V_e>1.5$ V, the I-V curve starts to show the Ohmic behavior. This indicates that the p-n junction can be break through when the local potential is larger than ~ 1.5 V. For a large belt used in our experiments of a few hundreds nanometer in width, the local piezoelectric potential can be a few to a few tens of volts according to the calculation (Eq. (6.1)). Thus, it is possible to have a local break through at large deflections. It is apparent that the OPV2 coating has changed the transport properties of the contacts, which is important for understanding the phenomenon presented in Fig. 6.8.

After knowing the contact characteristics, we proposed a model for understanding the voltage signal shown in Fig. 6.8. Our model is based on the mechanism presented previously for understanding the charge creation-accumulation and charge releasing processes proposed for a clean ZnO wire/belt. By bending a ZnO wire/belt, an asymmetric strain distribution across its width results in an asymmetric potential distribution, with a positive potential ($V_s^+>0$) at its stretched side and negative potential ($V_s^-<0$) at the compressed side.[123] Typically, an as-grown ZnO NW is n-type. For a clean ZnO wire/belt without oligomer coating, a Schottky diode is presented at the interface between the Pt tip and the n-type ZnO wire/belt, which controls the charge accumulating and releasing process. Since the work function of Pt is 6.1 eV and the electron affinity of ZnO is 4.5 eV [124], the Pt-ZnO contact is Schottky with a barrier height of 1.6 eV for bulk materials. Recent STM experimental measurement shows that

the barrier for nanocontact is 0.45 eV and is very sensitive to local strain, which is significantly lower than that of bulk contact.[125] The piezoelectric potential V_s^+ is proportional to the degree of bending of the wire/belt and it is simply described by a simple formula of

$$V_s^{\pm} \approx \pm 27\ (a/L)^3\ y_m \quad \text{(in V)} \qquad (6.1)$$

where a and L are the radius and length of the NW, respectively, and y_m (in nm) is the lateral displacement at tip of the NW. For a typical wire of a = 1 μm, L = 40 μm and y_m = 10 μm (see Fig. 6.7), the maximum potential at the surface is $(V_s^{\pm})_{max} \approx \pm 4.2$ V.

When the ZnO wire/belt is functionalized with a thin layer of OPV2, the Pt tip is separated from the n-type ZnO wire/belt by this p-type oligomer. Since the contact between Pt and ZnO is Ohmic, the carrier transportation from Pt to ZnO is controlled by the p-n junction formed between OPV2 and ZnO. From the I-V characteristic presented in Fig. 6.9, it is likely that the p-n junction barrier height $\Delta\phi$ between OPV2 and ZnO is lower than Schottky barrier height between Pt and ZnO. When the tip first touches the OPV2 coated wire/belt (Fig. 6.10a), it deflects the wire/belt and the piezoelectric charges are continuously produced, but the local potential V_s^+ created is smaller than the barrier height because V_s^+ is proportional to the lateral deflection of the nanowire (Eq. (1)), thus, the p-n junction at the OPV2-ZnO interface is reversely biased (Schottky type).

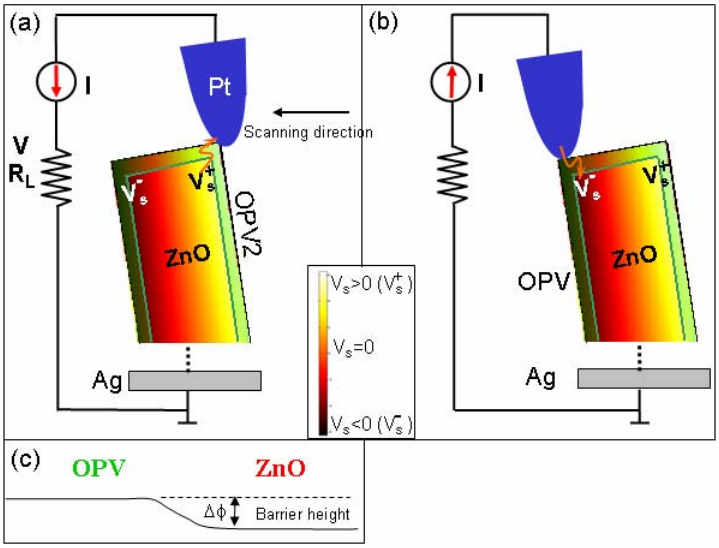

Figure 6.10 Proposed model of the piezoelectric potential generated from a OPV2 coated ZnO wire/belt when deflected by an AFM tip. (a, b) Metal and semiconductor contacts between the AFM tip and the semiconductor ZnO belt coated with OPV2 at positive and negative local contact potential (see text). (c) Schematic diagram showing the barrier height at the OPV2-ZnO p-n junction.

In this case the charges are accumulated without releasing due to the rectifying effect of the p-n junction. With the further increase of bending, the local piezoelectric potential V_s^+ becomes larger than the barrier height $\Delta\phi$ (Fig. 6.10c) and the p-n junction is broken through (Ohmic type). Thus, the current flows from the ZnO wire/belt into Pt tip through the OPV2 layer resulting in the positive potential peaks as presented in Fig. 6.8.

If the Pt tip scans fast across the wire/belt, two possible consequences could be resulted. First, the contacting time may be so short that the piezoelectric charges could not be completely neutralized/screening by the external electrons if the carrier density and carrier mobility were low in OPV2. As a result, a small potential may still be preserved

even after neutralizing/screening part of the charges. The other possibility is that the wire/belt could be continuously bent when the tip scanned from the stretched side to the compressed side, which generates additional potential with the increase of deformation. When the conductive tip reaches the compressed side of the ZnO wire/belt, the negative piezoelectric potential V_s^- at the ZnO side sets the p-n junction to forward bias, resulting in a flow of current from the Pt tip into the ZnO wire/belt, thus, negative voltage pulses are observed (Fig. 6.8). In an alternative case, if all of the charges are neutralized/screened when the tip contacts the stretched side of the wire, and no more deflection is introduced when the tip slides to the compressed side, there will be no negative pulse output. This is likely the reason that only a positive pulse is observed in some of the scans.

CHAPTER 7

SUGGESTED FUTURE WORK

In this short chapter, the future work followed the major research in this dissertation will be suggested.

7.1 Improve the Current or Voltage output of Nanogenerators

The key problem which impedes the commercialization of nanogenerator is that the output is too small to have real application. The suggested future work in this section may provide an applicable solution.

7.1.1 Design Universal Mask to Fabricate Next Generation Nanogenerator

By the high resolution of scanning electron microscopy, electron beam sensitive polymer will be employed to fabricate a special mask with regular angular nanoscale stripe pattern. The distance between any two adjacent slits and the width of the slit will be optimized by series of optimization experiments.

The mechanism is like Fig. 7.1 below.

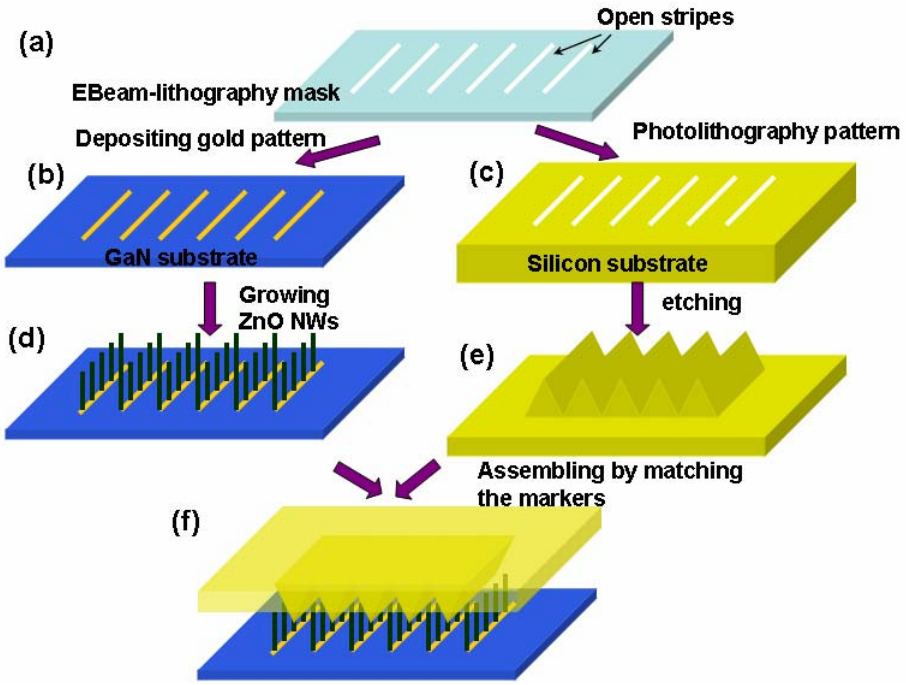

Figure 7.1 Schematic design for the high output nanogenerator. (a) E-Beam lithography mask with open stripes. (b) Depositing gold pattern on GaN substrate by using the mask in (a). (c) Silicon substrate with photolithography pattern by using the mask in (a). (d) Growing ZnO nanowires by the substrate in (b). (e) Chemical etching the patterned silicon substrate to for zigzag electrode. (f)Diagram for assembling nanogenerator by the patterned growth ZnO nanwires sample with the matching silicon zigzag electrode coated with Pt.

Fabrication of the mask is proposed to use E-Beam lithography, which has better resolution than photo lithography. The initial pattern of the mask is stripe, which width is within nanometer scale as in Fig. 7.1 a. This mask will be utilized to do photo lithography to form the golden pattern on GaN substrate (Fig. 7.1 b) and the photo lithography on silicon substrate (Fig. 7.1 c). The GaN substrate with patterned gold will be used to synthesize well aligned ZnO nanowire arrays by VSS method for the epitaxial match between the lattice parameters of ZnO and GaN, which will induce the perpendicularly growth of ZnO nanowire arrays (Fig. 7.1d). The principle could be found in chapter 2 in this dissertation. For the patterned gold strips will serve as the catalyst to induce the

growth of ZnO nanowire arrays, the as-synthesized ZnO nanowire arrays will form the pattern matching the original mask made by E-Beam lithography. The patterned silicon wafer will be developed by chemicals to fabricate zigzag trenches (Fig. 7.1 e) according to the original pattern of the mask (Fig. 7.1 a) and further coated with Pt layer in order to form Schottky barrier with ZnO nanowires. After growth the patterned aligned ZnO nanowire arrays on GaN substrate and the fabrication of the etched zigzag electrode, the zigzag silicon wafer will be placed face down on the top of the patterned growth ZnO nanowire arrays with carefully adjustment to guarantee the match of the top electrode and the ZnO nanowire arrays below (Fig. 7.1 f).

Fine applicable procedure should be found to adjust the top electrode to exactly math the patterns on both top electrode and the ZnO nanowire arrays. Further more, the vertical distance between the patterned top zigzag electrode and the corresponding ZnO nanowire arrays should be adjusted to the desired value which could let the ZnO nanowire arrays right in the trench without touching.

The technique illustrated above could improve the quantity of workable nanowires intensively, but the height uniformity is another key problem to be solved.

7.1.2 Growth Parameter Control to Improve the Uniformity of ZnO Nanowires

As for the nanogenerator assembly, increasing the uniformity is the first key to improve its electric output. Our previous research has identified the best parameter of chamber pressure, oxygen concentration and catalyst. The main reason that causes the height variation is the NWs nucleate at different time. In light of this situation, Further investigation should be taken to growth parameters and deposition system to eliminate the variance in nucleation time and achieve the aligned NWs with height variance within ± 2% or ± 40 nm for 2μm-long NW arrays.

My previous work indicated the thickness of the gold which is deposited on the substrate to introduce the growth affected the nanowire quality. Series of experiment

should be carry out to investigate the relationship between thickness of catalyst and the growth quality of ZnO nanowires in order to get the best growth conditions.

7.1.3 Optimization Frequency of Input Untrasonic Wave

Ultrasonic wave source with tunable frequency will be used in the optimization of input ultrasonic wave to find the maximum output of nanogenerator with certain length of nanowire arrays.

A cure of output power vs. the input ultrasonic wave frequency will be explored, from which the optimization of the frequency for the stimulating ultrasonic wave will be found.

CHAPTER 8

CONCLUSION

The dilemma of scarce research carried out on nano power sources impedes the real application of nanotechnology. This dissertation focuses on innovatively research on a nanogenerator based on ZnO nanostructures, which provides an ideal solution.

Starting from the synthesis of basic nanomaterial, well aligned ZnO nanowire arrays on GaN substrate by VSS method, a "Phase Diagram" for growing well aligned uniformly ZnO nanowire arrays on GaN substrate is found. By controlling two key synthesis parameters, oxygen partial pressure and total chamber pressure, more than one hundred synthesis experiments have been carried out. A matrix for the growth quality under oxygen partial pressure varying from 1 to 4 vol.% and chamber pressure from 1.5 to 300 mbar is determined. The "Phase Diagram" provides a roadmap for fabricating aligned ZnO nanowires at large-scale and controlling nanowire synthesis. The synthesis of aligned ZnO nanowire arrays on nitride substrates is also investigated. For epitaxial match between lattice parameters of ZnO nanowire and the substrates, the lateral growth of ZnO nanowires is restrained. This research builds primary knowledge on substrate selection for synthesizing well aligned ZnO nanowire arrays.

The mechanical property of the nanostructure is very important to the property and reliablility of the nanodevice fabricated from it. An innovative method to measure the mechanical property of an aligned nanostructure on solid substrate without manipulating and destroying the sample has been invented. By using AFM working in contact mode, well aligned ZnO nanowire arrays on sapphire substrate is scanned. Both the topography

and lateral force are recorded. The scanning line from topography gives the height and the maximum bending distance of each nanowire, from which the Young's modulus can be derived. The average elastic modulus of an aligned ZnO nanowire is measured to be 29 ± 8 GPa. The same measurement is also carried out on RuO_2 and a RuO_2/TiO_2 core/shell structure, and the elastic modulus is measured to be 194 GPa without destroying the sample. Furthermore, the elastic modulus of aligned Ni-doped metallic $TaSi_2$ nanowires is found to be 302 GPa by the same method.

Based on the mechanical property measurement, the first nanogenerator has been demonstrated using conductive AFM scanning on the aligned ZnO nanowire arrays. Due to the semiconducting and piezoelectric dual properties, a ZnO nanowire can convert mechanical energy into electricity. When an aligned ZnO nanowire is bent by the conductive AFM tip coated with a layer of platinum, the compressed side of the nanowire gains negative potential while the stretch side has positive potential due to the piezoelectric property of ZnO. The Schottky barrier formed by the platinum coated AFM tip and the semiconductor ZnO is reversely biased. When the tip touches the stretched side of the nanowire, the polarized charges are separated and accumulated. As the tip goes across the top of the nanowire and touches the compressed side, the Schottky barrier is forward biased by the positive potential and the polarized charges are neturalized by free electrons from the outer circuit to realize the power converting process. The voltage output from the nanogenerator is around 8 mV. The same process is carried out on ZnO nanowires grown on plastic substrate to meet the applications which require flexible or foldable building materials. The observed maximum of 25 mV from the nanowire grown on the plastic substrate is due to the bigger diameter and height of the nanowires.

In order to understand the principle of the nanogenerator in depth, and to further explore the ability of harvesting electric energy from the environment, the power generating process from a single ZnO wire/belt is investigated. The principle of nanogenerator is further confirmed through these measurements.

For real application, the true nanogenerator should eliminate the AFM. A zigzag top electrode, which is coated with a layer of platinum and put on the top of aligned ZnO nanowire arrays is designed to be instead of conductive AFM tip. The distance between the top electrode and the ZnO nanowire arrays is carefully adjusted and maintained by a polymer. Ultrasonic waves are introduced as the stimulating mechanical energy, and direct current electrical power is generated from the DC generator. The short circuit current output is around 0.1 nA and the open circuit voltage output is around 0.5 mV. Ideally, the nanogenerator built using the NWs grown on an area of 1 cm^2 could be effective for powering 100-500 nanodevices.

The ability of the DC generator to work in bio-fluid is also investigated. A waterproof polymer is applied to package the generator and the performance is checked in the bio-fluid. The possiblity of parallelizing more than two nanogenerators to increase the current output and serializing nanogenerators to improve voltage output is also demonstrated. The intensity of stimulating ultrasonic wave is also a key factor to the output of the nanogenerator.

As the core of this dissertation, the nanogenerator is demonstrated as a roadmap to the new research field Nano-Piezotronics. For a typical example, the piezoelectric field effect transistor is fabricated. A single crystal ZnO nanowire is applied with certain

voltage through the micro manipulators under SEM. As the nanowire bends, the current through the nanowire decreases. This is due to the electrical field produced by the deformation of piezoelectric ZnO nanowire attracting most of the carriers to one side of the nanowire, which produces the depletion zone. The nanowire's ability of being a nano-force sensor is also demonstrated by this device.

Further investigations on the carrier density and Schottky barrier effects on the performance of the nanogenerator are also discussed in this dissertation. The carrier density is controled by doping or annealing samples which will be built into nanogenerators. Too many carriers in the ZnO nanowires will neutralize the piezoelectric charges, while too few carriers will increase the inner resistance of the nanogenerator, also decreasing the performance. The Schottky barrier must be high enough to hold the charges from leaking, but low enough so that the strain created piezoelectric potential can effectively operate and control the diode.

The power generation of a p-type oligomer functionalized ZnO nanowire is characterized to further understand the primary principle of the nanogenerator. The p-type oligomer forms a diode with the n-type ZnO nanowire, which serves as the gate to accumulate and release polarized piezoelectric charges. When the potential generated overwhelms the breakthrough point of the diode, positive potential can be detected. This is a special phenomenon of nanogenerators fabricated from oligomer functionalized ZnO nanowires.

In summary, this dissertation presents systematical research on the nanogenerator, the roadmap for real application of nanotechnology. From the synthesis of aligned ZnO

nanowire arrays to characterize the mechanical property, the nanogenerator is invented by first using the conductive AFM. A prototype DC nanogenerator driven by ultrasonic waves is fabraicated; the investigations on the details of the nanogenerator are discussed in depth. The work in this dissertation builds a solid basis of Nano-Piezotronics.

REFERENCES

[1] Pan, Z. W.; Dai, Z. R.; Wang, Z.L. *Science* 2001, *291*, 1947

[2] Huang, M.; Wu , Y.; Feick, H.; Weber, N. Tran,E.; Yang, P. *Adv. Mater* 2001, *13*, 113.

[3] Ng, H. T.; Chen, B.; Li, J.; Han, J.; Meyyappan, M.; wu, J.; Li, X.; Haller, E.E. *Appl. Phys. Lett.* 2003, *83*, 2023

[4] Kong, X.Y.; Wang, Z.L. *Nano Letters*, 2003, *3*, 1625-1631

[5] Arnold, M. S.; Avouris, P.; Pan, Z. W.; Wang, Z. L. *J. Phys. Chem.B* 2003, *107*, 659.

[6] Johnson, J.; Yan, H.; Yang, P.; Saykally, R. *J. Phys. Chem. B*, 2003, *107*, 8816.

[7] Liu, C.; Zapien, J. A.; Yao, Y.; Meng, X.; Lee, C. S.; Fan, S.; Lifshitz, Y.; Lee, S. T. *Adv. Mater. (Weinheim, Ger.)* 2003, *15*, 838.

[8] Zhong, Z.; Wang, D.; Cui, Y.; Bockrath, M.W.; Lieber, C.M. *Science* 2003, *302*, 1377-1379.

[9] Wang, Z.L. *materials today* 2004,*June*, 26-33.

[10] Wang, X. D.; Summers, C. J.; Wang , Z. L. *Nano Lett.* 2004, *4*, 423

[11] Li, S. Y.; Lin, P.; Lee, C. Y.; Tseng, T. Y. *J. Appl. Phys.* 2004, *95*, 3711.

[12] Zhao, Q. X.; Willander, M.; Morjan, R. R.; Hu, Q. H.; Campbell, E. E. B. *Appl. Phys. Lett.* 2003, *83*, 165.

[13] Park, W. I.; Yi, G. C. *Adv. Mater.* 2004, *16*, 87.

[14] Krumeich, F.; Muhr, H. J.; Niederberger, M.; Bieri, F.; Schnyder, B.; Nesper, R. *J. Am. Chem. Soc.* 1999, *121*, 8324

[15] Sun, X. C.; Zhang, H. Z.; Xu, J.; Zhao, Q.; Wang, R. M.; Yu, D. P. *Solid State Comm* 2004, *129* 803.

[16] Hg, H. T.; Chem, B.; Li, J.; Han, J.; Meyyappan, M.; Wu, J.; Li, S. X.; Haller, E. E. *Appl. Phys. Lett*. 2003, *82,* 2023.

[17] Fan, H. J.; Fleischer, F.; Lee, W.; Nielsch, K.; Scholz, R.; Zacharias, M.; Gosele, U.; Dadgar, A.; Krost, A. *Superlattices and Microstructures* 2004, *36,* 95.

[18] Park, W. I.; Yi, G. C. *Adv. Mater.* 2004, *16*, 87.

[19] Wang, X. D.; Song, J.; Peng, L.; Ryou, J. H.; Dupuis, R. D.; Summers, C. J.; Wang, Z. L. *J. Am. Chem. Soc.* Submitted.

[20] Arnold, S. M. and Kounce, S. E., J. Appl. Phys. 27, 964 (1956).

[21] Sears, G. W., Acta Metall. 3, 361 (1955).

[22] Blakely, J. M. and Jackson, K. A., J. Chem. Phys. 37, 428 (1962).

[23] Dai, Z. R., Pan, Z. W. and Wang, Z. L., Adv. Func. Mater. 13, 9 (2003).

[24] Wagner, R. S. and Ellis, W. C., Appl. Phys. Lett. 4, 89 (1964).

[25] Morales, A. M. and Lieber, C. M., Science 279, 208 (1998).

[26] Huang, M. H., Mao, S., Feick, H., Yan, H., Wu, Y., Kind, H., Weber, E., Russo, R. and Yang, P., Science 292, 1897 (2001).

[27] Cui, Y., Lauhon, L. J. and Gudiksen, M. S., Appl. Phys. Lett. 78, 2214 (2001)

[28] Huang, M. H., Wu, Y., Feick, H., Tran, N., Weber, E. and Yang, P., Adv. Mater. 13, 113 (2001)

[29] Kirkham, M.; Wang, X.D.; Wang, Z.L.; Snyder, R.L. *Nanotechnology* 2007, 18, 365304.

[30] Unpublished results.

[31] Wang, X. D.; Summers, C. J.; Wang, Z. L. *Nano Lett.* 2004, *4*, 423.

[32] Huang, M. H.; Mao, S.; Feick, H.; Yan, H.; Wu, Y.; Kind, H.; Weber, E.; Russo, R.; Yang, P. *Science* 2001, *292*, 1897.

[33] Park, W. I.; Kim, D. H.; Jung, S. W.; Yi, G. C. *Appl. Phys. Lett.* 2002, *80*, 4232.

[34] Park, W. I.; Yi, G. C. *Adv. Mater.* 2004, *16*, 87.

[35] Collins, C.J.; Chowdhury, U.; Wong, M. M.; Yang, B.; Beck, A. L.; Dupuis, R. D.; Campbell, J. C. *Electron. Lett.* 2002, *38*, 824.

[36] Waldron, E.; Graff, J.; Schubert, E. *Phys. Stat. Sol. A* 2001, *188*, 889.

[37] Chowdhury, U.; Wong, M. M.; Collins, C. J.; Yang, B.; Denyszyn, J. C.; Campbell, J. C.; Dupuis, R. D. *J. Crys. Growth* 2003, *248*, 552.

[38] Zhu, T. G.; Chowdhury, U.; Wong, M. M.; Denyszyn, J. C.; Dupuis, R. D.; *J. Crys. Growth* 2003, *248*, 548.

[39] Wong, E. W,; Sheehan, P. E.; Lieber, C. M. *Science* 1997, *277*, 1971.

[40] Gao, R. P.; Wang, Z. L.; Bai, Z. G.; de Heer, W. A.; Dai, L.M.; Gao, M. *Phys. Rev. Letts*. 2000, *85,* 622.

[41] Poncharal, P.; Wang , Z. L.; Ugarte, D.; de Heer, W. A, *Science* 1999, *283,* 1513.

[42] Yu, M. F.; Lourie, O.; Dyer, M. J.; Moloni, K.; Kelly, T.F.; Ruoff, R. S. *Science* 2000, *287,* 637.

[43] Salvetat, J. P.; Kulik, A. J.; Bonard, J. M.; Andrew, G.; Briggs, D.; Stöckli, T.; Méténier, K.; Bonnamy, S.; Béguin, F.; Burnham, N. A.; Forró, L. *Advanced Materials* 1999, *11,* 161.

[44] Salvetat, J. P.; Andrew, G.; Briggs, D.; Bonard, J. M.; Bacsa, R. R.; Kulik, A. J.; Stöckli, T.; Burnham, N. A.; Forró, Lásló. *Phys. Rev. Letts.* 1999, *82,* 944.

[45] Treacy, M. M. J.; Ebbesen, T. W.; Gibson, J. M. *Nature* 1996, *381,* 678.

[46] Qi, H. J.; Teo, K. B. K.; Lau, K. K. S. *J. Mech. Phys. Solids* 2003, *51*, 2213.

[47] Wang, X. D.; Summers, C. J.; Wang, Z. L. *Nano Letters* 2004,*3,* 423.

[48] Wang, X.D.; Song , J. H.; Li , P.; Ryou, J. H.; Dupuis, R. D.; Summers, C. J.; Wang,, Z. L. *J. Am. Chem. Soc.* 2005, *127*, 7920.

[49] Landau, L.D.; Lifshitz, E. M. *Theory of Elasticity* 1959, Addison Wesley Publishing Company, Inc.

[50] Bai, X. D.; Gao, P. X.; Wang, Z. L.; Wang, E. G. *Appl. Phys. Letts* 2003*, 82*, 4806.

[51] a) S. K. Hong, H. J. Kim, H. G. Yang, *J. Appl. Phys.* 1996, *80*, 822.b) J. S. Tse, D. D. Klug, K. Uehara, Z. Q. Li, J. Haines, J. M. Le'ger, *Phys. Rev. B: Condens. Matter Mater. Phys.* 2000, *61*, 10 029.

[52] J. H. Song, X. D. Wang, E. Riedo, Z. L. Wang, *Nano Lett.* 2005, *5*,1954.

[53] C. Q. Chen, Y. Shi, Y. S. Zhang, J. Zhu, Y. J. Yan, *Phys. Rev. Lett.*2006, *96*, 075 505.

[54] C. Y. Nam, P. Jaroenapibal, D. Tham, D. E. Luzzil, S. Evoy, J. E. Fischer, *Nano Lett.*

2006, *6*, 153.

[55] a) M. Tabib-Azar, M. Nassirou, R. Wang, S. Sharma, T. L. Kamins, M. S. Islam, R. S. Williams, *Appl. Phys. Lett* 2005, *87*, 113 102. b) S. Hoffmann, I. Utke, B. Moser, J. Michler, S. H. Christiansen, V. Schmidt, S. Senz, P. Werner, U. Gösele, C. Ballit, *Nano Lett.* 2006, *6*, 662.

[56] Sidorenko S I, Makogon Y N, Beke D L, Csik A, Dub S N, Pavlova E P and Zelenin O V 2003 *Power Metall. Met. Ceram.* 42 14

[57] Cuenot S, Fretigny C, Demoustier-Champagne S and Nysten B 2004 *Phys. Rev.* B 69 165410

[58] Nilsson S G, Borrise X and Montelius L 2004 *Appl. Phys. Lett.* 85 3555

[59] Li X, Ono T, Wang Y and Esashi M 2003 *Appl. Phys. Lett.* 83 3081

[60] Wong E W, Sheehan P E and Lieber C M 1997 *Science* 277 1971

[61] Wu B, Heidelberg A and Boland J J 2005 *Nat. Mater.* 4 525

[62] Nam C Y, Jaroenapibal P, Tham D, Luzzil D E, Evoy S and Fischer J E 2006 *Nano Lett.* 6 153

[63] Tabib-Azar M, Nassirou M, Wang R, Sharma S, Kamins T L, Islam M S and Williams R S 2005 *Appl. Phys. Lett.* 87 113102

[64] Hoffmann S, Utke I, Moser B, Michler J, Christiansen S H,Schmidt V, Senz S, Werner P, G¨osele U and Ballit C 2006 *Nano Lett.* 6 662

[65] M.H. Huang, Y.Y. Wu, H. Feick, N. Tran, E. Weber and P.D. Yang, *Adv. Mater.* 13, 113 (2001).

[66] Z.W. Pan, Z.R. Dai and Z.L. Wang, *Science*, 291, 1947 (2001).

[67] X.Y. Kong, and Z.L. Wang, *Nano Letters*, 3, 1625 (2003).

[68] X.Y. Kong, Y. Ding, R. Yang, and Z.L. Wang, *Science* 303, 1348 (2004).

[69] W.L. Hughes and Z.L. Wang, *J. Am. Chem. Soc.*, 126. 6703 (2004).

[70] P.X. Gao, Y. Ding, W.J. Mai, W. L. Hughes, C.S. Lao and Z.L. Wang, *Science*, 309, 1700 (2005).

[71] X. F. Duan, Y. Huang, R. Agarwal, C.M. Lieber, *Nature,* 421, 241 (2003).

[72] G.F. Zheng, F. Patolsky, Y. Cui, W.U. Wang, C.M. Lieber, *Nature Biotechnology*, 23, 1294 (2005).

[73] X.D. Bai, P.X. Gao, Z.L. Wang and E.G. Wang, *Appl. Phys. Letts*., 82, 4806 (2003).

[74] X.D. Wang, C.J. Summers and Z.L. Wang, *Nano Letters*, 3, 423 (2004); X.D. Wang , J.H. Song , P. Li , J.H. Ryou , R.D. Dupuis , C.J. Summers and Z. L. Wang, *J. Am. Chem. Soc.*, 127, 7920 (2005).

[75] R.P. Gao, Z.L. Wang*, Z.G. Bai, W. de Heer, L. Dai and M. Gao, Phys. Rev. Letts., 85 (2000) 622-655

[76] X.D. Bai, P.X. Gao, Z.L. Wang and E.G. Wang, *Appl. Phys. Letts*., 82, 4806 (2003)

[77] J. H. He, C. S. Lao, L. J. Chen, D. Davidovic, and Z. L. Wang, *J. Am. Chem. Soc.*, 127, 16376 (2005)

[78] M.H. Zhao, Z.L. Wang, S. X.Mao, *Nano Letters*, 4, 587 (2004).

[79] The wurtzite structured ZnO can be described as a number of alternating planes composed of tetrahedrally coordinated O^{2-} and Zn^{2+} ions, stacked alternatively along the *c*-axis. The oppositely charged ions produce positively charged (0001)-Zn and

negatively charged $(000\bar{1})$-O polar surfaces. The Zn-terminated surface is at the growth front (positive c-axis direction) due to its higher catalytic activity (Z.L. Wang, X.Y. Kong and J.M. Zuo, *Phys. Rev. Letts*., 91, 185502 (2003)).

[80] A simple calculation indicates that the magnitude of V_s^+ and V_s^- are in the order of a few tens to hundreds of volts. An accurate calculation of the potential distribution as a result of the ionic charges introduced by piezoelectric effect and the surface charges caused by boundaries has to be solved numerically. In our current analysis, a correct magnitude and sign of the potential is sufficient for illustrating the physical model.

[81] S. Hasegawa, S. Nishida, T. Yamashita and H. Asahi, *J. Ceramic Processing Res*., 6, 245 (2005).

[82] R.F. Pierret, Semiconductor Device Fundamentals, Addison-Wesley Publishing Com., Chapter 14, pp. 477 (1996); W.I. Park, G.C. Yi, J.W. Kim and S.M. Park, *Appl. Phys. Letts*. 82, 4358 (2003).

[83] C. Keawboonchua and T. G. Engel*, IEEE Transactions On Plasma Science*, 31, 123 (2003).

[84] W.L. Hughes and Z. L. Wang, *Appl. Phys. Letts*., 86, 043106 (2005).

[85] Y. Huang, X.F. Duan, Y. Cui, L.J. Lauhon, K.H. Kim, C.M. Lieber, *Science*, 294, 1313 (2001).

[86] A. Bachtold, P. Hadley, T. Nakanishi, C. Dekker, *Science*, 294, 1317 (2001).

[87] J. Chen, V. Perebeinos, M. Freitag, J. Tsang, Q. Fu, J. Liu, P. Avouris, *Science*, 310, 1171 (2005).

[88] M. Billinghurst & T. Starner, *IEEE Computer* 1999, *32*, 57.

[89] D. De Rossi, A. Della Santa and A. Mazzoldi, *Mat. Sci. Eng. C* 1999, *7*, 31.

[90] R.F. Service, *Science* 2003, 301, 909.

[91] Q. M. Zhang, V. Bharti and X. Zhao, *Science* 1998, *280*, 2101.

[92] A.J. Heeger, *J. Phys. Chem. B* 2001, *105*, 8475.

[93] S. Ashley, *Sci. Amer.* 2003, *10*, 52.

[94] Q. M. Zhang, H. Li, M. Poh, F. Xia, Z.Y. Cheng, H. Xu and C. Huang, *Nature* 2002, *419*, 284.

[95] X. Yu, J. B. Bates, G. E. Jellison Jr. and F. X. Hart, *J. Electrochem.Soc.* 1997, *144*, 524.

[96] N. S. Shenck and J. A. Paradiso, *IEEE Micro* 2001, *21*, 30-42.

[97] R. Venkatasubramanian, E. Siivola, T. Colpitts and B. O'Quinn, *Nature* 2001, *413*, 597.

[98] D. Setiadi, H. Weller and T. D. Binnie, *Sensor Actuat. A—Phys.* 1999, *76*, 145.

[99] J.H. Song, J. Zhou and Z.L. Wang, *Nano Letters* 2006, *6*, 1656.

[100] J. Zhou, C.S. Lao, P.X. Gao, W.J. Mai, Z.L. Wang and N. S. Xu, *Solid State Comm.,* 2006, *139*, 222.

[101] S.R. Platt, S. Farritor and H. Haider, *IEEE/ASME Tran. Mechatronics,* 2005, *10*, 240.

[102] Hasegawa, S.; Nishida, S.; Yamashita, T.; Asahi, H. *J. Ceramic Processing Res.* 2005, 6, 245.

[103] Park, W. I.; Yi, G. C.; Kim, J. W.; Park, S. M. *Applied Physics Letters* 2003, 82, (24), 4358-4360.

[104] Yannouleas, C.; Landman, U. *Physical Review B* 2000, 61, (23), 15895-15904.

[105] X.D. Wang, J. Zhou, J.H. Song J. Liu, N.S. Xu and Z.L. Wang, *Nano Letters*, 6, 2768 (2006).

[106] 17. Ma, C., *et al.*, *J. Am. Chem. Soc.*, (2004) 126, 708

[107] Fischler, C., *et al.*, *Appl. Phys. Lett.* (1970) 17, 252

[108] He, Jr, H., *et al.*, *Adv. Mater.* (2007), in press

[109] Z.L. Wang and J.H. Song, Science, 312, 242 (2006).

[110] Z.L. Wang, X.D. Wang and J.H. Song, US patent pending (2006).

[111] J. Frühauf and S. Krönert, *Microsyst. Technol.* 11, 1287 (2005).

[112] Z.L. Wang, *Adv. Materials*, submitted (2006).

[113] J. H. He, C.H. Hsin, L.J. Chen, Z.L. Wang, *Adv. Mater*., in press (2006).

[114] Wang, X. D.; Song, J. H.; Liu, J.; Wang, Z. L. *Science* 2007, *316*,102.

[115] Wang, X.D.; Liu, J.; Song, J.H.; Wang, Z.L. *Nano Lett*. 2007 *7* 2475

[116] Li, Y.; Wong, C. P. *Appl. Phys. Lett.* 2006, *89*, 112112.

[117] Lao, C.S.; Li, Y.; Wong, C.P.; Wang, Z.L. *Nano Lett.* 2007, *7* 1323.

[118] Lao, C.S., Park, P.C., Kuang, Q., Deng, Y.L., Sood, A.K., Polla, D.L. and Wang, Z.L., *J. Am. Chem. Soc.* 2007, to appear online.

[119] Jiu, T.; Li, Y.; Gan，H.; Li, Y.; Liu, H.; Wang, S.; Zhou, W.; Wang, C.; Li, X.; Liu，X.; Zhu, D. *Tetrahedron* 2007, 63, 232.

[120] Nagata, T.; Osuka, A.; Maruyama, K. *J. Am. Chem. Soc.* 1990, 112, 3054;Gaylord, B. S.; Wang, S.; Heeger, A. J.; Bazan, G. C. *J. Am. Chem. Soc.* 2001, 123, 6417;

[121] George, S. J.; Ajayaghosh, A.; Jonkheijm, P.; Schenning, A. P. H. J.; Meijer, E. W. *Angew. Chem., Int. Ed.* 2004, 43, 3422;

[122] Jonkheijm, P.; Hoeben, F. J. M.; Kleppinger, R.; van Herrikhuyzen, J.; Schenning, A. P. H. J.; Meijer, E. W. *J. Am. Chem. Soc.* 2003, 125, 15941; Wolffs, M.; Hoeben, F. J. M.; Beckers, E. H. A.; Schenning, A. P. H. J.; Meijer, E. W. *J. Am. Chem. Soc.* 2005, 127, 13484.

[123] Gao, Y.F. and Wang, Z.L. *Nano Letters*, 2007, *7*, 2499.

[124] Hasegawa, S.; Nishida, S.; Yamashita, T.; Asahi, H. *J. Ceramic Processing Res.* 2005, 6, 245.

[125] Perez-Garcıa, B., Zun˜iga-Perez, J., Munoz-Sanjose, V., Colchero, J., and Palacios-Lidon, E., *Nano Letters*, 2007, *7*, 1505.